Numerical simulations of the dyslocation dynamics in the very high-cycle fatigue regime

Eddie Margarita Listrange Lopez Guerrero Longsworth

Université Grenoble Alpes

THÈSE

Pour obtenir le grade de

DOCTEUR DE L'UNIVERSITÉ DE GRENOBLE

Spécialité : **2MGE : Matériaux, Mécanique, Génie civil, Electrochimie**

Arrêté ministérial : 25 mai 2016

Présentée par

Margarita LONGSWORTH

Thèse dirigée par **Marc FIVEL**
et codirigée par **Nicolas RANC**

préparée au sein du **Laboratoire Science et Ingénierie des Matériaux et Procédés**
dans **l'École Doctorale I-MEP2 - Ingénierie - Matériaux, Mécanique, Environnement, Energétique, Procédés, Production**

Towards dislocation dynamics simulations of very-high-cycle fatigue: a novel approach based on the physical modelling of cross-slip

Thèse soutenue publiquement le **29 octobre 2021**,
devant le jury composé de :

Edgar RAUCH
Directeur de Recherche CNRS, SIMaP, Président
Ghiath MONNET
Chercheur-ingénieur HDR, EDF, Rapporteur
Alexander HARTMAIER
Professeur, Rühr-Universität Bochum, ICAMS, Rapporteur
Dan MORDEHAI
Professeur, Technion University, Examinateur
Laurent DUPUY
Chercheur-ingenieur, CEA Saclay, Examinateur
Marc FIVEL
Directeur de Recherche CNRS, SIMaP, Directeur de thèse
Nicolas RANC
Professeur Arts et Métiers ParisTech, PIMM, Co-Directeur de thèse

This page intentionally contains only
a statement about its contents.

Declaration of Authorship

I hereby declare that this thesis is my own work and effort and that it has not been submitted anywhere for any award. Where other sources of information have been used, they have been acknowledged.

Place and date	Full name and signature

Abstract

In order to investigate the Very High Cycle fatigue behavior of FCC metals using Discrete Dislocation Dynamics simulations, the present thesis proposes an improved model of cross-slip mechanism which has been implemented in the nodal DDD code NuMoDis (Drouet et al., 2014). The first step was to obtain the effect of stress on the activation enthalpy of cross-slip using discrete dislocation dynamics. The obtained results were compared with two modern cross-slip models, namely the numerical model of Kang et al. (2014) and the analytical model of Malka-Markovitz and Mordehai (2019). It was shown that both cross-slip models were in quantitative agreement with the results obtained using discrete dislocation dynamics simulations. Due to its easy calibration based on the unstressed energy barrier of cross-slip, the analytical model of Malka-Markovitz and Mordehai (2019) was preferred to be employed in the discrete dislocation dynamics code to effectively calculate the activation enthalpy of screw segments.

The second step was to implement the recent cross-slip rate model proposed by Esteban-Manzanares et al. (2020) into the discrete dislocation dynamics code NuMoDis (Drouet et al., 2014). The obtained results were compared with the numerical values of the cross-slip rate estimated by Vegge et al. (2000) and Oren et al. (2017) using atomistic simulations. It was demonstrated that the proposed cross-slip modelling was able to reproduce atomistic results using only one free parameter, namely the unstressed energy barrier of cross-slip required to fit the analytical model developed by Malka-Markovitz and Mordehai (2019).

As a first application of the benchmarked simulation methodology, the firsts cycles of the gigacycle fatigue regime were simulated two different configurations, namely one isolated screw dislocation and a network of twelve mixed dislocations. It was found that the effect of cross-slip on an isolated dislocation was negligible, whereas it produced irreversible changes in the case of a dislocation network. With the aim of simulating a much larger number of cycles, a jump-in-cycles method was finally proposed in the last chapter.

Résumé

Afin de simuler le comportement en fatigue à très grand nombre de cycle de métaux par dynamique des dislocations, cette thèse propose une modélisation améliorée de la loi de glissement dévié utilisée jusqu'alors. La première étape a consisté à obtenir l'effet de la contrainte sur l'enthalpie d'activation du glissement dévié en utilisant la dynamique des dislocations discrètes. Les résultats obtenus ont été comparés à deux modèles récents de glissement dévié, à savoir le modèle numérique de Kang et al. (2014) et le modèle analytique de Malka-Markovitz and Mordehai (2019). Il a été démontré que ces deux modèles étaient en accord quantitatif avec les résultats obtenus à l'aide de simulations de la dynamique des dislocations discrètes. L'enthalpie d'activation des segments vis est estimée à partir du modèle analytique de Malka-Markovitz and Mordehai (2019) dont la calibration est aisée à partir de la valeur de la barrière d'énergie sans contrainte.

La deuxième étape a consisté à mettre en œuvre le récent modèle de probabilité de glissement dévié proposé par Esteban-Manzanares et al. (2020) dans le code de dynamique des dislocations discrètes. Les résultats obtenus ont été comparés aux valeurs numériques du taux de glissement dévié estimées par Vegge et al. (2000) et Oren et al. (2017) en utilisant des simulations atomistiques. Il a été démontré que le modèle de glissement dévié proposé était capable de reproduire les résultats atomistiques en utilisant un seul paramètre libre, à savoir la barrière d'énergie sans contrainte du glissement dévié requise par le modèle analytique développé par Malka-Markovitz and Mordehai (2019).

Comme première application du code de DDD ainsi amélioré, les premiers cycles du régime de fatigue gigacyclique ont été simulés dans deux configurations différentes, à savoir une dislocation vis isolée et un réseau de douze dislocations mixtes. Il a été constaté que l'effet du glissement dévié sur une dislocation isolée était négligeable, alors qu'il produisait des changements irréversibles dans le cas d'un réseau de dislocations. Dans le but de simuler un nombre beaucoup plus important de cycles, une méthode de saut dans les cycles a finalement été proposée dans le dernier chapitre.

Für
Elina Longsworth
und
Bernhard Klemt

Acknowledgements

Hereby I thank my advisors, Marc FIVEL and Nicolas RANC, for making this project possible. Their thoughtful suggestions and wise commentaries were greatly appreciated throughout these years. I also want to express my deepest gratitude to the other jury members, namely Ghiath MONNET, Alexander HARTMAIER, Edgar RAUCH, Dan MORDEHAI and Laurent DUPUY, for carefully reading this manuscript and contributing to it with their expertise.

I would like to express my sincere appreciation to the other members of the FastMat team, namely Vincent JACQUEMAIN, Christophe CHEULEU, Doriana VINCI, Véronique FAVIER, Olivier CASTELNAU, Vincent MICHEL and Cristian MOCUTA, for warmly receiving us when we met with them at their laboratory in Paris.

To my office colleagues Aatreya VENKATESH, Oğuz OZDEMIR, Fanshi MENG, Nicolas BOTTER, Guillaume HAMELIN and Arthur DEPRES, for the common activities that we mutually enjoyed before the pandemic.

I thank to my mother Elina LONGSWORTH for her loving encouragement and unconditional support in all my personal endeavors. I am also very grateful to my partner Bernhard KLEMT for his tireless work to built our future together.

Finally, I acknowledge having received financial support from the European Research Council (ERC) under the European Union's Horizon 2020 research and innovation programme (ERC-2016-COG grant agreement number 725142).

Contents

List of Figures

List of Tables

List of Publications

A partial content of the present thesis has already been published in the following papers:

M. Longsworth and M. Fivel. The effect of stress on the cross-slip energy in face-centered cubic metals: A study using dislocation dynamics simulations and line tension models *Journal of the Mechanics and Physics of Solids* **148** p. 104281 (2021).

M. Longsworth and M. Fivel. Investigating the cross-slip rate in face-centered cubic metals using an atomistic-based cross-slip model in dislocation dynamics simulations *Journal of the Mechanics and Physics of Solids* **153** p. 104449 (2021).

List of Abbreviations

BEM	Boundary Element Method
CDM	Continuum Damage Mechanics
DDD	Discrete Dislocation Dynamics
FCC	Face-Centered-Cubic
FE	Friedel-Escaig
FEM	Finite Element Method
FL	Fleischer
FPD	Fractional Partial Dislocations
HA	Harmonic Approximation
HCF	High Cycle Fatigue
HTST	Harmonic Transition State Theory
kMC	kinetic Monte Carlo
LCF	Low Cycle Fatigue
LT	Line Tension
MC	Monte Carlo
MD	Molecular Dynamics
MMC	Metropolis Monte Carlo
MN	Meyer-Neldel
PSB	Persistent Slip Band
SF	Stacking-Fault
TST	Transition State Theory
VHCF	Very High Cycle Fatigue
XFEM	Extended Finite Element Method
XTFEM	Extended Space-Time Finite Element Method

Chapter 1

Introduction

Mechanical structures can break under repeated loading well below the yield stress associated to the underlying material. In the engineering jargon, fatigue of materials refers to the progressive destruction of the cohesive atomic bonds as a result of cyclic loading. Many machine components and structures are subjected to cyclic loading at small stress amplitudes, such as gas turbines, car engines, drilling machines and high-speed trains (Kazymyrovych, 2009). The formation and propagation of cracks due to a repetitive or cyclic load is known as fatigue failure (Freudenthal, 1946). It has been estimated that 90% of all mechanical systems associated to the energy production and transportation industry fail as a result of fatigue mechanisms (de Freitas, 2017). Many relevant mechanical structures are subjected to gigacyclic fatigue in our modern technological society. In automobiles, the valve in a thermal engine can endure up to 10^9 cycles during its lifespan. In airplanes, the wings and fuselage can endure up to 10^7 loading cycles associated to the take-off and landing (Costa et al., 2020). Fatigue design has developed scientific methods and experimental approaches to asses the fatigue life of such structures, which require a precise characterization of the underlying material to minimize the risk of failure. An efficient characterization of materials undergoing gigacycle fatigue is still a challenging problem because more than 10^7 cycles are typically required for this process.

This chapter provides a brief overview on the experimental characterization and physical modelling of the gigacyclic regime as a way to introduce the main objective of the present manuscript, namely the development of a more physical simulation technique that is able to simulate the gigacyclic regime at the microstructure scale. Section 1.1 gives an overview of the experimental characterization of the gigacyclic regime using modern ultrasonic machines, section 1.2 presents the few attempts to simulate the gigacyclic regime and section 1.3 shows the thesis structure.

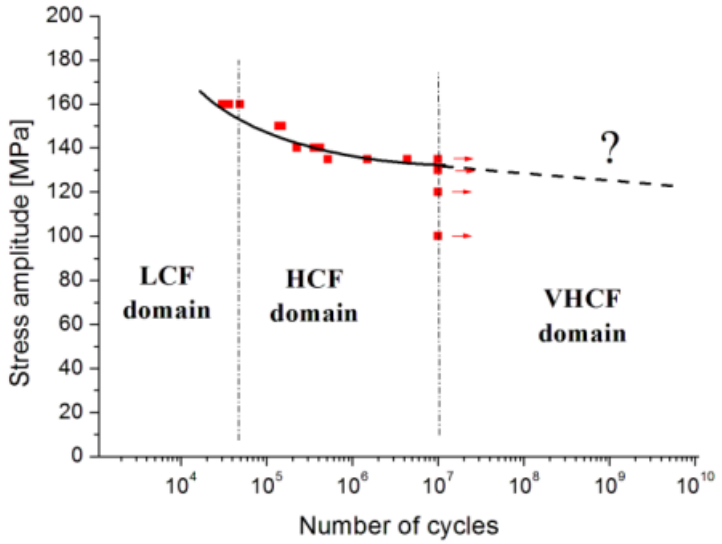

Figure 1.1: SN curve showing the fatigue domains. *Source:* Ranc (2017).

1.1 Characterization of the ultrasonic fatigue

1.1.1 Classical fatigue design

The present fatigue standards are based on the concept of fatigue limit introduced by Wöhler (1860). A fatigue test can be performed by subjecting a sample to cyclic stresses using a fatigue machine over many cycles until the sample fails. The aim is to obtain a SN curve of the material. A SN curve is a plot of the stress amplitude versus the number of cycles required to break an specimen. The fatigue domain is characterized by the number of cycles to failure. Figure 1.1 shows the typical three broad fatigue regimes evidenced on the SN curve: (1) the Low-Cycle-Fatigue (LCF) regime - up to 10^4 cycles to failure, (2) the High-Cycle-Fatigue (HCF) regime - between 10^4 and 10^7 cycles to failure and (3) the Very-High-Cycle-Fatigue (VHCF) regime - over 10^7 cycles to failure. The stress value associated to the horizontal asymptote obtained by extrapolation from the LCF and HCF domain is known as the fatigue limit. In the present standards it is assumed that the specimen will never break if the applied stress amplitude is smaller than the fatigue limit. In other words, the sample is expected to exhibit an infinite lifespan for lower stress amplitudes than the fatigue limit.

Obtaining a single SN curve can be extremely time-consuming. Traditionally, hydraulic machines operating at 30 Hz have been used to perform fatigue tests. Therefore, the test must be carried on for at least a month in order to compute part of the HCF domain. Moreover, fatigue failure is a stochastic process. In consequence, a minimum of 25 fatigue tests are required in order to obtain a reliable

SN curve. Due to the impractical test duration, the infinite lifespan under the fatigue limit was generally accepted until recent years.

The fatigue characterization in the VHCF domain represents an even greater challenge. In the past two decades, powerful ultrasonic machines operating at 20 kHz have been used to improve the test duration (Bathias, 1999; Stanzl-Tschegg and Mayer, 2001; Stanzl-Tschegg, 2014). The ultrasonic machines represented an immense progress on the generation of reliable SN curves up to the VHCF domain. Moreover, the testing time up to 10^9 cycles was considerably reduced to a few days, which constituted an important breakthrough on practical fatigue testing. Most crucially, experiments confirmed that most materials can break at stress levels considered to be safe after more than 10^7 cycles (Bathias, 1999; Pyttel et al., 2011; Shiozawa et al., 2001), in contradiction to the assumption of an infinite lifetime for applied stresses below the fatigue limit. It can be concluded that it is possible to have fracture for number of cycles higher than 10^7 and for stress amplitude lower than the fatigue limit defined by modern standards. The technological relevance of the VHCF regime has motivated a deeper research using ultrasonic machines. Some of the most important challenges currently are:

i to understand the effect of loading frequency on the fatigue mechanism. The reason why some SN curves obtained using hydraulic and ultrasonic machines can be different is still controversial (Furuya et al., 2002; Tsutsumi et al., 2009; Willertz, 1980).

ii to estimate the applied stress more accurately. A the present time, the calculation is based on the elastic approximation, which is only valid when the plastic strain is small.

iii to account for the effect of self-heating on the obtained SN curves. Air guns have helped to counterbalance the specimen's self-heating. In spite of it, the samples' temperature can increase up to several hundreds of degrees due to the high-frequency vibrations. Since temperature significantly affects the physics of materials, the fatigue characterization at room temperature is still a challenge.

iv to improve the test duration beyond 10^9 cycles. As an example, a fatigue test of 10^{11} cycles using an ultrasonic machine takes approximately 2 months. Although the testing has been drastically reduced, the test duration beyond 10^{10} cycles remains impractical.

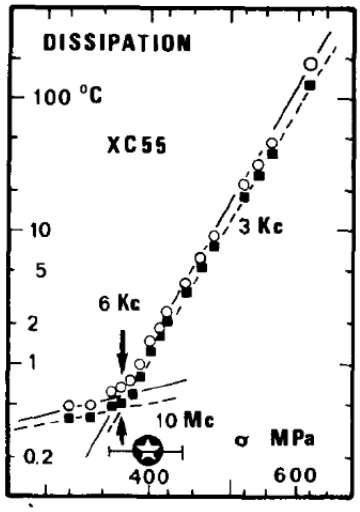

Figure 1.2: Self-heating curve of XC55 steel. *Source:* Luong (1995).

1.1.2 Self-heating methods

When a sample is subject to cyclic fatigue, its temperature increases. The mechanical energy is dissipated as heat, which provokes an increase of temperature. This effect is known as self-heating. Experimental techniques have been developed to determine the fatigue limit using the so-called self-heating methods (Luong, 1995, 1998; La Rosa and Risitano, 2000; Krapez et al., 2000; Munier et al., 2014). In these techniques, the stress amplitude is increased after applying a sequence of approximately 10^4 cycles to allow the temperature to stabilize. Infrared cameras or thermocouples are used to measure the specimen's self-heating during cyclic fatigue. The obtained plots of stabilized temperature vs applied stress are known as self-heating curves. Two characteristic regimes can be observed in the typical self-heating curve (see figure 1.2). In both regimes, the temperature increases linearly with the applied stress. In the low-stress regime, the temperature increases slowly, whereas in the high-stress regime, the temperature increases drastically faster. The conventional fatigue limit is thus conventionally defined as the stress amplitude separating these two regimes.

The self-heating method can be used to estimate the fatigue limit of materials within a few hours. Hydraulic machines working at 30 Hz are typically employed. The self-heating method has been used to determine the fatigue limit of several steels (Munier et al., 2014). However, it was shown that for 316L steel under tension-tension cyclic loading, the self-heating method can lead to an underestimation of the fatigue limit (Krapez et al., 2000). For materials in which the temperature increase is weak, such as in aluminum and some of its alloys, the two regimes of the self-heating curve are hardly distinguishable (Krapez et al., 2000). In this case, the fatigue limit

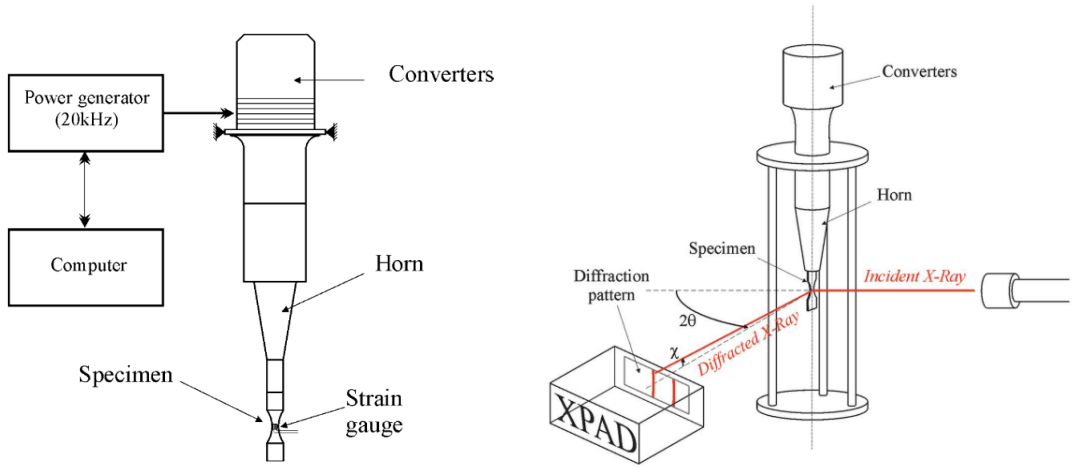

Figure 1.3: Schematic diagram of an ultrasonic fatigue machine.
Source: Ors et al. (2019).

cannot be easily determined using the self-heating method. Moreover, it has been reported that the temperature of aluminum alloys does not easily stabilize at certain stress amplitudes (Wagner et al., 2010). For that reason, the self-heating curve can be difficult to obtain.

In general, the heat source can be categorized into two components, namely, the thermo-elastic source associated to the thermal expansion of the material, and the dissipative source related to the irreversible deformation of the microstructure (Boulanger et al., 2004). In fact the average value of the thermo-elastic source is zero because it reversibly oscillates during one cycle, whereas the dissipated energy rate is always positive due to its monotonic increment with time. At the microstructural level, part of the work applied to the crystal is dissipated through the motion of dislocations, which might lead to an increased dislocation density, reactions between dislocations and the formation of complex dislocation structures. The stored energy is associated to the plastic deformation generated by the microstructural defects. Since the stored energy indicates the amount of permanent damage accumulated, it can be used to characterize the fatigue level during cyclic loading. Once the temperature of the sample has been stabilized, the applied work is equal to the dissipated and stored energy. The self-heating method has been thus implemented to estimate the stored energy of steels in the LCF and HCF regimes (Chrysochoos et al., 2008; Connesson et al., 2011).

In the VHCF regime, the applied stresses are very weak with respect to the yield stress. Sophisticated measurements have shown that the temperature variations are very small when the cyclic fatigue is generated by hydraulic machines operating at 30 Hz. In order to increase the heat rate emitted at low applied stresses, the

self-heating method has been recently implemented in the case of ultrasonic machines (Blanche et al., 2015). The heat equation must be inverted to obtain the heat sources. However, the noisy character of the temperature field can make the inversion unstable. A reduced-basis projection of thermal data has been proposed to improve the signal-to-noise ratio before estimating the heat sources (Ranc et al., 2015). In the VHCF regime, the time integration of the infrared camera does not detect the thermo-elastic source. In this particular case, the heat source is equal to the average dissipation after many cycles. However, the applied work must be also estimated in order to calculate the stored energy. Modern experiments at the synchrotron SOLEIL are currently being performed to estimate the applied work during ultrasonic fatigue. These experiments are challenging because the time-resolved evolution of both stress and strain must be obtained in order to estimate the applied work. A new method based on time-resolved X-ray diffraction was implemented to measure the elastic strain and applied stress during ultrasonic fatigue (Ors et al., 2019).

The left-handed side of figure 1.3 shows an ultrasonic device consists of three main components, namely (a) the power generator, which converts the voltage into a sinusoidal signal, (b) the piezo-electric converter, which loads the specimen into its first longitudinal mode and (c) a horn that amplifies the mechanical vibration generated by the converted to obtain the desired stress amplitude. The total strain on the specimen is directly measured using two gauges glued at its center. A probing monochromatic X-ray beam of 16 keV hits the sample during cyclic loading to obtain information about the microstructure, such as the stress heterogeneity and the dislocation density evolution (see right-handed side of figure 1.3). Since the fatigue machine is operated at 20 kHz, the period of an applied cycle is 50 microseconds. In order to reproduce the time-resolved intensity of the diffracted beam, the aperture time of the detector must be sufficiently fast. For that reason, an XPAD detector with an aperture time of one microsecond is necessary for the investigation of ultrasonic fatigue. After a certain adjustable delay, an XPAD detector acquires the corresponding diffractogram for one microsecond. By monitoring the diffracted X-ray beam as a function of the time delay, the time-resolved diffracted intensity during one full cycle can be reproduced with the information obtained from the 50 diffractograms.

Once the accumulated intensity of the XPAD image is sufficiently strong, the image is stored.

A detailed diagram of the triggering chain of the XPAD detector is shown in figure 1.4 (a). The gauge conditioner reads the signal sent by the strain gauge. At a prescribed voltage value, the first data card signalizes a waiting time to the delay line. Once said delay has passed, the delay line triggers simultaneously the

gauge acquisition using the second data card and the detector aperture during one microsecond. The signal send by the delay line passes through a function generator before arriving to the XPAD detector. This step ensures that the signal sent by the delay line has the appropriate shape. In the particular experiments done at the synchrotron SOLEIL, the zero delay signal is set when the gauge reaches a value of 0.5 V (labeled as TRIG in Fig 1.4 (b)). The triggering process is repeated each 50 microseconds. In this way, a diffractogram corresponding to the exact same part of the cycle is periodically read. The same process must be repeated until the accumulated intensity on the XPAD image is sufficiently strong to achieve good counting statistics on every pixel conforming the picture. Once the XPAD image acquires the desired quality, it is finally registered on the system. The time delay is then increased by one microsecond and the process is repeated until the full cycle has been probed. As a result, 50 diffractograms are obtained as function of the time delay. Finally, the peak position and width are reported as function of the time delay (see Fig 1.4 (b)). The mean elastic strain obtained from the shift of diffraction peaks allows to estimate the applied stress using the scale transition model. On the other hand, the fluctuation of elastic strain obtained from the peak broadening provides information about the intragranular strain heterogeneities and the dislocation density (Bretheau and Castelnau, 2006).

Ors et al. (2019) found that in order to obtain a strain resolution of 6×10^{-6}, the detector must be triggered 20,000 times for each XPAD image. Since the applied frequency is 20000 Hz, each XPAD image can be obtained after one second. Considering also the reading time, each diffractogram is obtained after 4.5 seconds. For that reason, 4.5×10^6 cycles are executed after completing the 50 images required to describe the full cycle, which are a small amount of cycles with respect to the total number of cycles to failure. Therefore, the fatigue properties are assumed to remain constant during the acquisition process.

1.2 Physics of the ultrasonic fatigue

1.2.1 Damage mechanisms and fatigue-life diagrams

The effect of LCF and HCF on the physical microstructure has been thoroughly investigated (Lukáš and Klesnil, 1973; Suresh, 1998; Polak, 1991). In contrast, the theoretical research on VHCF has been limited to the available experimental results. At the microstructural level, fatigue can be described as the initiation and subsequent propagation of cracks, which ultimately lead to the specimen failure. This physical process strongly depends on the stress amplitude and the number of cycles. In the LCF regime, the cracks appear very quickly but they propagate

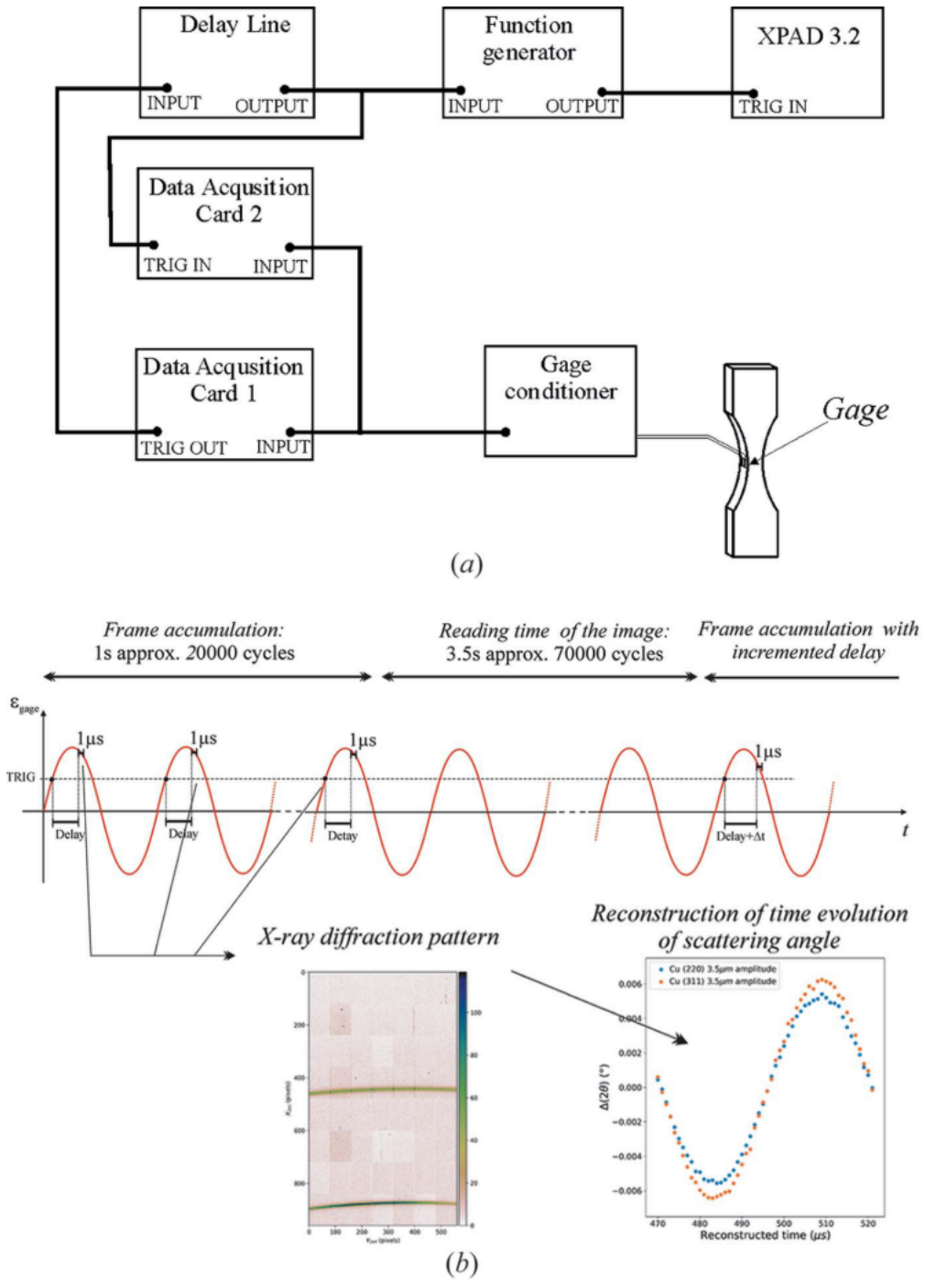

Figure 1.4: Schematic diagram of an ultrasonic fatigue machine.
Source: Ors et al. (2019).

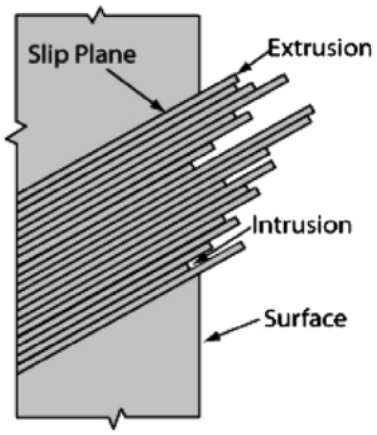

Figure 1.5: Intrusions and extrusions conforming the PSBs.
Source: Karuskevich et al. (2012).

at much slower rate to the surface, typically near the grain boundary. In strong contrast, the stage of crack initiation on the HCF and VHCF regimes is much longer than the crack propagation, which indicates that the underlying mechanisms occurring on the LCF regime might be fundamentally different.

The firsts VHCF theories were developed by Mughrabi (2002). He specified the conditions under which fatigue failure could occur. Moreover, he identified different physical mechanisms leading to fatigue for two broad types of solids, namely for pure single-phase metallic materials (type I) and for imperfect crystalline solids reinforced by non-metallic inclusions (type II). According to Mughrabi (2002), materials of type I can only exhibit surface cracking. In contrast, depending on the applied stress amplitude, materials of type II can undergo either surface or internal fatigue failure. Surface cracks occur more often at intermediate and high stress amplitudes, whereas cracks growing from the internal structure are more common at small stress amplitudes (Mughrabi, 2002). The fatigue damage is caused by irreversible slip during cyclic loading. Cyclic slip is said to be irreversible if the atomic positions at the beginning of the cycle are not completely restored when the stress cycle ends. In other words, the slip displacements during the first half of the cycle are not completely reversed on the second half of the cycle (Mughrabi, 2001). As a consequence, the small changes accumulate on the material after every cycle forming microstructural inhomogeneities. The strain concentration at the plastically deformed zone constitutes a strain localization (Croft et al., 2008). In general, microstructural inhomogeneities leading to strain localization can be present on the material before loading, such as internal inclusions, twin boundaries, or even external defects (Vogt et al., 2020).

For perfect single-phase metallic materials (type I), the dominant form of strain

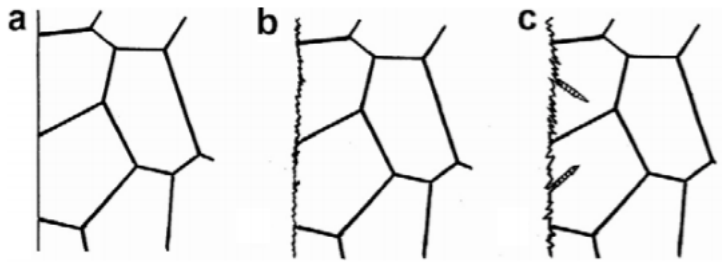

Figure 1.6: Crack initiation process at lower stress amplitudes than the PSB threshold: (a) initial state, (b) surface roughening and (c) stage I crack initiation.
Source: Mughrabi (2006).

localization is the Persistent Slip Band (PSB) (Mughrabi, 2001). The PSBs are zones of high cyclic slip activity. The zones of high dislocation density are linked together below the material surface, whereas the zones of low dislocation density serve as channels of relatively free glide Lukáš and Kunz (2004). The steps formed at the material surface when dislocations reach the boundary are known as extrusions (Lukáš et al., 1966). For that reason, the width, length and depth of the slip bands increases with the number of cycles. The word "persistent" refers to the fact that such slip bands remain after etching or polishing the surface (Lukáš et al., 1966). Reverse extrusions penetrating the bulk were termed intrusions (see Figure 1.5). In the case of ductile metals, there is no distinction between an intrusion and a crack. According to Basinski and Basinski (1989), cracks are intrusions which have grown deeper than the limiting extrusion height. Failure occurs when a crack reaches some critical depth at which the crack propagates throughout the bulk, breaking the complete material (Basinski and Basinski, 1989).

For many pure metals and alloys, PSBs are reported to be formed at well-defined stress threshold amplitudes (Mughrabi et al., 1983; Mughrabi, 1984). By definition, the PSB threshold corresponds to the minimum stress at which PSBs can be formed (Mughrabi, 2002). The PBS threshold can also be associated to the (stage I) crack initiation and the initial crack growth (Mughrabi et al., 1983; Mughrabi, 1984). At stress levels above the PSB threshold, fatigue cracks emerge at the PSB surface. The rapid formation of extrusions can lead to fatigue crack initiation (Essmann et al., 1981). According to Mughrabi (2002), cracks can initiate when the surface roughness reaches a critical value. In an earlier work, Mughrabi et al. (1983) characterized the surface roughness as the local root-mean-square deviation between neighboring glide planes:

$$R \approx \sqrt{4pN\gamma_{pl}bh} \tag{1.1}$$

where N is the number of cycles, γ_{pl} the local plastic strain at the surface, b the Burgers vector magnitude, h the plane separation and p the slip irreversibility, defined as the irreversible plastic strain divided by the plastic strain accumulated during one cycle. Both the slip irreversibility and the local plastic strain are decreasing functions of the applied stress. If the slip irreversibility and the local plastic strain are negligibly small, but finite, the surface roughness can reach the critical value after a sufficiently large number of cycles (see equation 1.1). When the material surface reaches a state of critical roughness, the local stress produced by the extrusions and intrusions can surpass the PSB threshold value at the surface. This can lead to the formation of inhomogeneities at the surface, which are capable of initiating stage-I cracks. After a sufficiently large number of cycles, the surface cracks might be able to grow and propagate into the material, which can cause failure at stress amplitudes below the PSB threshold (Mughrabi, 2002) (see figure 1.6). In principle, there exists a sufficiently small stress known as the irreversibility threshold, below which the surface roughness remains negligible for a specific maximum number of cycles (Mughrabi, 2002).

Figure 1.7 shows an schematic fatigue life diagram for type I materials in the form of a Coffin-Manson plot (plastic strain amplitude vs number of cycles to failure). Alternatively, a fatigue life diagram can also be presented in the SN form (applied stress amplitude vs number of cycles to failure) as previously shown in figure 1.1. The range I (LCF) corresponds to the strain amplitudes above the PSB threshold. In this range, cracks initiation is fast with respect to crack propagation. The range II (HCF) corresponds to the PSB threshold. In this range, crack initiation is slow with respect to crack propagation. The range III (VHCF) corresponds to the strain amplitudes between the PSB and irreversibility thresholds. In this range, most of the fatigue life is invested in crack initiation. Therefore, fatigue lives are much longer but finite. The range IV (true VHCF) corresponds to the strain amplitudes below the irreversibility threshold. In principle, cracks are simply not formed and infinite fatigue life could be possible. The extent of range II was explained by Mughrabi (2002) using the concept of critical roughness. The local plastic strain just below the PSB threshold γ_{pl} is significantly lower than the local plastic strain just above the PSB threshold γ_{PSB} ($\gamma_{PSB} \approx 10^2\gamma_{pl}$ for copper (Mughrabi et al., 1983; Mughrabi, 1984)). Similarly, the slip irreversibility just below the PSB threshold is small with respect to the slip irreversibility just above the PSB threshold. Therefore, the number of cycles required to reach the critical roughness at the onset of range II is much smaller than the number of cycles required to reach the critical roughness at the onset of range III. In the particular case of copper, the number of cycles to failure at the beginning of range II is approximately two orders of magnitude smaller than the number of cycles to failure at the beginning of range III (see figure 1.7).

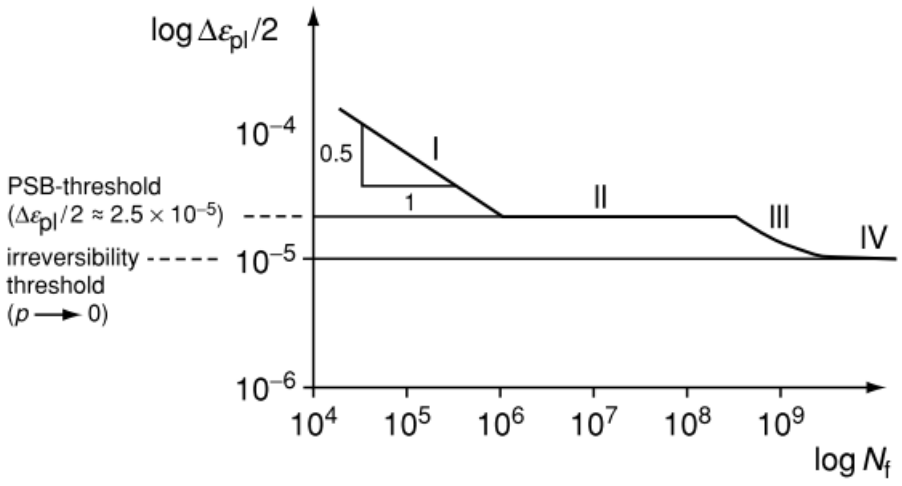

Figure 1.7: Multi-stage life diagram for Type I materials. The numerical values correspond to pure copper.
Source: Mughrabi (2002).

As a conclusion, type I materials can only exhibit surface failure. In contrast, type II materials can undergo both internal and surface failure. By definition, type II materials can contain internal defects, such as non-metallic inclusions, pores or contraction cavities (Mughrabi, 2002). An inclusion is a region contained inside an homogeneous elastic solid that has undergone inelastic deformation (Eshelby, 1961). It is widely agreed that crack initiate more easily at larger intrusions (Mughrabi, 2002; Billaudeau and Nadot, 2004; Itoga et al., 2003; Murakami et al., 1999). The critical intrusion size depends on the specific material. In the particular case of 2124-T4 aluminum alloys (Al_2CuMg), the probability of crack initiation at inclusions smaller than 6 μm decreases rapidly (Kung and Fine, 2007). It has been reported that inclusions located deeper into the material tend to be larger compared to those located at the surface (Yang et al., 2004). For that reason, internal cracks are more likely to initiate at larger inclusions lying deep into the material (Itoga et al., 2003).

Another important parameter influencing the type of failure is the volumetric density of inclusions. Mughrabi (2002) established two necessary conditions for internal crack to nucleate, namely (1) the existence of extrinsic defects at which cracks can initiate, such as non-metallic inclusions, pores of cavities and (2) a critical volumetric density of inclusions below which surface failure is inhibited. Assuming a cylindrical specimen and spherical inclusions, Mughrabi (2002) deduced a critical volumetric density of inclusions as function of the specimen thickness d and external area A:

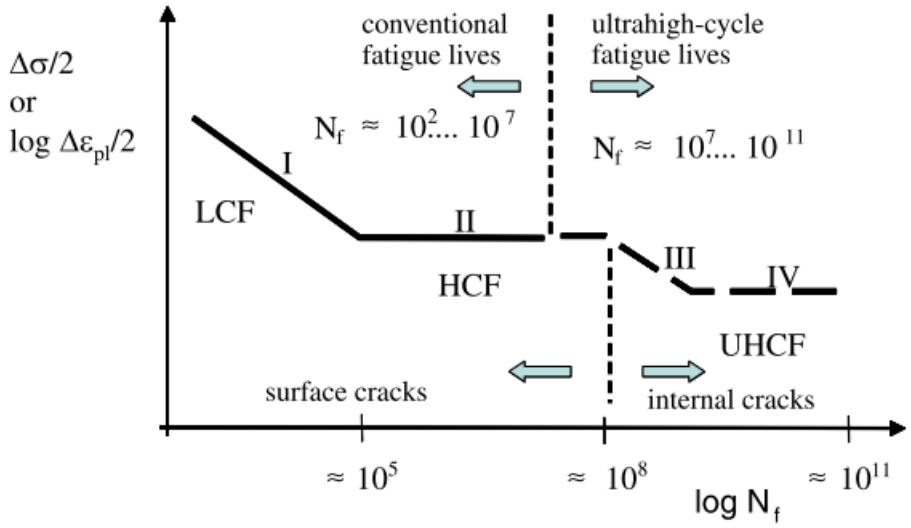

Figure 1.8: Multi-stage life diagram for Type II materials.
Source: Mughrabi (2006).

$$n_c = \frac{1}{dA} \tag{1.2}$$

For volumetric densities below n_c, no inclusion can be found within the external layer of thickness d. As a consequence, crack initiation at inclusions located inside the external layer can be neglected. In this case, crack initiation occurs at the internal inclusions. For volumetric densities above n_c, the probability of crack initiation at inclusions located inside the external layer increases. At the same time, crack initiation can occur at the internal inclusions. However, it has been reported (Mughrabi, 2002; Billaudeau and Nadot, 2004) that internal crack propagation is slow with respect to cracks propagating from the surface. For that reason, internal failure is only privileged for volumetric densities below n_c.

Figure 1.8 shows the typical fatigue life diagram of type II materials. In ranges I and II (LCF and HCF regimes) most cracks initiate at inclusions located just below the surface. However, it has been reported that cracks can also initiate at internal inclusions, although much less frequently (Sakai, 1999; Nishijima and Kanazawa, 1999). The analogous situation occurs in ranges III and IV (UHCF regime). Although most cracks initiate at internal inclusions, there is experimental evidence (Sakai, 1999; Nishijima and Kanazawa, 1999) that surface failure can also occur to a lesser extent. When the volumetric density of inclusions lies below the critical value, the fatigue mechanisms in range III are similar for materials of type I and II. Under this condition, crack initiation at the surface inhomogeneities would be the dominant fatigue mechanism (Mughrabi, 2002).

1.2.2 A brief overview on cyclic-fatigue simulations

Most cyclic-fatigue simulations have been done using the Finite Element Method (FEM) coupled with the Continuum Damage Mechanics (CDM) framework (Takagaki and Nakamura, 2007; Hilgendorff et al., 2013; Bhamare et al., 2014; Pandey et al., 2021). CDM is a branch of classical continuum mechanics dedicated to the study of fatigue. In the CDM framework, the average microstructural degradation is represented by the damage variable (Lemaitre and Chaboche, 1994). Therefore, the overall effect of crack initiation and propagation can be represented in an unified manner via the damage variable, which continuously varies from zero to one. At the initiation stage, the damage variable value increases under the influence of mechanical loading. When a certain value of damage is reached, the crack initiates. A further increase of the accumulated damage causes the crack to propagate. The material finally breaks when the damage variable acquires the value of one (Lemaitre and Chaboche, 1994). The evolution equation of the damage variable is known as the damage law. Many models have been proposed to predict the fatigue life of materials on the HCF regime, most notably the damage laws developed by Kachanov (1958), Chaboche and Lesne (1988), Paas et al. (1993), Xiao et al. (1998), Lemaitre et al. (1999), Peerlings et al. (2000) and Abdel Wahab (2001). In general, the damage laws are expressed as functions of the stress or strain. Therefore, the FEM has been used to calculate the stress and strain at each Gauss point of the representative volume.

The numerical simulation of fatigue crack propagation based on fracture mechanics and the conventional FEM is computationally expensive (Takagaki and Nakamura, 2007). For that reason, Takagaki and Nakamura (2007) proposed to implement the anisotropic theory of CDM developed by Chow and Wang (1987a,b, 1988) and their own damage law in the finite element code FINAS. They simulated the propagation of multiple cracks in 316L steel subjected to LCF. Based on their simulation results, failure occurred at the 1298th cycle. Their simulated crack length as function of the cycle number was in good quantitative agreement with experimental results. More recently, Pandey et al. (2021) simulated the propagation of cracks under LCF using the eXtended Finite Element Method (XFEM). In contrast with the work of Takagaki and Nakamura (2007), the XFEM results are mesh-independent. The XFEM was developed by Belytschko and Black (1999) based on the theory of Melenk and Babuška (1996) and Duarte and Oden (1996). The XFEM allows discontinuities to exist within a finite element by implementing enrichment functions at certain nodes (Pascoe et al., 2013). Therefore, the XFEM can be considered as a "meshless" FEM, which allows to simulate crack growth without having to define a crack plane (Pascoe et al., 2013). In an older work, Murakami and Liu (1995) showed

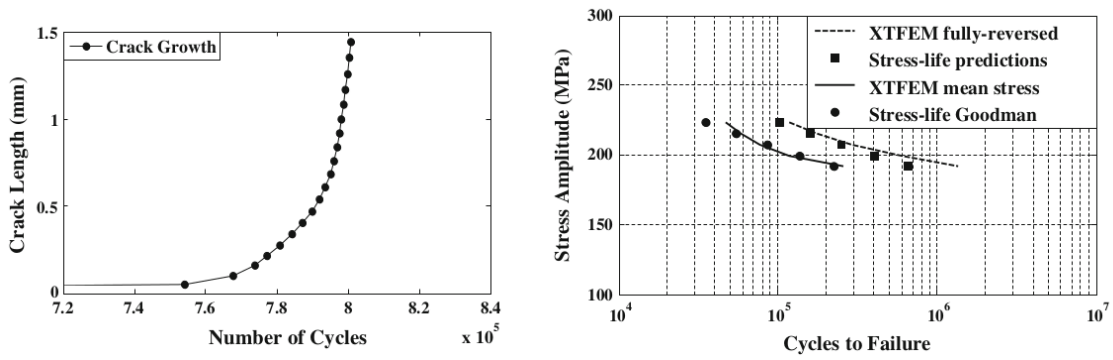

Figure 1.9: Crack growth simulations (left image) and fatigue-life diagram of stainless steel (right image).
Source: Bhamare et al. (2014).

that exponential damage laws are less mesh-dependent with respect to power-based damage laws. For that reason, Pandey et al. (2021) proposed a new exponential law for the damage increment per cycle, which they used in their model to simulate crack propagation under LCF in stainless steels and aluminum alloys. Their fatigue-life diagrams obtained from simulations were in good quantitative agreement with their experimental results.

HCF simulations typically require extrapolation techniques to simulate a large number of cycles. In the conventional jump-in-cycle method (Cojocaru and Karlsson, 2006), the damage values are stored during one full cycle. Afterwards, the damage values of the next block of cycles are obtained by extrapolation. The process is iteratively repeated for a large number of cycles. However, Zhang et al. (2012) showed that the jump-in-cycles method generates stable results only for sufficiently small number of cycles. On the other hand, space-time methods are known to be unconditionally stable (Hughes and Hulbert, 1988; Hulbert and Hughes, 1990). In order to simulate a large number of cycles without having to rely on the jump-in-cycle procedure, Bhamare et al. (2014) developed the eXtended space-Time Finite Element Method (XTFEM) based on the time-discontinuous Galerkin formulation (Chessa and Belytschko, 2004; Chirputkar et al., 2008). In their work, the XTFEM was coupled with the two-scale CDM (Lemaitre et al., 1999; Desmorat et al., 2007) to evaluate the irreversible-damage accumulation. As a result, Bhamare et al. (2014) were able to successfully simulate more than one million fatigue cycles using the commercial FEM code LS-DYNA. In particular, they obtained the fatigue-life diagrams of stainless steel, along with the crack length evolution as function of the cycle number. Their simulations were in good quantitative agreement with the experimental results (see figure 1.9). In recent years, Zhang et al. (2019) drastically improved the numerical efficiency of the XTFEM-CDM method (Bhamare et al.,

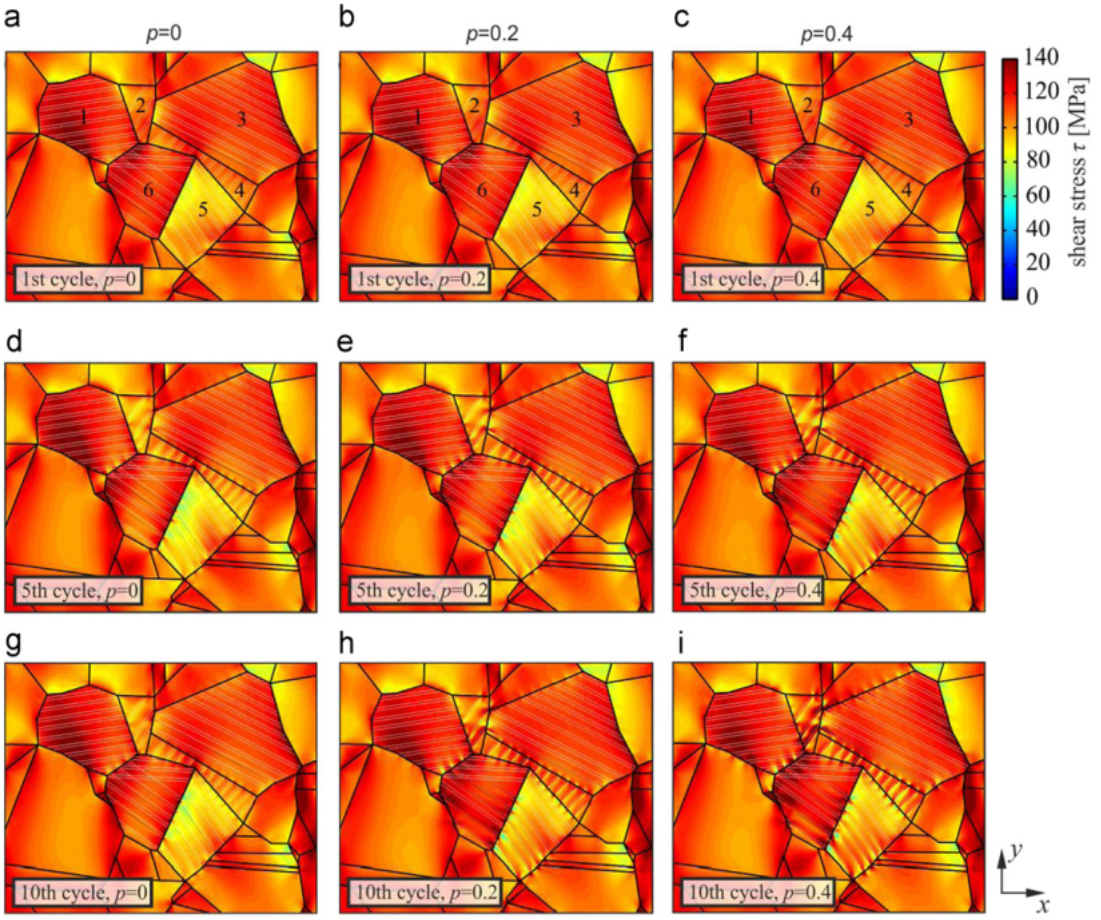

Figure 1.10: Shearing-stress contours at the most critical slip systems. An increased cyclic slip irreversibility is associated to a larger number of experimental cycles. Figures (a)-(c) show the effect of cyclic slip irreversibility after one cycle, (d)-(f) five cycles and (g)-(i) ten cycles.
Source: Hilgendorff et al. (2013).

2014) using parallel computing.

The damage mechanisms under VHCF have been thoroughly studied using diverse simulation methods. Fatigue cracks are known to initiate at the slip bands (Mughrabi, 2002). For that reason, slip bands are considered to be the first sign of fatigue damage (Man et al., 2003). Hilgendorff et al. (2013) simulated the formation, sliding, irreversibility and hardening of slip bands using the two-dimensional Boundary Element Method (BEM) (Aliabadi, 2002). In their method, the slip band was approximated as two closely separated layers. Therefore, the slip band evolution was determined by the sliding distribution between these two layers. Once a critical resolved shear stress was exceeded, one layer started to slide with respect to the other. Another contribution to the sliding distribution was the total irreversible

displacement per cycle, which was directly proportional to the total displacement per cycle. The proportionality constant was given by the cyclic-slip irreversibility as a free parameter. They simulated only a few cycles due to the generic computational limitations. In order to simulate the slip bands after 10^7 experimental cycles, the value of cyclic-slip irreversibility was increased (see figure 1.10). The simulated slip bands were in qualitative agreement with their electron-microscopy images (Hilgendorff et al., 2013, 2014, 2016a,b).

In the last two decades, finite element simulations have achieved an unrivaled success on fatigue-life prediction. However, all the finite element methods for fatigue simulations must be coupled with constitutive laws at the macroscopic scale, which invariably depend on empirical constants. In other words, most of the recent progress on fatigue-life prediction has been based on the amelioration of empirical laws to better fit the latest experimental data (Pascoe et al., 2013). In order to predict fatigue-life diagrams without having to rely on experimental results, the empirical laws used in simulations must be replaced by the appropriate physical models. Macroscale continuum simulation methods such as the FEM aim to describe the effect of the physical phenomena occurring at the microscale[1] and mesoscale[2] using constitutive relations. Experimental results or even simulations at the mesoscale are typically employed to develop the appropriate constitutive relations due to their more fundamental nature. Mesoscale methods such as Discrete Dislocation Dynamics (DDD) are specifically designed to track the evolution of microstructural defects. DDD was developed to simulate plastic deformation through the motion of dislocations under the influence of stress (El-Awady et al., 2008). In contrast to FEM simulations, the DDD framework does not require the specification of elastic-plastic constitutive laws to study plastic deformation (Olarnrithinun, 2013). As an example, DDD have successfully provided physically-based simulations of the most crucial fatigue mechanisms, such as crack initiation (Deshpande et al., 2003a; Brinckmann and Van der Giessen, 2003, 2004; Déprés et al., 2004a; Tran and Homma, 2009), crack growth (Cleveringa et al., 2001; Deshpande et al., 2001, 2003b; Huang et al., 2014) and crack propagation (Déprés et al., 2012, 2014, 2015; Deshpande et al., 2001; Prasad Reddy et al., 2013).

The fatigue mechanisms occurring during the firsts cycles of the LCF regime have been studied using DDD simulations. In the work of Déprés et al. (2006), the DDD code TRIDIS (Verdier et al., 1998) was used to estimate the number of cycles to micro-crack initiation in 316L steel during LCF. In TRIDIS (Verdier et al., 1998), the DDD framework is coupled with the FEM to calculate the image forces induced by the presence of a free surface. Considering a single grain, they

[1] Scale between picometers and a few nanometers.
[2] Scale between nanometers and a few micrometers.

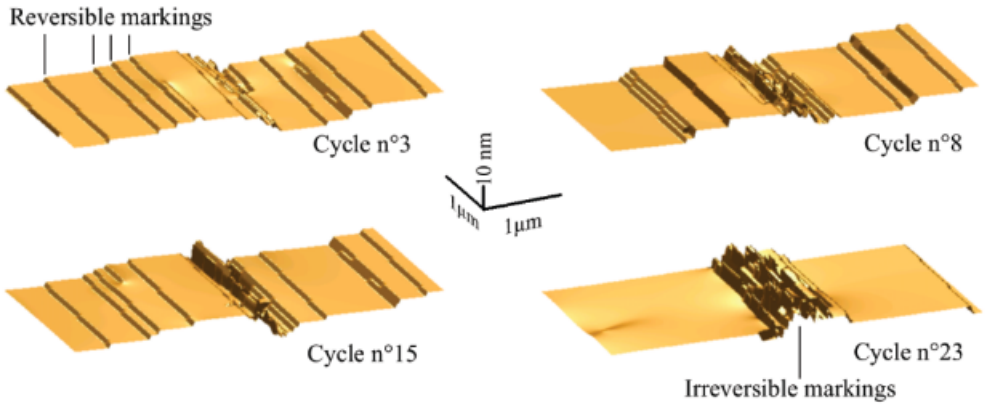

Figure 1.11: Evolution of the slip markings at the same position of the surface. *Source:* Déprés et al. (2006).

quantified the size of intrusions and extrusions formed at the crystal surface during cyclic loading (see figure 1.11). Therefore, Déprés et al. (2006) were able to calculate the growth rate of surface markings at the crystal boundary from the simulation of 35 cycles. By defining a crack as a 3-μm-deep intrusion, they estimated the number of cycles required for crack initiation. According to the calculations of Déprés et al. (2006), cracks in 316L steels initiate after 3459 cycles at an applied plastic strain amplitude of 10^{-3}. As an important conclusion of their work, they emphasized the role of cross-slip on the formation and growth of PSBs. Years later, El-Achkar and Weygand (2019) used DDD simulations to study the dislocation microstructures formed on Face-Centered Cubic (FCC) Aluminum during LCF. They simulated up to 160 cycles in the range of applied plastic strain amplitudes between 10^{-3} and 10^{-2}. In their work, El-Achkar and Weygand (2019) provided a statistical description of the stable defects formed during cyclic loading, such as prismatic loops, sessile junctions, dislocation dipoles and surface steps (see figure 1.12). In agreement with the conclusions of Déprés et al. (2006), El-Achkar and Weygand (2019) emphasized the importance of cross-slip on the emergence and evolution of PSBs. In the present year, Meng et al. (2021) used the TRIDIS code (Verdier et al., 1998) to analyze the microstructural damage of FCC copper and 316L steel subject to LCF. They simulated up to 80 fatigue cycles in the range of applied plastic strain amplitudes between 0.6×10^{-3} and 1.5×10^{-3}. According to Meng et al. (2021), PSBs emerged more easily in copper than in 316L steel due to the higher cross-slip probability of screw dislocations in copper.

A few years ago, El-Achkar and Weygand (2018) used DDD simulations to study the irreversible changes occurring on the microstructure of FCC Aluminum in the VHCF regime. They simulated up to 50 loading cycles at applied plastic strain am-

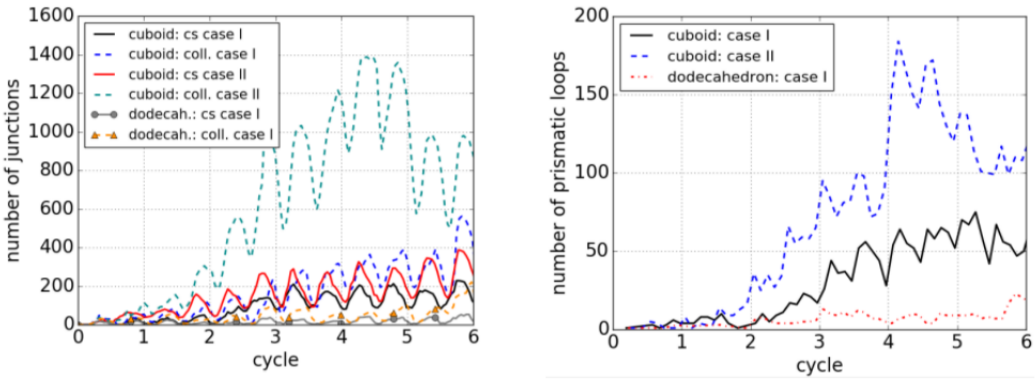

Figure 1.12: Number of junctions (left-handed image) and prismatic loops (right-handed image) formed during the firsts cycles of the VHCF regime. Notice that the simulation box' symmetry affected the number of structures formed during cyclic loading.
Source: El-Achkar and Weygand (2018).

plitudes in the range between 5×10^{-6} and 5×10^{-5}. In their work, El-Achkar and Weygand (2018) used dislocation-network analysis to study the dislocation structures formed during cyclic loading. They measured a higher concentration of irreversible changes in the crystal regions where cross-slip was most likely to occur. A possible explanation might be that cross-slip enables the formation of prismatic loops, which can act as obstacles to other gliding dislocations (Erel et al., 2017a). For that reason, prismatic loops are believed to play a significant role in strain hardening of FCC metals (Erel et al., 2017a). El-Achkar and Weygand (2018) concluded that the persistent roughness formed at the crystal surface was due to the irreversible motion of prismatic loops and dislocation dipoles gliding along the channels of plastic slip.

The cross-slip mechanism plays thus an important role on realistic DDD simulations. Cross-slip is a thermally activated process that strongly depends on the local stress acting on the screw dislocations. Molecular Dynamics (MD) can provide an appropriate time scale to accurately simulate a single cross-slip event. For sufficiently small screw dipoles, one of the screw dislocations can spontaneously cross-slip, glide on the deviated plane and annihilate the other dislocation (Vegge et al., 2000). For that reason, screw dipoles have been simulated using molecular dynamics to quantify the average waiting time required for an spontaneous cross-slip event to occur. The reciprocal of said waiting period is known as the cross-slip rate. In the past two decades, molecular dynamics have provided a few quantitative results of the cross-slip rates at different stress conditions and temperatures (Vegge et al., 2000; Mordehai et al., 2005; Oren et al., 2017; Esteban-Manzanares et al.,

2020). However, most DDD simulations have been based on cross-slip models unable to reproduce quantitative atomistic results. Following the pioneering work of Kubin et al. (1992), the cross-slip of screw dislocations in most DDD simulations is implemented using the kinetic Monte Carlo method. Based on the cross-slip rate proposed by Kubin et al. (1992), the vast majority of the rate models implemented on DDD simulations were expressed as function of the Schmid stress applied on the glide plane or the deviate plane (Déprés et al., 2004a). Two decades later, Kang et al. (2014) used molecular dynamics to quantity the effect of Schmid and Escaig stresses on the activation enthalpy of cross-slip. They showed that both Schmid and Escaig stresses have a comparable effect on the activation enthalpy of cross-slip. For that reason, the full effect of the stress components must be considered on the cross-slip rate in order to reproduce atomistic results. More recently, Hussein et al. (2015) proposed a new cross-slip rate model in which the main stress component is the difference of Escaig stresses on the glide and cross-slip planes. However, their model is incomplete because it neglects the effect of Schmid stress on the deviate plane. A few years later, Malka-Markovitz and Mordehai (2019) proposed an analytical expression for the activation enthalpy of cross-slip that considers the full effect of all stress components. Shortly after, Esteban-Manzanares et al. (2020) deduced a general model for the cross-slip rate by coupling the Harmonic Transition State Theory with the Meyer-Neldel rule.

Based on the notable research of Malka-Markovitz and Mordehai (2019) and Esteban-Manzanares et al. (2020), the present manuscript introduces the first quantitative DDD methodology that is able to reproduce the cross-slip rates of screw dislocations found from atomistic simulations. In contrast with previous works, the present cross-slip model does not rely on any fitting parameters nor empirical results. For that reason, the physical properties of solids calculated using the present DDD methodology can be now directly compared with quantitative experimental results. One important drawback of DDD simulations with respect to macro-scale methods is that they are computationally more expensive. Therefore, only a limited amount fatigue cycles can be performed. In order to study the system evolution on the VHCF regime after a large number of cycles, a new time-coarsening algorithm for DDD simulations is proposed.

In the following section, a more detailed overview of the present manuscript is given.

1.3 Thesis structure

The present thesis is structured as follows:

- Chapter 2 introduces the cross-slip framework by giving clear definitions of all dislocation types, establishing unambiguous rules to predict in which direction a perfect dislocation would move and then employing those rules to understand the effect of each stress component on the geometry and motion of extended dislocations.

- Chapter 3 shows that the activation enthalpy of cross-slip obtained from DDD simulations can be well fitted with two line tension models of cross-slip, namely the numerical model of Kang et al. (2014) and the analytical expression of Malka-Markovitz and Mordehai (2019). For that reason, it was concluded that those line tension models could be reliably used in DDD codes to calculate the activation enthalpy of screw segments.

- Chapter 4 proposes to compute the cross-slip probability of screw segments using the rate equation proposed by Esteban-Manzanares et al. (2020) and the general expression for the activation enthalpy obtained by Malka-Markovitz and Mordehai (2019) to remove the scaling factors often required in cross-slip models. The annihilation rates of a screw dipole obtained from the DD simulations were in quantitative agreement with the atomistic results of Vegge et al. (2000) and Oren et al. (2017), which demonstrates that the presented DDD methodology was able to reproduce atomistic results without any fitting parameters.

- Chapter 5 shows some qualitative applications of the recently benchmarked cross-slip modeling described in chapter 4 to cyclic fatigue simulations. The objective was to study the effect of cross-slip on two simple microstructural configurations in FCC copper, namely on one isolated dislocation, and on twelve dislocations with an arbitrary angle between their Burgers vector and line direction. It was found that even forcing an isolated dislocation to cross-slip did not cause any cyclic irreversibilities, whereas some segments of the configuration with twelve dislocations naturally cross-slipped due to strong internal stress on certain dense parts of the configuration, provoking irreversible changes in the microstructure due to reactions between dislocations. It was confirmed that the physical description of the cross-slip mechanism plays an important role on realistic DDD simulations.

- Chapter 6 summarizes the main conclusions of the present manuscript and proposes a novel time-coarsening method to simulate a larger number of cycles in the future.

Chapter 2

Theory of dislocations

Dislocations are crystallographic defects within a regular crystal structure. The first experimental evidence of dislocations was provided by Ewing and Rosenhain (1899), who formally announced the existence of slip-bands on metals subjected to mechanical loading. According to their studies, the plastic deformation was attributed to the relative slip of crystalline planes. Years later, Volterra (1907) studied the elastic fields generated by elementary deformations of isotropic continuous media. Although some of the deformed configurations that he proposed were later on used to describe real dislocations, his work included more general defects that are not normally found in regular metals. The discovery of X-rays by Röntgen (1896) enabled Darwin (1914) and Ewald (1917) to study the crystalline structure of metals. They found that the diffracted intensity was about twenty times larger than expected for a perfect crystal. Moreover, the diffracted-beam width was also many times larger than expected for a perfect crystal. Due to these discrepancies, real crystals were envisioned as an array of slightly misoriented crystallites glued together by an amorphous material. According to said theory, the diffracted intensity was associated to the crystallite size, whereas the diffracted-beam width accounted for the misorientation between crystallites (Anderson et al., 2017). Based on the theory of a perfect crystalline solid, Frenkel (1926) postulated an expression for the applied

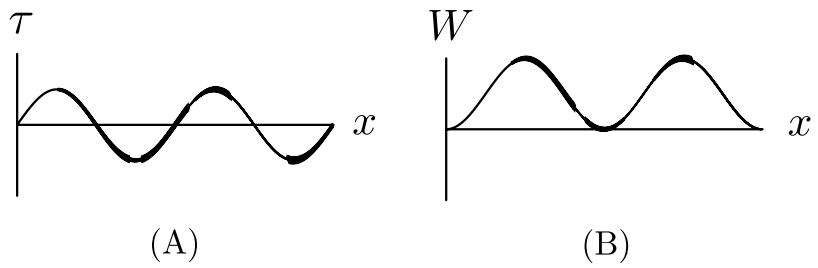

Figure 2.1: Model of Frenkel (1926) for: (A) the shear stress τ as function of the relative displacement x and (B) the periodic lattice potential W as function of x. *Source*: figure adapted from Anderson et al. (2017).

shear stress τ as function of the relative shear displacement x. Assuming a periodic crystalline lattice with period equal to the Burgers vector of magnitude b, Frenkel (1926) approximated the corresponding potential energy W using a trigonometric function (see figure 2.1):

$$W(x) = 1 - \cos\left(\frac{2\pi}{b}x\right) \implies \tau = \tau_0 \sin\left(\frac{2\pi}{b}x\right) \tag{2.1}$$

where τ_0 is the theoretical shear strength of the crystal. Assuming that the relative shear displacement is much smaller than the Burgers' vector magnitude, the applied stress reduces to:

$$\tau = \frac{2\pi\tau_0 x}{b} \tag{2.2}$$

Under the condition of small displacements, the Hooke's law can be applied:

$$\tau = \mu\gamma = \mu\frac{x}{a} \tag{2.3}$$

where γ is the strain, μ the elastic shear modulus and a the interplanar distance. Combining equations 2.2 and 2.3, an expression for the theoretical shear strength can be deduced:

$$\tau_0 = \frac{\mu b}{2\pi a} \tag{2.4}$$

Assuming that the interplanar separation is similar to the Burgers vector magnitudes, a simpler expression for the theoretical shear strength is obtained:

$$\tau_0 = \frac{\mu}{2\pi} \tag{2.5}$$

which gives an approximate value of $\tau_0 \approx 0.2\mu$. In strong disagreement, experiments performed at the time of Frenkel's work measured values the theoretical shear strength between $10^{-4}\mu$ and $10^{-3}\mu$ (Anderson et al., 2017). A few years later, Orowan (1934a,b), Polanyi (1934) and Taylor (1934) postulated the existence of edge dislocations to explain the discrepancy between theoretical and experimental values of the shear strength. Shortly after, Burgers (1939) proposed the existence of screw dislocations in metals.

In the following sections, a more rigorous description of dislocation encountered in real crystalline solids is given. The present chapter introduces the framework required to explain the cross-slip process of screw dislocations affecting the fatigue of materials. Section 2.1 defines all dislocation types and provides rules describing their motion under the influence of shearing stress. Said rules are used in section 2.2 to understand the effect of stress on extended dislocations composed by two Shockley partials in FCC metals. Finally, section 2.3 provides equations for the

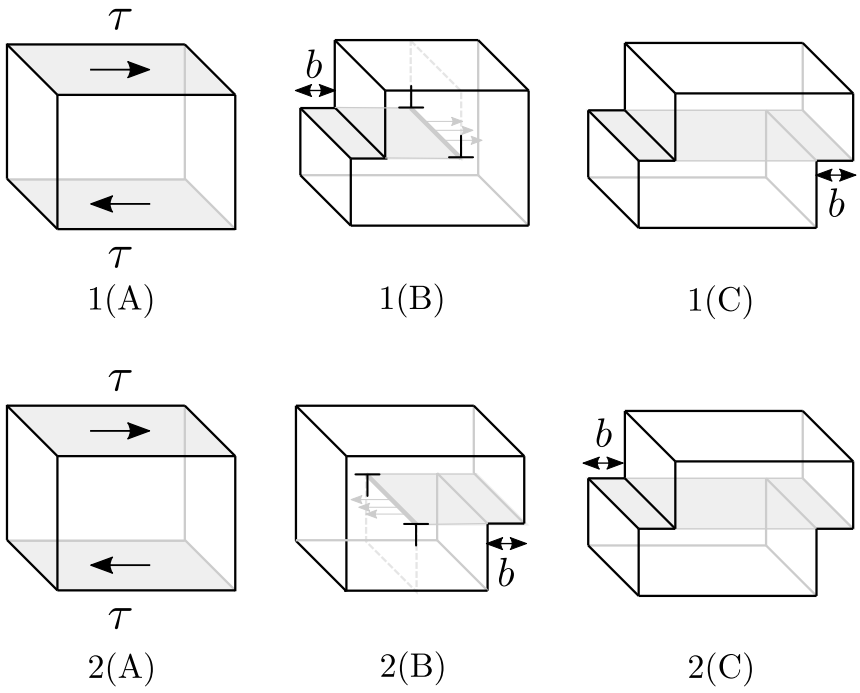

Figure 2.2: Movement under shearing stress of: 1(A)-1(C) a right-handed edge dislocation and 2(A)-2(C) a left-handed edge dislocation. The segmented line indicates the extra half-plane, the gray solid line represents the dislocation line and the shaded area shows the slipped surface.
Source: figure adapted from Anderson et al. (2017).

stress components affecting the dislocation width and glide of extended dislocations, which are employed on the next chapter to describe the influence of stress on the cross-slip process of extended screw dislocations.

2.1 Perfect dislocations

2.1.1 Dislocation types

Real metals are not perfect crystalline structure because they typically contain defects. The particles of perfect crystalline solids form a periodic arrangement among all available lattice planes. When a perfect crystalline solid undergoes an applied stress, the constituent atoms rearrange themselves on the crystalline planes causing local regions of deformation. A shearing stress provokes a relative shear displacement when parts of the solid material move respect to others along the crystalline planes. Consider the shearing stress τ applied on the upper part of the perfect crystal as shown in figure 2.2 1(A). Due to the relative shearing displacement b across one crystalline plane, an extra half-plane was created on the upper part of the crys-

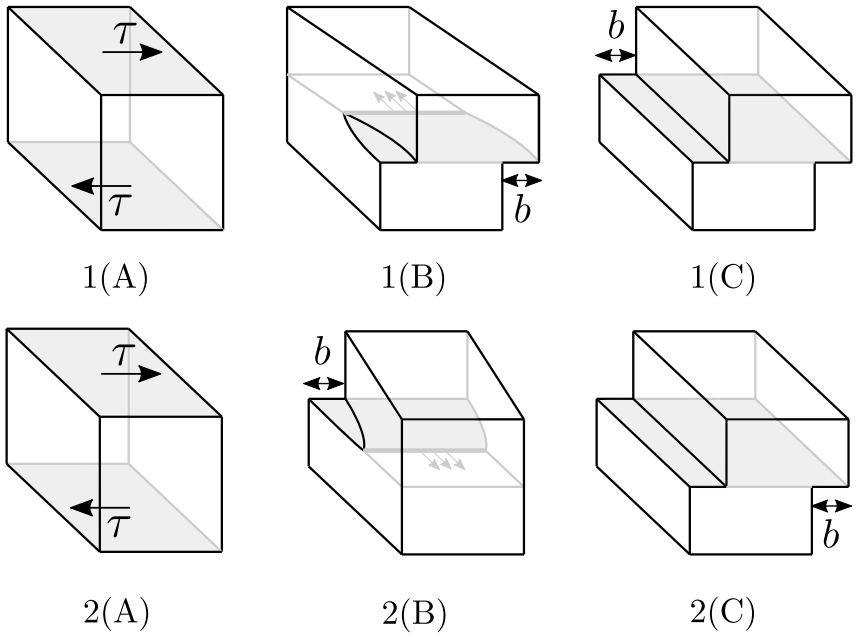

Figure 2.3: Movement under shearing stress of: 1(A)-1(C) a right-handed screw dislocation and 2(A)-2(C) a left-handed screw dislocation. The shaded area indicates the slipped surface and the gray solid line represents the dislocation line.
Source: figure adapted from Anderson et al. (2017).

tal as shown in figure 2.2 1(B). Said extra half-plane consists of a right-handed edge dislocation that provokes local deformation on the otherwise perfect structure. A right-handed edge dislocation is represented with the symbol $\perp$ because its relative displacement is perpendicular to the extra half-plane (Anderson et al., 2017). Interpreted graphically, the symbol points out towards the extra half-plane. As a dislocation propagates across the glide plane, the atomic planes above the sheared area undergo a relative shear displacement with respect to the lower part of the crystal. Moving through the glide plane, the dislocation finally exits the crystal leaving a step of magnitude b as shown in figure 2.2 1(C). As a result, the external crystal surface acquires a step of size b at the glide plane. A left-handed edge dislocation is represented with the symbol $\top$. In contrast with right-handed dislocations, the extra half-plane appears on the negative side of the surface where stress is applied. As a consequence, right-handed edge dislocations move in the direction of applied shearing stress, whereas left-handed edge dislocations move in the exact opposite direction (see figure 2.2 2(B)).

Edge dislocations are simpler to visualize than other more complex structures such as screw dislocations. In contrast with the direct visual image of an extra half-plane inserted in the structure, a screw dislocation is visualized by cutting across on plane and slipping both parts with shearing displacement b (see figures 2.3 1(B)

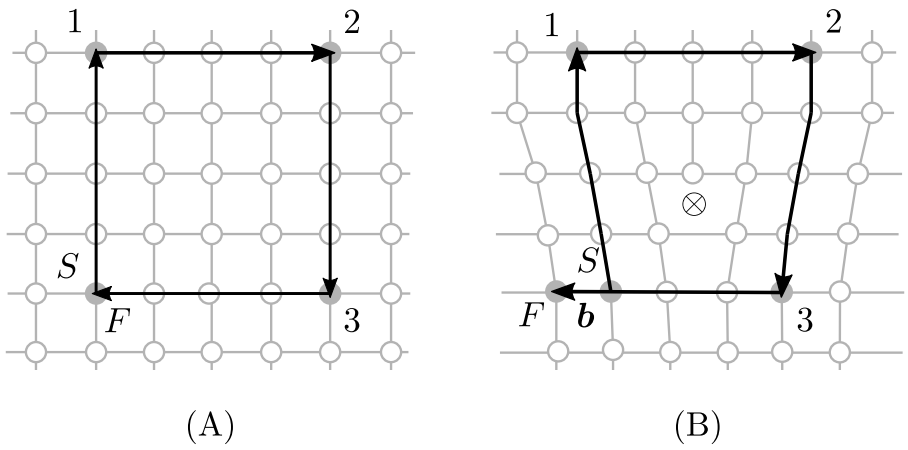

Figure 2.4: Burgers circuits based on the RH-SF convention in: (A) a perfect crystal and (B) a deformed crystal. The ⊗ symbol indicates that the line direction of the edge dislocation points into the page. The starting point of the circuit is denoted as S and the final point as F.
Source: figure adapted from Anderson et al. (2017).

and 2.3 2(B)). The dotted gray line indicating where the cut ends represents the dislocation line. Similar to edge dislocations, the atomic planes above the sheared area undergo a relative shear displacement with respect to the lower part of the crystal. It implies that the dislocation line topologically separates the slipped and unslipped regions. Right-handed and left-handed screw dislocations move in opposite directions. When placing a right hand on the plane where stress is applied, a right-handed dislocation moves in the thumb's direction. Analogously, when placing a left hand on the plane where shear stress is applied, a left-handed dislocation also moves in the thumb's direction.

The following section presents an univocal definitions for both the shear displacement and the dislocation lines as vector quantities. Later on, section 2.1.3 provides clear rules to determine the motion of edge, screw and mixed dislocations.

2.1.2 Burgers vector definition

Dislocations can be unambiguously defined using two vectors: the unitary line direction $\hat{\boldsymbol{\xi}}$ tangent to the dislocation line and the Burgers vector $\boldsymbol{b}$ characterizing the direction and magnitude of the relative shear displacement. Once the line direction has been specified, the Burgers vector of the dislocation is defined by drawing a so-called Burgers circuit around the line direction. There are several conventions to draw Burgers circuits. Every established convention leads to the same Burgers vector provided that the lattice distortions around the dislocation line are small. Due to its specific adoption in several standard books such as Anderson et al. (2017) and

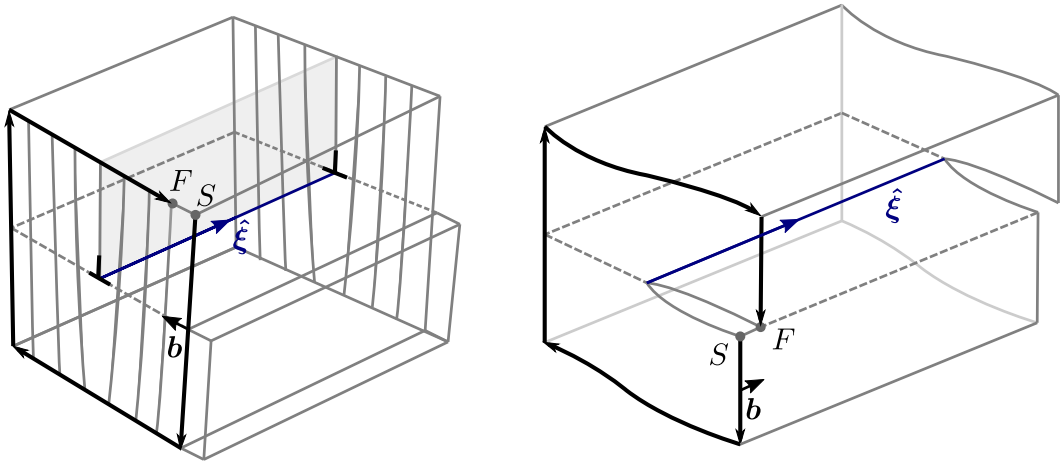

(A) (B)

Figure 2.5: Construction of a Burgers circuit around: (A) a right-handed edge dislocation and (B) a right-handed screw dislocation. The Burgers vector is parallel to the displacement vector that has its tail at point S and its head at point F. *Source*: figure adapted from Nix (2010).

Cai and Nix (2016), the right-handed, start-finish (RH-SF) convention will be used in this work. As a first step, an arbitrary right-handed loop is drawn in the perfect part of the crystal. Figure 2.4 (A) shows a Burgers circuit constructed around an arbitrary point of the perfect part of the crystal, consisting of four steps up, four steps right, four steps down, four steps left and four steps up, which results in the formation of a closed loop. As a second step, the same Burgers circuit is drawn around an existing dislocation using the right-hand rule. Figure 2.4 (B) shows that reproducing the same Burgers circuit around an edge dislocation prevents the loop from closing due to the lattice distortion. According to the RH-SF convention, the Burgers vector has its tail at the starting point S and its head at final point F on the distorted structure.

Figure 2.5 (A) shows an application of the RH-SF convention to find the Burgers vector on a right-handed edge dislocation. For the given line direction pointing into the crystalline structure, the chosen circuit denoted with black arrows show that the Burgers vector points towards the left. When a dislocation moves under the influence of stress, its motion is confined in a glide plane containing both the line direction $\hat{\boldsymbol{\xi}}$ and the Burgers vector $\boldsymbol{b}$. Notice that reversing the line direction leads to a Burgers vector pointing in the opposite sense. Since the extra half-plane is located on the other side of the plane for left-handed edge dislocations, the cross product between the line direction and the Burgers vector is reversed respect to right-handed edge dislocations. For that reason, the extra half-plane direction $\hat{\boldsymbol{n}}$

can be determined from the cross product of the line direction and the Burgers vector for both right-handed and left-handed edge dislocations:

$$\hat{\boldsymbol{n}} = \hat{\boldsymbol{\xi}} \times \boldsymbol{b} \tag{2.6}$$

Once an specific positive side of the glide plane has been defined, the extra half-plane of a right-handed edge dislocation is contained on the positive side of the glide plane, whereas the extra half-plane of a left-handed edge dislocation is contained on the negative side of the glide plane. For those reasons, a right-handed edge is also known as a positive edge and a left-handed edge is also referred as a negative edge. In sections 2.1.3 and 2.2.2, the positive side of the plane will be more concretely defined.

Figure 2.5 (B) shows an application of the RH-SF convention to find the Burgers vector of a right-handed screw dislocation. For the given line direction pointing into the crystalline structure, the chosen circuit denoted with black arrows shows that the Burgers vector is parallel to the line direction. As observed on the edge dislocations, the reversed line direction leads to a Burgers vector pointing in the opposite sense. In both cases, a right-handed screw dislocation satisfies $\hat{\boldsymbol{\xi}} \cdot \boldsymbol{b} > 0$. Since the relative shear displacements of left-handed and right-handed dislocations have opposite sense by definition, a left-handed dislocation satisfies $\hat{\boldsymbol{\xi}} \cdot \boldsymbol{b} < 0$. For those reasons, a right-handed screw is also known as a positive screw and a left-handed screw is also referred as a negative screw.

Each dislocation type moves on a different direction under the influence of shearing stress. A mixed dislocation can be decomposed on its screw and edge components. By knowing the direction in which pure screw and edge dislocations move, the direction of motion of a mixed dislocation can be inferred. Next section presents a helpful diagram used to predict on which direction an arbitrary dislocation would move in response to shearing stress.

2.1.3 Standard glide loop

Consider a dislocation loop oriented in the clockwise sense as indicated in figure 2.6. The Burgers vector of the dislocation loop shown was determined using the RH-SF convention. Although the local line direction changes at each point, the Burgers vector is an invariant quantity associated to the entire loop, which implies that each local dislocation type conforming the glide loop contributes to the same amount of shear displacement despite of moving on different directions. Because a dislocation produces shear displacement on the Burgers vector direction, the only shear component affecting the dislocation motion must be parallel to the Burgers vector. Expressed in terms of the Cartesian coordinate system shown in figure 2.6,

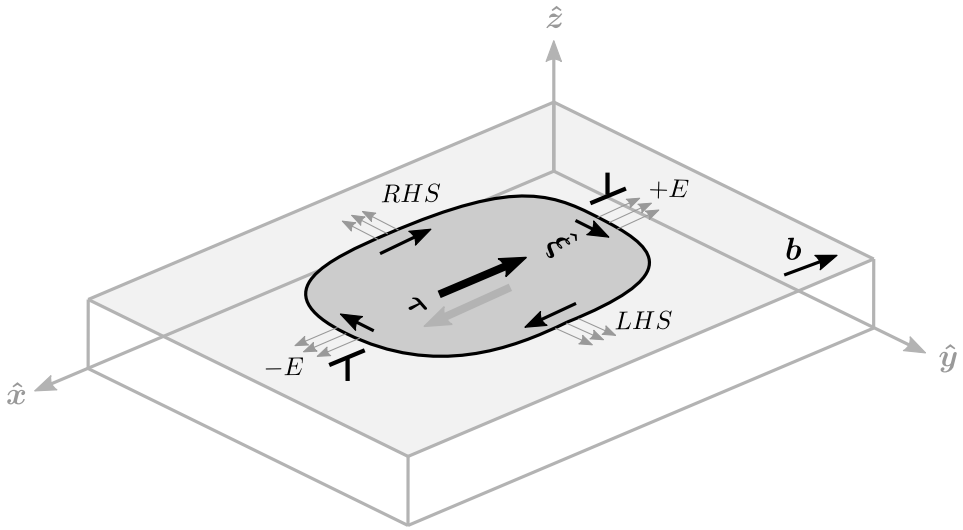

Figure 2.6: Standard glide loop formed by different dislocation types expanding under the influence of shearing stress. The region shaded in dark gray inside the glide loop indicates the slipped surface and the region shaded in light gray outside the glide loop indicates the unslipped surface.
Source: figure adapted from Nix (2010).

the Burgers vector of the dislocation loop is $\boldsymbol{b} = -b\hat{\boldsymbol{x}}$. A shearing stress equal to $\sigma_{xz} = -\sigma$ is therefore applied on the positive side of the z plane to set the dislocation loop into motion. Recall that the movement of each pure dislocation types was briefly discussed in section 2.1.1. It was deduced that under the influence of shearing stress, a right-handed screw (RHS) moves from right to left, a positive edge (+E) moves in the shearing direction, a left-handed screw (LHS) moves from left to right and a negative edge dislocation (-E) moves opposite to the shearing direction. These observations are consistent with the movement of each dislocation type conforming the glide loop. Moreover, the direction of motion is always perpendicular to the dislocation line. For these reasons, the glide loop expands under positive shearing stress. The pure dislocation types forming part of the glide loop are continuously joined together through the different mixed dislocation types. Since the shearing stress drives the motion of any dislocation with its Burgers vector parallel to the shear direction, the shearing plane defines what side of the glide plane is positive. Notice that the edge dislocation with its extra half-plane contained on the positive side of the glide plane is defined as a positive edge dislocation. Analogously, the edge dislocation with its extra half-plane contained on the negative side of the glide plane is defined as a negative edge dislocation.

Figure 2.7 shows the same standard glide loop from above. The diagram proposes a right-hand rule to predict in which direction a given dislocation would move under

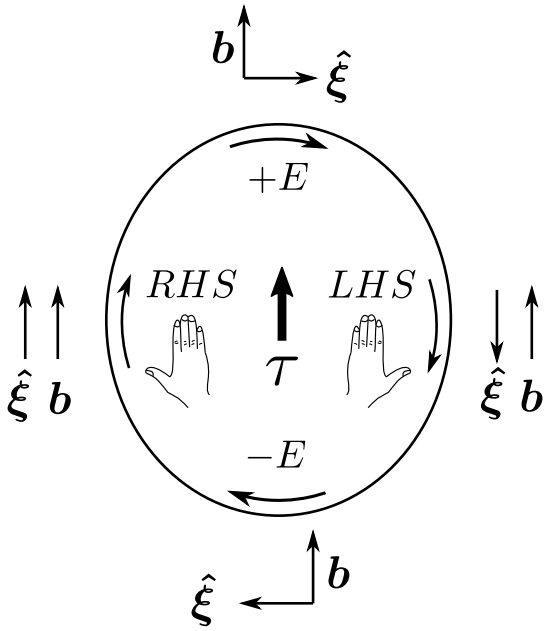

Figure 2.7: Standard glide loop showing the hand rules to determine the exact direction in which dislocations would move according to their type.
Source: figure adapted from Nix (2010).

the influence of shearing stress. By laying a right hand on the shear plane with the fingers parallel to the shearing, a RHS dislocation would move in the direction indicated by the right thumb. As previously discussed, a positive edge dislocation simply moves in the direction of shearing. Analogously, by laying a left hand on the shear plane with the fingers parallel to the applied shearing, a LHS dislocation would move in the direction indicated by the left thumb. Finally, a negative edge dislocation simply moves opposite to the shearing direction.

The present section has discussed the direction of dislocation movement due to a shearing stress. For completion, the following section introduces the concept of a force acting on a dislocation due to a general stress state.

2.1.4 Forces on dislocations

The Peach-Köhler force acting on a dislocation of line direction $\hat{\boldsymbol{\xi}}$ and perfect Burgers vector $\boldsymbol{b}$ in response to a stress state $\boldsymbol{\sigma}$ is given by:

$$\boldsymbol{f}_{PK} = (\boldsymbol{\sigma} \cdot \boldsymbol{b}) \times \hat{\boldsymbol{\xi}} \tag{2.7}$$

It has a climbing component $\boldsymbol{f}_c$ perpendicular to the glide plane and a gliding component $\boldsymbol{f}_g$ parallel to the direction of motion (see figure 2.8). Obtaining the scalar version of equation 2.7, it can be deduced that the magnitude of said gliding

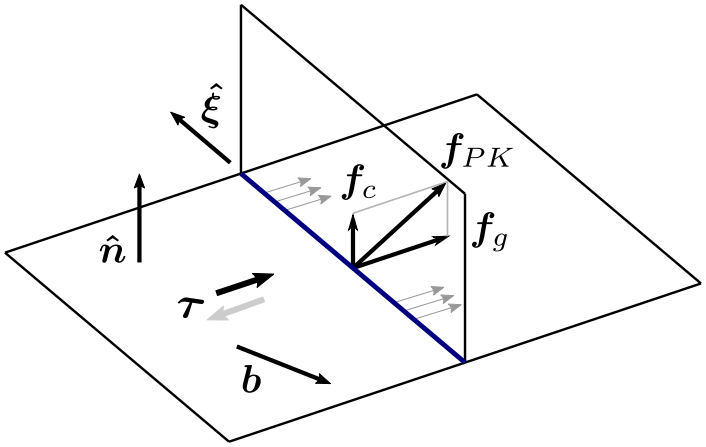

Figure 2.8: Mixed dislocation gliding due to a Peach-Köhler force having a climbing and a gliding component.

force is proportional to the shearing stress component parallel to the Burgers vector, also known as the gliding stress τ:

$$f_g = \tau b \tag{2.8}$$

The gliding stress can be expressed as (Kubin, 2013):

$$\tau = \boldsymbol{\sigma} \cdot \hat{\boldsymbol{n}} \cdot \hat{\boldsymbol{b}} \tag{2.9}$$

Equation 2.9 shows that the shearing stress is positive if the Burgers vector is parallel to the applied stress, whereas it is negative if the Burgers vector is anti-parallel to the applied stress. Substituting equation 2.9 into 2.8, another useful scalar version of the gliding force can be obtained:

$$f_g = \boldsymbol{\sigma} \cdot \hat{\boldsymbol{n}} \cdot \boldsymbol{b} \tag{2.10}$$

It is well-known that the force acting on the dislocation is parallel to its direction of motion, which according to section 2.2.3 is given by $\hat{\boldsymbol{n}} \times \hat{\boldsymbol{\xi}}$ for all dislocation types. Therefore, the vectorial equation of the gliding force can be also expressed on a simpler form:

$$\boldsymbol{f}_g = f_g(\hat{\boldsymbol{n}} \times \hat{\boldsymbol{\xi}}) \tag{2.11}$$

Perfect dislocations tend to dissociate into two partials to lower their elastic energy density. A perfect dislocation that has been dissociated into two partials is known as an extended dislocation. Due to the mixed character of partial dislocations, the effect of a general stress on the partial dislocations is more difficult to

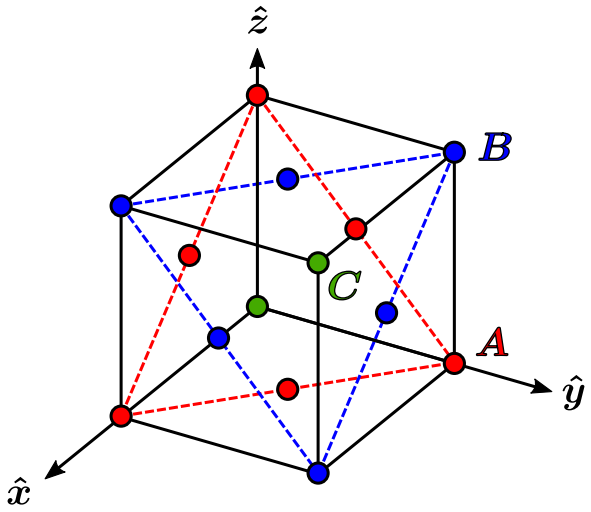

Figure 2.9: Unit cell showing the three different atomic layers of the FCC structure.

predict. The concept of Peach-Köhler force and the standard glide loop will be necessary to understand in which direction an extended dislocation would move under the influence of a shearing stress. Section 2.2 introduces the concept of extended dislocations, proposes a method to express an uniaxial stress into its relevant components and explains the effect of each stress component on extended dislocations.

2.2 Extended dislocations

2.2.1 Partial dislocations in FCC metals

The previous section was focused on the description of perfect dislocations based on the theory of continuum elasticity, where the relative shear displacement can take place on any direction. Although the continuum elasticity theory has been used to study important properties of crystalline solids, such as the elastic stress and strain fields provoked by dislocations, the relative shear displacement of crystalline solids is restricted to certain discrete directions. In order to understand the dislocation movement in crystalline solids, the particles constituting each atomic plane are assumed to be hard spheres bonded with their nearest neighbors. The Burgers vector of a perfect dislocation is therefore equal to the shortest translation vector of the crystalline lattice. In the FCC structure, the Burgers vector joins a corner of the cube to an atom at the center of a face, or equivalently, it joins the two atoms at the center of two neighboring faces. Plastic deformation occurs on the slip planes containing the Burgers vector, which are the most widely spaced atomic planes of the FCC structure. Figure 2.9 shows the three different atomic layers corresponding

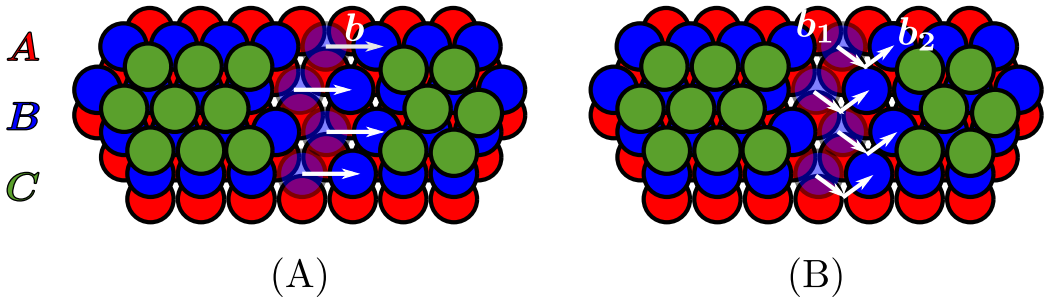

Figure 2.10: Displacement of atoms caused by the gliding of: (A) a perfect dislocation versus (B) an extended dislocation. Figure (A) shows how atoms on layer B end up on the same layer when displaced by an amount $\boldsymbol{b}$. Figure (B) shows that atoms on layer B end up on the layer C when displaced by an amount $\boldsymbol{b_1}$, which return to layer B after being displaced by an amount $\boldsymbol{b_2}$. All layers above the dislocation are displaced as well but only the layer B is shown for clarity.
Source: figure adapted from Zhigilei (2018).

to parallel slip planes. Each layer has a different atomic pattern despite belonging to the same family of planes. A dislocation located at a given slip plane would move under the influence of shearing stress by relative slip respect to the adjacent atomic layer. A given family of planes constitute an infinite amount of atomic layers stacked in the same periodic order such as $ABCABCABC$.

Figure 2.10 (A) shows a perfect dislocation at layer B gliding an amount $\boldsymbol{b}$ with respect to layer A. When the atoms that conform the perfect dislocation are moved by a lattice vector $\boldsymbol{b}$, all the atomic layers above are moved by the same amount as well. Recall that a particle displaced by a lattice vector end up on a translated atomic position of the same layer. For that reason, the stacking order of the atomic layers is preserved on both sides of the perfect dislocation, except that the two parts end up displaced by an amount $\boldsymbol{b}$ with respect to each other. The crystalline structure remains thus perfect on both sides of the dislocation line except for the relative shear displacement separating the two regions.

A more detailed study of the dislocation movement determined that dislocations do not directly slide a full lattice vector when moving from one atomic position to the other. As a matter of fact, the relative displacement of a full lattice vector is split into two partial movements. Figure 2.10 (B) shows a so-called extended dislocation in layer B slipping with respect to layer A. An extended dislocation consists of two partial dislocations known as the leading and trailing partials. Taking the direction of motion as a reference, the leading partial is located at the moving front whereas the so-called trailing partial follows behind it. In a first step, the atoms that are part of the leading partial moves an amount $\boldsymbol{b_1}$ with respect to the layer A. As

shown in Figure 2.10 (B), the leading partial on layer B ends up at the atomic positions of layer C. Because all particles are bounded with their nearest neighbors, the successive atomic planes above the leading dislocation undergo a transition such that $A \overset{\boldsymbol{b_1}}{\mapsto} B$, $B \overset{\boldsymbol{b_1}}{\mapsto} C$ and $C \overset{\boldsymbol{b_1}}{\mapsto} A$. The leading partial thus provokes a so-called stacking-fault on the atomic layers between the two partials, which means that the original periodic arrangement $ABCABCABC$ between the atomic layers has been disrupted:

$$\begin{array}{c} ABCA|BCABC \\ \downarrow\downarrow\downarrow\downarrow\downarrow \\ CABCA \end{array} \tag{2.12}$$

where the vertical line indicates the dislocation position. A so-called intrinsic stacking-fault is formed between the partials due to the missing B layer:

$$ABCA|CABCA \tag{2.13}$$

When the trailing partial moves an amount $\boldsymbol{b_2}$ respect to the layer A, the trailing partial on layer C returns back to the B layer. As a consequence, the successive atomic planes above the trailing dislocation transition back to their original positions such that $A \overset{\boldsymbol{b_2}}{\mapsto} C$, $B \overset{\boldsymbol{b_2}}{\mapsto} A$ and $C \overset{\boldsymbol{b_2}}{\mapsto} B$:

$$\begin{array}{c} ABCA|CABCA \\ \downarrow\downarrow\downarrow\downarrow\downarrow \\ BCABC \end{array} \tag{2.14}$$

Consider that the leading partial had Burgers vector $\boldsymbol{b_2}$ instead. In that case, the original stacking order would be transformed to a higher-energy configuration:

$$\begin{array}{c} ABCA|BCABC \\ \downarrow\downarrow\downarrow\downarrow\downarrow \\ ABCAB \end{array} \tag{2.15}$$

that will spontaneously split into an extrinsic stacking fault made of a double fault of the type $ABCA|C|B$ involving a faulted prismatic loop. Since the slip provoked by the trailing partial restores the original stacking order of the atomic layers, one says that the leading partial creates a stacking-fault whereas the subsequent movement of the trailing partial removes it.

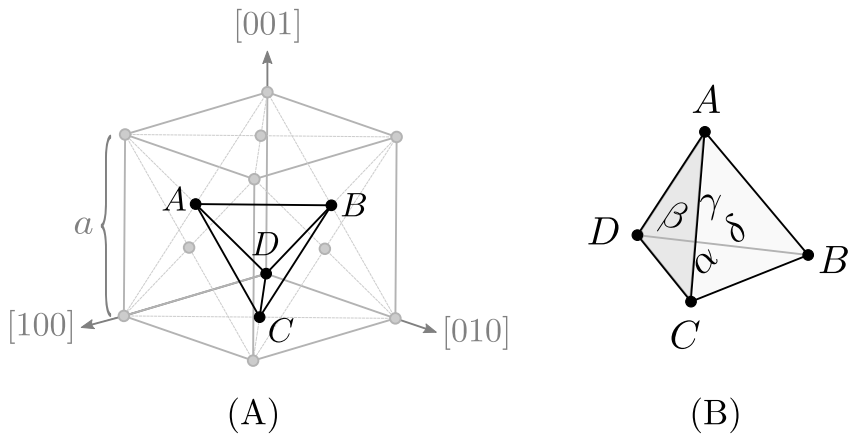

Figure 2.11: Illustrations of the Thompson tetrahedron showing: (A) the crystallographic position of the vertices at $A = \frac{a}{2}[101]$, $B = \frac{a}{2}[011]$, $C = \frac{a}{2}[110]$ and $D = [000]$ inside an FCC unit cell and (B) the notation for the unitary normals pointing inwards to the Thompson tetrahedron represented by Greek letters at the center of each triangular face, namely $\alpha = (1\bar{1}1)$, $\beta = (\bar{1}11)$, $\gamma = (11\bar{1})$ and $\delta = (\overline{111})$.
Source: figure adapted from Nix (2010).

In order to find the configuration of minimum energy, the Burgers vectors of the partials conforming an intrinsic stacking-fault must be obtained. The Thompson tetrahedron shows all the Burgers vectors of both perfect and partial dislocations in FCC metals. For that reason, the Thompson tetrahedron defined in section 2.2.2 will be used to find the intrinsic stacking-fault arrangement in section 2.2.3.

2.2.2 Thompson tetrahedron

The present section introduces the notation used on the Thompson tetrahedron and deduces how to construct it based on the FCC unit cell. Figure 2.11 (A) shows that the Thompson tetrahedron is obtained by joining four vertices of the FCC structure: one vertex at a cell corner and three vertices at the center of each neighboring face. An edge of the tetrahedron has an associated vector identified by two Roman letters, where the first Roman letter indicates the initial position of the tail, and the second Roman letter refers to the final position of the head. Notice that each closed-packed directions of the FCC structure is parallel to a vector formed by a pair of two different Roman letters, such that the tetrahedron edges represent the six Burgers vectors of the FCC structure. It can be also easily verified that the four faces of the Thompson tetrahedron are parallel to the closed-packed planes of the FCC structure, namely the $\{111\}$ family composed by the (111), $(\overline{1}\overline{1}1)$, $(\overline{1}11)$ and $(1\overline{1}1)$ directions. Recall that a family consists of crystallographically equivalent planes possessing the same atomic packing. The Greek letter centered at each triangular

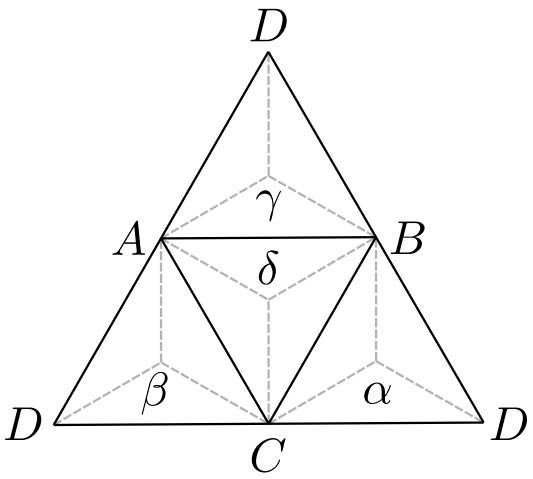

Figure 2.12: Two-dimensional representation of a Thompson tetrahedron. The gray segmented lines represent the Burgers vector of the partial dislocations.

Face α	Face β	Face γ	Face γ
$CB = \frac{a}{2}[\bar{1}01]$	$DA = \frac{a}{2}[101]$	$AD = \frac{a}{2}[\bar{1}0\bar{1}]$	$AB = \frac{a}{2}[\bar{1}10]$
$BD = \frac{a}{2}[0\bar{1}\bar{1}]$	$AC = \frac{a}{2}[01\bar{1}]$	$DB = \frac{a}{2}[011]$	$AC = \frac{a}{2}[01\bar{1}]$
$DC = \frac{a}{2}[110]$	$CD = \frac{a}{2}[\bar{1}\bar{1}0]$	$BA = \frac{a}{2}[1\bar{1}0]$	$BC = \frac{a}{2}[10\bar{1}]$
$C\alpha = \frac{a}{6}[\bar{2}\bar{1}1]$	$D\beta = \frac{a}{6}[211]$	$A\gamma = \frac{a}{6}[\bar{2}1\bar{1}]$	$A\delta = \frac{a}{6}[\bar{1}2\bar{1}]$
$B\alpha = \frac{a}{6}[1\bar{1}\bar{2}]$	$A\beta = \frac{a}{6}[\bar{1}1\bar{2}]$	$D\gamma = \frac{a}{6}[112]$	$B\delta = \frac{a}{6}[\bar{2}\bar{1}\bar{1}]$
$D\alpha = \frac{a}{6}[121]$	$C\beta = \frac{a}{6}[\bar{1}\bar{2}1]$	$B\gamma = \frac{a}{6}[1\bar{2}\bar{1}]$	$C\delta = \frac{a}{6}[\bar{1}\bar{1}2]$

Table 2.1: Burgers vectors of the Shockley partials in the FCC structure.

face of figure 2.11 (B) represents a unitary normal vector with its tail centered at the corresponding triangular face and its head pointing towards the opposite vertex facing the triangular surface, which means that said unitary vector point inwards to the Thompson tetrahedron. Notice also that the Greek letter associated to each triangular face corresponds to the Roman letter of the facing vertex, such that α points towards A, β points towards B, γ points towards C and δ points towards D.

Consider the two-dimensional representation of the Thompson tetrahedron depicted in figure 2.12. The three vertices of the resulting triangle represent the same point because the Thompson tetrahedron was unfolded with respect to the D vertex, namely the origin associated to the Cartesian system indicated in figure 2.11 (A). The solid lines represent the Burgers vectors having type $\frac{a}{2}\langle 110\rangle$ and magnitude $\frac{a}{\sqrt{2}}$, whereas the segmented lines refer to the Burgers vector of the Shockley partials having type $\frac{a}{6}\langle 112\rangle$ and magnitude $\frac{a}{\sqrt{6}}$. According to the notation used in the Thompson tetrahedron, the Burgers vectors of the Shockley partials are also vector quantities identified either by a Roman-Greek pair, or a Greek-Roman pair, where the first letter indicates the initial position of the tail, and the second letter refers to

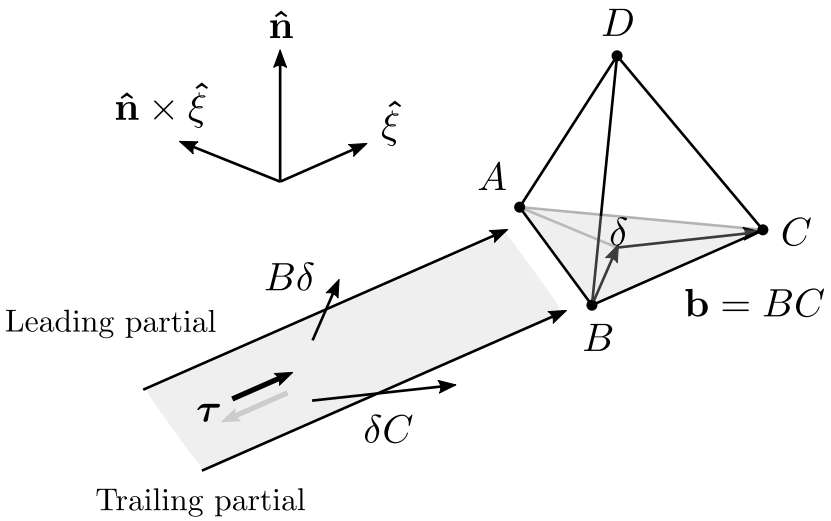

Figure 2.13: Extended RHS dislocation moving towards $\hat{\boldsymbol{n}} \times \hat{\boldsymbol{\xi}}$ under the influence of a positive shearing stress τ.
Source: figure adapted from Nix (2010).

the final position of the head. Due to the parallelogram rule, every Burgers vector associated to a perfect dislocation can be dissociated into two Burgers vectors of the partials, one starting at the first Roman letter of the perfect Burgers vector and ending on the Greek letter centered at the triangular surface, and the other starting from the Greek letter centered at the triangular surface and ending at the second Roman letter of the perfect Burgers vector, so that for example AB on the δ plane splits into $A\delta$ and δB. The Burgers vectors of all perfect and partial dislocations of the FCC structure are listed in table 2.1. Based on the presented notation of the Thompson tetrahedron, the following section deduces the intrinsic stacking-fault arrangement of several extended dislocations for different stress conditions.

2.2.3 Dislocation partials under stress

Section 2.1.3 described the direction in which dislocations would move under the influence of stress. The standard glide loop was assumed to expand by applying a positive shearing stress on one specific side of the glide plane. This section unambiguously defines the positive side of the glide plane using the Thompson tetrahedron. According to the observations of Hirth and Lothe (1982), atoms inside the Thompson tetrahedron slide under the influence of a shearing stress with respect to the atoms outside of the Thompson tetrahedron along the Burgers vector direction, which implies that the positive side of the glide plane where the stress acts is located inside the Thompson tetrahedron. For that reason, the normal vector pointing inwards the Thompson tetrahedron is called the positive normal vector of

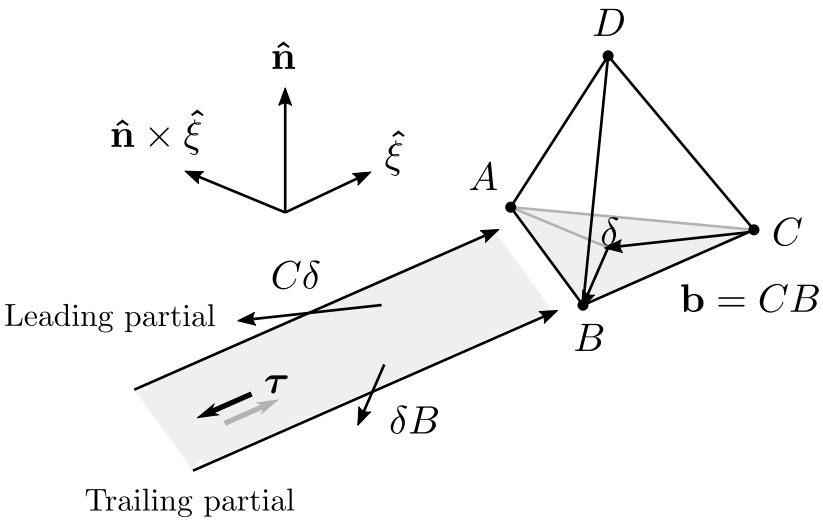

Figure 2.14: Extended LHS dislocation moving towards $\hat{\boldsymbol{n}} \times \hat{\boldsymbol{\xi}}$ under the influence of a positive shearing stress τ.
Source: figure adapted from Nix (2010).

the glide plane, and analogously, the normal vector pointing outwards the Thompson tetrahedron is called the negative normal vector of the glide plane. Based on the convention proposed by Hirth and Lothe (1982), a shearing stress is defined to be positive when the force acting along the Burgers vector is resolved on the glide plane with its normal pointing inwards to the Thompson tetrahedron. By applying the standard glide loop depicted in figure 2.7 to each Shockley partial, the direction in which an extended dislocation moves can also be determined. Figure 2.13 shows a dissociated RHS aligned along the BC direction on the δ plane. When a positive shearing stress is applied on the ABC plane in the direction of BC, the dissociated dislocation would move a full Burgers vector in two steps, namely from B to δ, and then from δ to C. For that reason, the leading partial at the movement front would have the Burgers vector $B\delta$ whereas the trailing partial following behind would carry the Burgers vector δC. Both partials are 60° mixed dislocations with a screw and an edge component. Since the stress acts along the direction of BC parallel to the line vector, the stress affects only the screw component of the partials, which can be considered as two pure RHS dislocations. By laying the right hand aligned with the line direction on the positive side of the glide plane, the thumb points in the direction of motion, towards the A vertex. Since the leading partial is located at the front respect to the direction of motion and the trailing partial follows from behind, the Burgers vectors of the partials point away from each other as shown in figure 2.13.

The same reasoning can be applied to other dislocation types. Consider the dissociated LHS subjected to a positive shearing stress as shown in figure 2.14. By

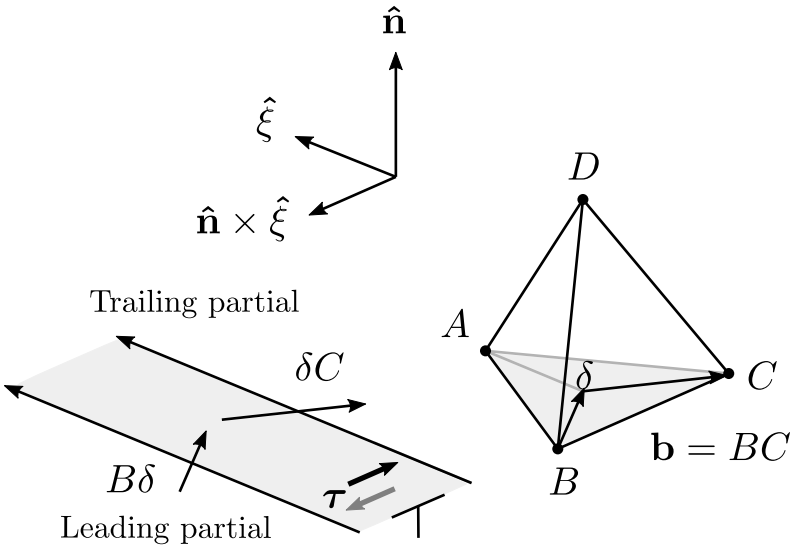

Figure 2.15: Extended negative edge moving towards $\hat{\boldsymbol{n}} \times \hat{\boldsymbol{\xi}}$ under the influence of a positive shearing stress τ.
Source: figure adapted from Nix (2010).

laying the left hand aligned with the line direction on the positive side of the glide plane, the thumb points towards the direction of motion, away from the A vertex. Due to the positive shearing stress applied on the ABC plane in the direction of CB, the dissociated dislocation would move a full Burgers vector in two steps, namely from C to δ, and then from δ to B. For that reason, the leading partial at the movement front would have Burgers vector δC whereas the trailing partial following behind would carry the Burgers vector δB. Since the leading partial is located at the front respect to the direction of motion and the trailing partial follows from behind, the Burgers vectors of the partials point away from each other as shown in figure 2.14. Consider the negative edge dislocation subjected to a positive shearing stress as shown in figure 2.15. According to the right-hand rule, the extra half-plane point towards the $\hat{\boldsymbol{\xi}} \times \hat{\boldsymbol{b}}$, which is located outside of the Thompson tetrahedron. Since the shearing stress is applied inside of the Thompson tetrahedron, it is confirmed that the edge dislocation is negative. Due to the positive shearing stress applied on the ABC plane in the direction of BC, the dissociated dislocation would move a full Burgers vector in two steps, namely from B to δ, and then from δ to C. For that reason, the leading partial at the movement front would have Burgers vector $B\delta$ whereas the trailing partial following behind would carry the Burgers vector δC. The resulting direction of motion is parallel to CB because negative edge dislocations move in the opposite direction of applied stress. As a final comment, notice that all the dislocation types move in the direction of $\hat{\boldsymbol{n}} \times \hat{\boldsymbol{\xi}}$ under the influence of a positive shearing stress.

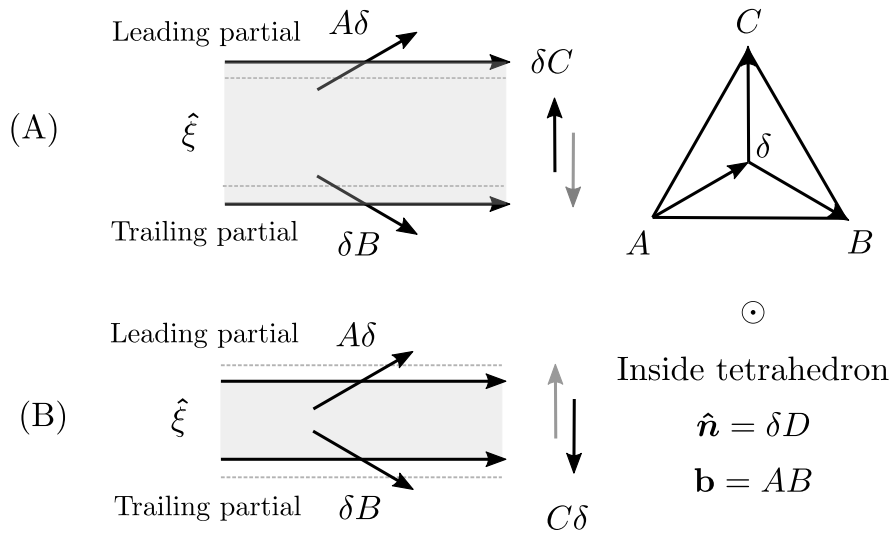

Figure 2.16: View from inside the Thompson tetrahedron of an extended RHS dislocation with Burgers vector AB under a shearing stress along: (A) δC vs (B) $C\delta$ affecting only the equilibrium separation. The gray segmented line represents the unstressed dissociation width and the $\odot$ symbol indicates that the plane normal $\hat{\boldsymbol{n}}$ points out of the page.

It is well know that the Shockley partials repel each other by an elastic force inversely proportional to their separation. On the other hand, the intrinsic stacking-fault decreases the elastic energy density of the dislocation, which leads to an attractive force between the partials. As an analogy to the surface tension of liquids, an intrinsic stacking-fault holds both partials together. The balance of attractive and repulsive forces leads to an equilibrium separation between the partials. It is clear that shearing stresses do not affect the equilibrium separation of an extended dislocation because shearing stresses exert the same gliding force on both partials. A careful observation of the Thompson tetrahedron shown in figure 2.12 demonstrates that the screw components of an extended dislocations are identical, whereas the edge components of Shockley partials have opposite sign. A force applied in the perpendicular direction to the line vector would affect the only edge components of the partials. Since each edge component have opposite signs, said force would drive each Shockley partial in opposite directions. The stresses affecting only the edge components would therefore change the equilibrium separation between the partials. According to the present terminology, a widening stress increases the equilibrium separation between the partials, whereas a compressive stress decreases it. In contrast, positive shearing stresses exerting an identical force on both partials are known as gliding stresses, which do not affect the equilibrium separation.

Figure 2.16 shows a dissociated RHS dislocation of Burgers vector AB laying

on the positive side of the δ plane. Using an hypothetical positive shearing stress, the intrinsic stacking-fault arrangement can be found. Under a positive shearing stress in the direction of AB, the dissociated dislocation would move a full Burgers vector in two steps, namely from A to δ, and then from δ to B. The leading partial would thus have Burgers vector $A\delta$, whereas the trailing partial following behind would have Burgers vector δB. By laying the right hand aligned with the line direction on the positive side of the glide plane, the thumb points in the direction of motion, namely towards the C vertex. Figure 2.16 (A) shows the effect of a shearing stress along δC on the equilibrium separation. An application of the $\hat{\boldsymbol{\xi}} \times \hat{\boldsymbol{b}}$ rule proofs that the extra-half plane of the edge component corresponding to the leading partial is contained inside the Thompson tetrahedron, whereas the extra-half plane of the edge component corresponding to the trailing partial is contained outside the Thompson tetrahedron. Since the shearing stress is applied on the positive side of the glide plane, the edge component of the leading partial is positive, whereas the edge component of the trailing partial is negative. As discussed in section 2.1.3, a positive edge moves in the shearing direction, whereas a negative edge moves against it. As a consequence, the equilibrium separation between the partials increases under the influence of shearing stress along the δC direction. Figure 2.16 (B) shows the effect shearing stress along $C\delta$ on the equilibrium separation for completion. Since the positive edge moves in the shearing direction and the negative edge moves against it, the equilibrium separation decreases under the influence of a shearing stress in the direction of $C\delta$.

The same procedure can be applied to a dissociated dislocation located outside the Thompson tetrahedron to understand the effect of shearing stress on the equilibrium separation. A dissociated RHS dislocation of Burgers vector AB laying on the negative side of the δ plane is shown in figure 2.17. Using an hypothetical positive shearing stress to determine the intrinsic stacking-fault arrangement, it is found that the leading partial at the front would have Burgers vector $A\delta$, whereas the trailing partial following behind would have Burgers vector δB. Applying the right hand on the positive side of the glide plane, the direction of motion would be along $C\delta$, the exact opposite direction of the RHS dislocation located inside the Thompson tetrahedron. It can be concluded that the partials point towards each other when viewing the intrinsic stacking-fault from outside the Thompson tetrahedron. Figure 2.17 (A) shows the effect shearing stress along δC on the equilibrium separation. Using the $\hat{\boldsymbol{\xi}} \times \hat{\boldsymbol{b}}$ rule it can be shown that the edge component of the leading partial is positive, whereas the edge component of the trailing partial is negative. It follows that the equilibrium separation between the partials decreases under the influence of shearing stress along the δC direction. Figure 2.17 (B) shows the effect shearing stress along $C\delta$ on the equilibrium separation for completion. Since the positive edge

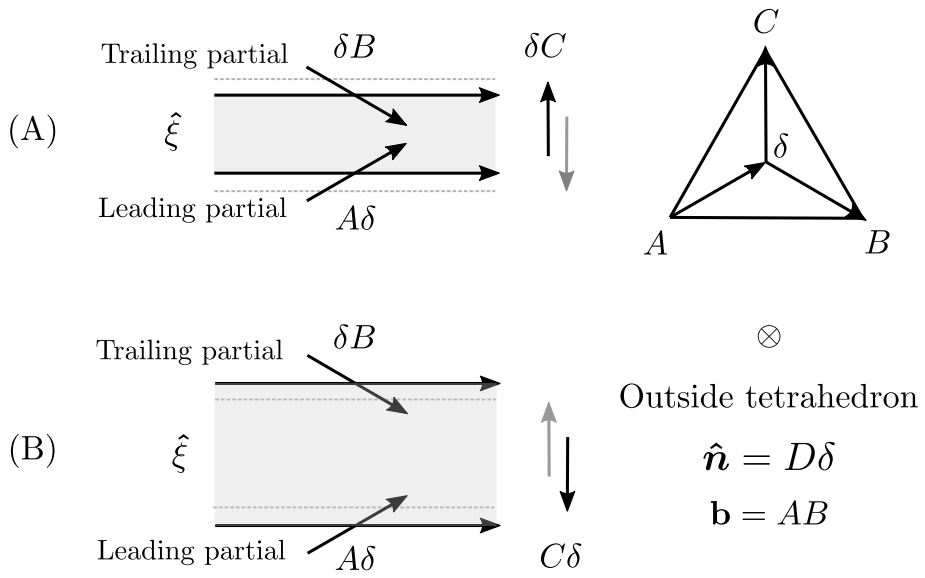

Figure 2.17: View from outside the Thompson tetrahedron of an extended RHS dislocation with Burgers vector AB under a shearing stress along: (A) δC vs (B) $C\delta$ affecting only the equilibrium separation. The gray segmented line represents the unstressed dissociation width and the $\otimes$ symbol indicates that the plane normal $\hat{\boldsymbol{n}}$ points into the page.

moves in the shearing direction and the negative edge moves against it, the equilibrium separation increases under the influence of a shearing stress in the direction of $C\delta$.

Notice that the partials point away from each other when viewing the intrinsic stacking-fault arrangement inside the Thompson tetrahedron, whereas they point towards each other when viewing it outside the Thompson tetrahedron. This is a generic feature of the extended dislocation in FCC crystals. Said observation is succinctly summarized in the Axiom of Anderson et al. (2017):

> *Viewing the perfect dislocation from inside the tetrahedron and along the positive sense of the line, the intrinsic stacking-fault arrangement is achieved by placing the Roman-Greek partial on the viewer's left and the Greek-Roman on the right; viewed in the positive sense from outside the tetrahedron, the intrinsic arrangement is achieved by placing the Greek-Roman partial on the left and the Roman-Greek partial on the right.*

In the next section, an explicit formula for the widening, compressive and gliding stresses will be deduced for materials subjected to uniaxial stress.

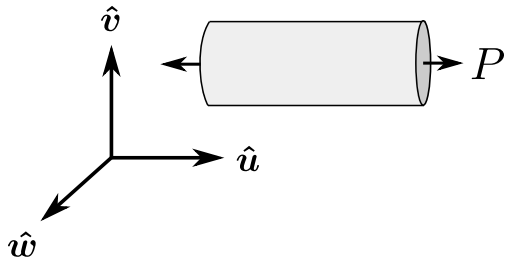

Figure 2.18: Material undergoing tensile stress of magnitude P along the $\hat{\boldsymbol{u}}$ direction.

2.3 Stress components under uniaxial loading

Materials subjected to an uniaxial stress are loaded along a single principal direction. There are two types of uniaxial stress, namely tensile and compressive stresses. The equal stretching forces acting on each side of the material due to a tensile stress provoke an increase of length along the principal direction, whereas the compressive forces pushing the material equally towards its center due to a compressive stress provoke a decrease of length along the principal direction. By convention, a positive value of P represents a tensile stress, whereas a negative value of P refers to a compressive stress (see figure 2.18). The state of loading can be expressed as a diagonal matrix by using the principal directions as an orthonormal basis. In that case, the stress state associated to an uniaxial loading would posses a single non-zero eigenvalue P corresponding to the principal direction $\hat{\boldsymbol{u}}$:

$$\tilde{\boldsymbol{\sigma}} = \begin{pmatrix} P & 0 & 0 \\ 0 & 0 & 0 \\ 0 & 0 & 0 \end{pmatrix} \tag{2.16}$$

Figure 2.19 illustrates that the orthonormal eigenbasis is a rotation of the original coordinate system. Therefore, each element of the orthonormal eigenbasis can be expressed in terms of the original coordinate system:

$$u_x\hat{\boldsymbol{x}} + u_y\hat{\boldsymbol{y}} + u_z\hat{\boldsymbol{z}} = (\hat{\boldsymbol{u}}\cdot\hat{\boldsymbol{x}})\hat{\boldsymbol{x}} + (\hat{\boldsymbol{u}}\cdot\hat{\boldsymbol{y}})\hat{\boldsymbol{y}} + (\hat{\boldsymbol{u}}\cdot\hat{\boldsymbol{z}})\hat{\boldsymbol{z}} \tag{2.17a}$$

$$v_x\hat{\boldsymbol{x}} + v_y\hat{\boldsymbol{y}} + v_z\hat{\boldsymbol{z}} = (\hat{\boldsymbol{v}}\cdot\hat{\boldsymbol{x}})\hat{\boldsymbol{x}} + (\hat{\boldsymbol{v}}\cdot\hat{\boldsymbol{y}})\hat{\boldsymbol{y}} + (\hat{\boldsymbol{v}}\cdot\hat{\boldsymbol{z}})\hat{\boldsymbol{z}} \tag{2.17b}$$

$$w_x\hat{\boldsymbol{x}} + w_y\hat{\boldsymbol{y}} + w_z\hat{\boldsymbol{z}} = (\hat{\boldsymbol{w}}\cdot\hat{\boldsymbol{x}})\hat{\boldsymbol{x}} + (\hat{\boldsymbol{w}}\cdot\hat{\boldsymbol{y}})\hat{\boldsymbol{y}} + (\hat{\boldsymbol{w}}\cdot\hat{\boldsymbol{z}})\hat{\boldsymbol{z}} \tag{2.17c}$$

The following direction cosine matrix transforms the orthonormal eigenbasis back to the original coordinate system:

$$\boldsymbol{U} = \begin{pmatrix} u_x & u_y & u_z \\ v_x & v_y & v_z \\ w_x & w_y & w_z \end{pmatrix} \tag{2.18}$$

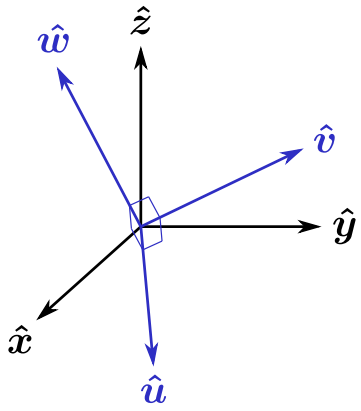

Figure 2.19: Orthonormal eigenbasis in blue can be expressed as a rotation of the reference coordinate system in black.

Using a rotation transformation on the diagonalized matrix given by equation 2.16, the stress state due to an uniaxial loading can be obtained in terms of the original coordinate system:

$$\boldsymbol{\sigma} = \boldsymbol{U}^T \cdot \tilde{\boldsymbol{\sigma}} \cdot \boldsymbol{U} \tag{2.19a}$$

$$= P \begin{pmatrix} u_x & v_x & w_x \\ u_y & v_y & w_y \\ u_z & v_z & w_z \end{pmatrix} \begin{pmatrix} 1 & 0 & 0 \\ 0 & 0 & 0 \\ 0 & 0 & 0 \end{pmatrix} \begin{pmatrix} u_x & u_y & u_z \\ v_x & v_y & v_z \\ w_x & w_y & w_z \end{pmatrix} \tag{2.19b}$$

$$= P \begin{pmatrix} u_x & v_x & w_x \\ u_y & v_y & w_y \\ u_z & v_z & w_z \end{pmatrix} \begin{pmatrix} u_x & u_y & u_z \\ 0 & 0 & 0 \\ 0 & 0 & 0 \end{pmatrix} \tag{2.19c}$$

$$= P \begin{pmatrix} u_x^2 & u_x u_y & u_x u_z \\ u_y u_x & u_y^2 & u_y u_z \\ u_z u_x & u_z u_y & u_z^2 \end{pmatrix} \tag{2.19d}$$

Consider the following unitary normal to the plane expressed in terms of the original coordinate system:

$$n_x \hat{\boldsymbol{x}} + n_y \hat{\boldsymbol{y}} + n_z \hat{\boldsymbol{z}} = (\hat{\boldsymbol{n}} \cdot \hat{\boldsymbol{x}})\hat{\boldsymbol{x}} + (\hat{\boldsymbol{n}} \cdot \hat{\boldsymbol{y}})\hat{\boldsymbol{y}} + (\hat{\boldsymbol{n}} \cdot \hat{\boldsymbol{z}})\hat{\boldsymbol{z}} \tag{2.20}$$

By definition, the stress vector $\boldsymbol{T}$ acting on said plane is given by:

$$\boldsymbol{T} = \boldsymbol{\sigma} \cdot \hat{\boldsymbol{n}} \tag{2.21a}$$

$$= P \begin{pmatrix} u_x^2 & u_x u_y & u_x u_z \\ u_y u_x & u_y^2 & u_y u_z \\ u_z u_x & u_z u_y & u_z^2 \end{pmatrix} \begin{pmatrix} n_x \\ n_y \\ n_z \end{pmatrix} \tag{2.21b}$$

$$= P \begin{pmatrix} n_x u_x^2 + n_y u_x u_y + n_z u_x u_z \\ n_x u_y u_x + n_y u_y^2 + n_z u_y u_z \\ n_x u_z u_x + n_y u_z u_y + n_z u_z^2 \end{pmatrix} \tag{2.21c}$$

$$= P \left(n_x u_x + n_y u_y + n_z u_z \right) \begin{pmatrix} u_x \\ u_y \\ u_z \end{pmatrix} \tag{2.21d}$$

$$= P(\hat{\boldsymbol{u}} \cdot \hat{\boldsymbol{n}})\hat{\boldsymbol{u}} \tag{2.21e}$$

Equation 2.21e shows that the stress vector is proportional to the loading direction. Recall that the goal is to obtain an expression for the widening, compressive and gliding stresses for materials subjected to uniaxial loading. In section 2.2.3 a gliding stress inducing pure dislocation motion was defined as the component of stress parallel to the Burgers vector of the perfect dislocation. A shearing stress applied perpendicular to the Burgers vector could increase or decrease the equilibrium separation depending on the chosen unitary normal to the glide plane. When considering the glide plane with unitary normal pointing inwards to the Thompson tetrahedron, a shearing stress parallel to the Greek-Roman partial perpendicular to the perfect Burgers vector would increase the equilibrium separation between the partials, whereas a shearing stress parallel to the Roman-Greek partial perpendicular to the perfect Burgers vector would decrease the equilibrium separation between the partials. It is therefore necessary to express the unitary loading direction in terms of the normalized Burgers vector of the perfect dislocation $\hat{\boldsymbol{b}}$, the Greek-Roman partial perpendicular to the perfect Burgers vector $\hat{\boldsymbol{p}}$ and the normal pointing inwards to the Thompson tetrahedron $\hat{\boldsymbol{n}}$ to obtain the stress components:

$$\hat{\boldsymbol{u}} = (\hat{\boldsymbol{u}} \cdot \hat{\boldsymbol{b}})\hat{\boldsymbol{b}} + (\hat{\boldsymbol{u}} \cdot \hat{\boldsymbol{p}})\hat{\boldsymbol{p}} + (\hat{\boldsymbol{u}} \cdot \hat{\boldsymbol{n}})\hat{\boldsymbol{n}} \tag{2.22}$$

Substituting equation 2.22 into 2.21e gives:

$$\boldsymbol{T} = P(\hat{\boldsymbol{u}} \cdot \hat{\boldsymbol{n}})(\hat{\boldsymbol{u}} \cdot \hat{\boldsymbol{b}})\hat{\boldsymbol{b}} + P(\hat{\boldsymbol{u}} \cdot \hat{\boldsymbol{n}})(\hat{\boldsymbol{u}} \cdot \hat{\boldsymbol{p}})\hat{\boldsymbol{p}} + P(\hat{\boldsymbol{u}} \cdot \hat{\boldsymbol{n}})^2\hat{\boldsymbol{n}} \tag{2.23}$$

Therefore, the stress components are given by:

$$\boldsymbol{T} \cdot \hat{\boldsymbol{b}} = P(\hat{\boldsymbol{u}} \cdot \hat{\boldsymbol{n}})(\hat{\boldsymbol{u}} \cdot \hat{\boldsymbol{b}}) \tag{2.24a}$$

$$\boldsymbol{T} \cdot \hat{\boldsymbol{p}} = P(\hat{\boldsymbol{u}} \cdot \hat{\boldsymbol{n}})(\hat{\boldsymbol{u}} \cdot \hat{\boldsymbol{p}}) \tag{2.24b}$$

$$\boldsymbol{T} \cdot \hat{\boldsymbol{n}} = P(\hat{\boldsymbol{u}} \cdot \hat{\boldsymbol{n}})^2 \tag{2.24c}$$

The gliding stress given by equation 2.24a is the well-known Schmid law used to calculate the resolved shear stress on a glide system. As discussed in section 2.1.3, dislocations move according to the standard glide loop when the applied stress is parallel to the Burgers vector, which implies that if the value of equation 2.24a is positive, dislocations would move according to the standard glide loop, whereas if it is negative, dislocations would move in the exact opposite direction. With regards to the shear component affecting the equilibrium separation between the partials, if the value of equation 2.24b is positive, then its value represents the widening stress, if the value of equation 2.24b is negative, then its value represents the compressing stress. Finally, equation 2.24c gives the normal stress acting perpendicularly to the gliding plane. If the value of equation 2.24c is positive, then the shearing stress pulls the dislocation away from the plane, whereas if it is negative, then the shearing stress pushes the gliding dislocation against the plane.

The present section has provided simple relations to find all relevant stress components and gliding forces acting on dislocations, which are employed on the next chapter to describe the influence of stress on the cross-slip process of screw dislocations.

Chapter 3

The activation enthalpy of cross-slip

Cross-slip is a thermally-activated process by which screw dislocations change their glide plane, allowing them to overcome obstacles and populate other slip planes (Anderson et al., 2017). It plays an important role in two competing processes during plastic deformation (Jackson, 1983). On the one hand, it causes dynamic recovery during stage III by dislocation annihilation (Hirsch, 2009), and other, it contributes to work hardening by dislocation multiplication (Jackson, 1985; Sudmanns et al., 2019).

Since cross-slip is a thermally activated process, its rate is controlled by an Arrhenius-like equation. Many DDD simulations have successfully model plastic deformation in crystals (Zbib et al., 1998; Weygand et al., 2002; Verdier et al., 1998; Déprés et al., 2006; Chaussidon et al., 2008). Most of them use the rate equation proposed by Kubin et al. (1992). In their model, the cross-slip probability explicitly depends on the resolved shear stress at the onset of stage-III plastic deformation, which is a macroscopic parameter obtained from the stress-strain curve of the material. This probability law has demonstrated to be robust enough to allow the formation of persistent slip bands in the low-cycle fatigue regime (Déprés et al., 2004a), or to study the recovery dynamics in copper (Devincre et al., 2005). However, it is not sufficient in many situations. As an example, in the case of irradiated materials, the local level of stress is very high because of the large number of obstacles associated with the defect density. In this case, the cross-slip events are too frequent (Nogaret et al., 2008). Contrarily, when the stress level is very low, the probability of inducing cross-slip events will be very low or nonexistent.

Based on the work of Kubin et al. (1992), Hussein et al. (2015) recently proposed a more physical rate equation that depends only on microstructure parameters, e.g. the energy barrier required to form a constriction point on a screw dislocation, the Debye frequency of the material, the activation volume and the local stress. This allowed them to implement cross-slip in DDD simulations considering the different mechanisms identified from molecular dynamics (MD) simulations. Quantifying the

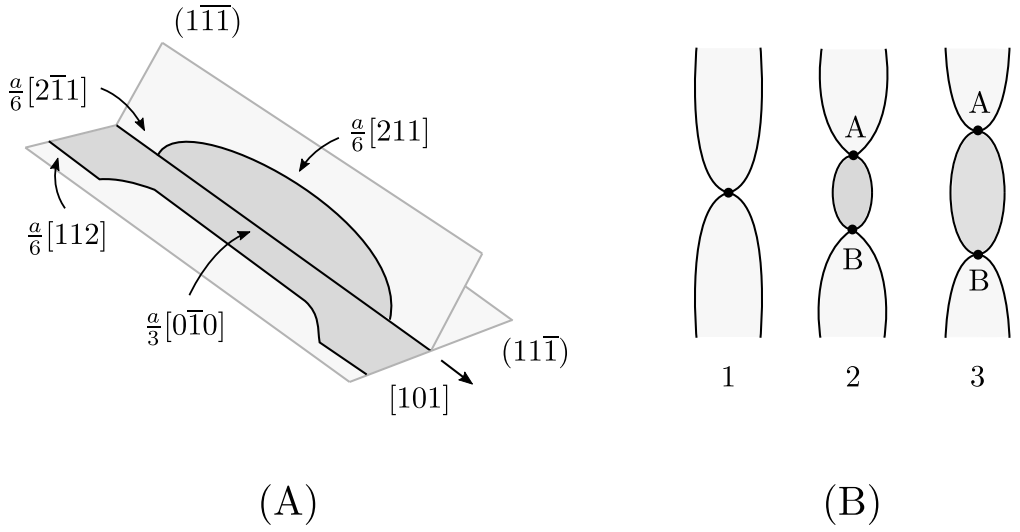

Figure 3.1: Cross-slip models of: (A) Fleischer. The leading partial $\frac{a}{6}[2\bar{1}1]$ can dissociate into $\frac{a}{6}[211]$, which is contained on the cross-slip plane $(1\bar{1}\bar{1})$, and a sessile partial $\frac{a}{3}[0\bar{1}0]$, which is contained at the plane intersection. The remaining trailing partial $\frac{a}{6}[112]$ would be attracted to the sessile dislocation $\frac{a}{3}[0\bar{1}0]$. The resulting partial $\frac{a}{6}[1\bar{1}2]$ is contained on the deviate plane, which completes the cross-slip process; (B) Friedel-Escaig. An initial constriction separates into two semi-constrictions A and B on the deviate plane. Their separation increases until the cross-slip process is completed.
Sources: figures adapted from Fleischer (1959) and Friedel (1964).

effect of stress on the activation barrier is thus of great importance to generate realistic DDD simulations.

The two most plausible cross-slip models for FCC crystals are the Fleischer (FL) and Friedel-Escaig (FE) mechanisms. The FL model was developed by Fleischer (1959). In his model, the leading partial in a stacking-fault dissociates into two partials; one glides on the cross-slip plane and the other remains sessile at the intersection of the two planes (stair-rod dislocation). The trailing partial then reacts with the stair-rod dislocation to form another Shockley partial in the conjugate plane, which completes the cross-slip process (see figure 3.1 (A)). The FE model was developed by Escaig (1968) based on J. Friedel's ideas Friedel (1964). Moreover, he used the line tension (LT) model of cross-slip developed by Stroh (1954) to study the effect of the widening stress (Escaig stress) on the energy barrier. In the FE model, the extended dislocation stops moving in the glide plane due to an obstacle. An already-existing constriction then splits into two halves and then separate in the cross-slip plane. This process proceeds spontaneously due to the stress on the cross-slip plane until the dissociation is completed (see figure 3.1 (B)).

Although there have been some controversy on which cross-slip model prevails (Püschl, 2002), recent atomistic simulations confirm that both FL and FE mechanisms can occur. The determination of which process would dominate depends on many factors. Jin et al. (2011) used the nudged-elastic-band method to study FCC aluminum. They concluded that there is a critical dislocation length below which the screw dislocation cross-slips only via FL mechanism, whereas longer ones would cross-slip either via FL or FE mechanisms, depending on the initial and final positions of the dislocation. The critical length they found was of the order of $22b \approx 5.6$ nm, where b is the magnitude of the Burgers vector. Xu et al. (2017) reported similar findings in FCC nickel using dynamic concurrent atomistic-continuum and MD simulations. They found that screw dislocations of length 6.47 nm cross-slip via FL mechanism, whereas longer dislocations (of length 12.94 nm) can cross-slip via either the FE or FL mechanisms. They also suggested that the critical shear stress for both FE and FL mechanisms depends on the dislocation length. Recently, Kuykendall et al. (2020) used atomistic simulations to examine the effect of stress on the energy barrier of cross-slip via FE and FL mechanisms in FCC nickel. They concluded that the FE mechanism prevails when the Escaig stress on the glide plane is dominant, and that increasing the Schmid and Escaig stress on the cross-slip plane promotes the FL mechanism.

The material of study in this work is FCC copper due to its broad literature. The mechanism of cross-slip in copper has been fully examined using atomistic simulations and it was reported that dislocations in this material cross-slip via FE mechanism (Rasmussen et al., 1997b; Vegge et al., 2001). The activation energy of copper has been calculated using both elasticity theory and atomistic simulations. However, the vast majority of energy barrier calculations employed atomistic simulations (Rao et al., 1999, 2009, 2011, 2015; Vegge et al., 2001; Rasmussen et al., 1997a). Alternatively, Ramírez et al. (2012) used a network-based formulation of dislocation dynamics to study the effect of a general stress on the energy barrier of cross-slip via FE mechanism. They found that the stress-free activation energy in copper is 1.9 eV when the core is represented by two partials, and that it converges to 1.43 eV when the core is distributed among 20 Volterra partial fractional dislocations, the later value being in better agreement with the experimental results. They also found that the cross-slip energy reduces to 0.62 eV in presence of a Lomer-Cottrel junction. The DDD simulations of fatigue mostly rely on the energy barrier, which is often calculated using atomistic simulations. However, the interatomic potential quantitatively affects the simulation results (Rao et al., 1999). Hence, they may not be reliable. On the other hand, in DDD simulations, the core-width used to compute the elastic energy can be determined using the theory developed by Schöck (2010), as suggested by Ramírez et al. (2012). Moreover, DDD simulations naturally enable

the possibility to study the effect of complex structures on the energy barrier. In this way, they offer an attractive alternative to large-scale atomic simulations.

In recent years, Kang et al. (2014) extended Escaig's LT model to include the effect of gliding stress (Schmid stress) on the cross-slip plane. Contrary to Escaig's claim that the Schmid stress had a negligible effect on the energy barrier, they found that it had a comparable effect to the Escaig stress. They calculated the energy barrier in FCC nickel using atomistic methods at different stress conditions and found good qualitative agreement with their LT model. More recently, Malka-Markovitz and Mordehai (2019) solved Strohs's LT model of cross-slip (Stroh, 1954) exactly by linearizing the interaction force between the partials. They obtained a general expression for the activation enthalpy as function of the elastic constants and local stress.

The contribution of this work is twofold. First, the effect of stress on the cross-slip activation enthalpy is carefully calculated using DDD simulations, which is an interesting alternative to the common atomistic approach found in the literature. Second, the results are compared with those obtained from two recent LT models of cross-slip in order to verify their consistency. The objective is to determine whether the aforementioned LT models could be reliably used in DDD simulations to calculate the activation enthalpy of screw segments.

The rest of this chapter is organized as follows. Section 3.1 introduces the cross-slip model of Kang et al. (2014) and the general expression for the activation enthalpy proposed by Malka-Markovitz and Mordehai (2019), section 3.2 introduces the DDD methodology and the simulation setup, subsequently section 3.3 describes the effect of stress on the activation enthalpy obtained using DDD simulations compared with the two LT models and section 3.4 presents the summary and conclusions of this work.

3.1 Theory

3.1.1 Cross-slip model of Kang

The LT model of Kang et al. (2014) assumes the FE mechanism. Thus, the dislocation does not move before cross-slipping i.e. the Schmid stress on the glide plane is zero ($\sigma_S^g = 0$). However, the Escaig stress on the glide plane σ_E^g is not necessarily zero. The equilibrium separation between the partials in the glide plane l^g depends on σ_E^g:

$$l^g = \frac{A}{F^g} \tag{3.1}$$

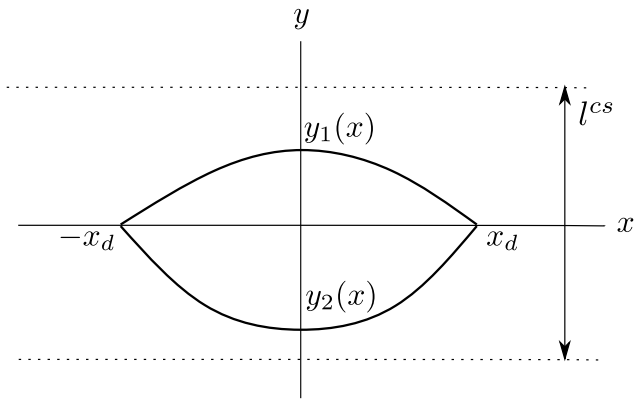

Figure 3.2: The shape of the partials in the cross-slip plane are described by the $y_1(x)$ and $y_2(x)$, and satisfy the boundary conditions $y_1(\pm x_d) = y_2(\pm x_d) = 0$ (figure adapted from Kang et al. (2014)).

where for a screw dislocation dissociated into two 30° partials (Cai et al., 2000):

$$A = \left(\frac{1}{4} - \frac{1}{12(1-\nu)}\right)\frac{\mu b^2}{2\pi} \tag{3.2}$$

$$F^g = \gamma_i - b\sigma_E^g/(2\sqrt{3}) \tag{3.3}$$

The convention used in this framework is that positive σ_E^g increases the distance between the partials and negative decreases it. Analogously, if the dislocation does not move in the cross-slip plane, its equilibrium distance l^{cs} is given by:

$$l^{cs} = \frac{A}{F^{cs}} \tag{3.4}$$

where

$$F^{cs} = \gamma_i - b\sigma_E^{cs}/(2\sqrt{3}) \tag{3.5}$$

The partials surrounding the stacking fault are described by continuous functions $y_1(x)$ and $y_2(x)$ (see figure 3.2). The constriction points are located in the x axis at $\pm x_d$ and thus $y_1(\pm x_d) = y_2(\pm x_d) = 0$ must be satisfied.

The energy contribution from the cross-slipped segment (measured with respect to the energy of an infinite straight screw dislocation resting at equilibrium in the glide plane) is given by (Kang et al., 2014):

$$E^{cs} = W_1 + W_2 + W_3 \tag{3.6}$$

where W_1 is the change in elastic repulsion between the partials, W_2 is the change of the line energy and W_3 the change in SF energy and the work done by the stress. Specifically,

$$W_1 = A \int_{-x_d}^{x_d} \ln\left(\frac{l^g}{y_1 - y_2}\right) dx \tag{3.7}$$

$$W_2 = T \int_{-x_d}^{x_d} \left(\sqrt{1 + (y_1')^2} + \sqrt{1 + (y_2')^2}\right) dx - 4Tx_d \tag{3.8}$$

$$W_3 = \int_{-x_d}^{x_d} (F_1^{cs} y_1 + F_2^{cs} y_2)\, dx - 2F^g l^g x_d \tag{3.9}$$

where

$$F_1^{cs} = F^{cs} - b\sigma_S^{cs}/2 \tag{3.10}$$

$$F_2^{cs} = -F^{cs} - b\sigma_S^{cs}/2 \tag{3.11}$$

The energy functional in equation 3.6 was minimized using the conjugate gradient method as suggested by Kang et al. (2014).

The line energy per unit length was given by (Kang et al., 2014):

$$T = \alpha\mu b^2/2 \tag{3.12}$$

where α is a dimensionless fitting parameter. Formally, the energy barrier is given by:

$$E_b(\sigma_E^g, \sigma_S^{cs}, \sigma_E^{cs}) = \max_{x_d} E(x_d; \sigma_E^g, \sigma_S^{cs}, \sigma_E^{cs}) \tag{3.13}$$

where

$$E = \min_{y_1, y_2} E^{cs}(y_1, y_2; x_d; \sigma_E^g, \sigma_S^{cs}, \sigma_E^{cs}) + E^g(\sigma_E^g) \tag{3.14}$$

E^g being the energy of an isolated constriction on a perfect screw dislocation:

$$E^g = 2l^g\sqrt{AT} \int_0^1 [-\ln t + (t-1)]^{1/2} dt \tag{3.15}$$

The activation energy can be obtained for a given stress condition by solving equation 3.14 numerically.

3.1.2 Cross-slip model of Malka-Markovitz and Mordehai

Another useful formulation of the LT model of cross-slip was proposed by Malka-Markovitz and Mordehai (2019), who solved Strohs's LT model (Stroh, 1954) exactly by linearizing the interaction force between the partials. They obtained the following general expression for the activation enthalpy as function of the elastic constants and local-stress components:

$$\frac{\Delta H(\sigma)}{\Delta E_0} = \frac{\beta^g}{2} + \left(\frac{\beta^{cs}}{2}\right)\tanh(l_c) - \left(\frac{\beta^{cs}}{2}\right)\left[\frac{2\alpha_L}{1.55} l_c E^* + \frac{\alpha_{Ls}^3}{1.55}\frac{\delta}{\beta^{cs}} l_c^3\right] \tag{3.16}$$

where $\Delta E_0 = 1.9$ eV is the energy barrier of copper obtained in this work using DD simulations and $\alpha_L \approx 0.6$ is a scale factor.

β^g and β^{cs} are functions of the Escaig stresses on the glide and cross-slip plane, respectively:

$$\beta^g = \frac{1}{1 + \frac{\sqrt{3}b}{6\gamma_i}\sigma_E^g} \quad \text{and} \quad \beta^{cs} = \frac{1}{1 + \frac{\sqrt{3}b}{6\gamma_i}\sigma_E^{cs}} \tag{3.17}$$

whereas δ is a quadratic function of the Schmid stress on the cross-slip plane:

$$\delta = \frac{1}{6}\left(\frac{b\sigma_S^{cs}}{\gamma_i}\right)^2 \tag{3.18}$$

The E^* function is a dimensionless off-set in the interaction energy between the glide and cross-slip planes (Malka-Markovitz and Mordehai, 2018):

$$E^* = \ln\left(\frac{\beta^{cs}}{\beta^g}\right) \tag{3.19}$$

The critical length l_c in equation 3.16 can be found by solving the following expression numerically (Malka-Markovitz and Mordehai, 2018):

$$\frac{1.55}{\cosh^2(l_c)} - \frac{3\delta}{\beta^{cs}} l_c^2 = 2E^* \tag{3.20}$$

In contrast with the convention used in Kang et al. (2014) LT model of cross-slip, a positive σ_E^g decreases the equilibrium separation between the partials, whereas a negative one increases it.

3.2 Methodology

3.2.1 Dislocation dynamics method

Dislocation dynamics is a modeling approach to study crystal plasticity, in which dislocation lines are discretized in linear segments and their motion is determined

(Sills et al., 2016). A segment is defined by two nodes on its ends and a tangent line $\hat{\boldsymbol{\xi}}$ that connects them. The Burgers vector $\boldsymbol{b}$ associated to it indicates the displacement's magnitude and direction. The following sections briefly explain how discrete dislocations were modeled.

Force computation

The force exerted by the local stress at each node is calculated using the Peach-Köhler formula. Similarly to other DDD codes (Arsenlis et al., 2007), NuMoDis (Drouet et al., 2014) uses the formalism developed by Arsenlis et al. (2007) to compute the nodal forces. This force affects the nodal velocity through a given mobility law. Thus, the dislocation dynamics can be determined by updating the position of all nodes after a simulation step.

In order to study cross-slip in FCC crystals, the dissociated character of dislocations must be considered. As discussed in chapter 2, the stacking-fault (SF) produces a force that tends to attract the partials towards each other, compensating the elastic repulsion between them. This results in an equilibrium separation distance in the SF ribbon. Perfect dislocations dissociate into partials if it decreases its elastic energy. However, DDD codes are based on nodal forces and do not consider the systems energetics to determine its evolution. In consequence, Martínez et al. (2008) proposed to account for the intrinsic SF energy γ_i by introducing a SF force ($\boldsymbol{f}_{sf}$) on the discretization nodes. They derived that $\boldsymbol{f}_{sf}$ should be of magnitude γ_i, and perpendicular to both the tangent line and SF plane $\hat{\boldsymbol{n}}$. The equation satisfying these conditions is given by:

$$\boldsymbol{f}_{sf} = \gamma_i \hat{\boldsymbol{n}} \times \hat{\boldsymbol{\xi}} \tag{3.21}$$

In NuMoDis (Drouet et al., 2014), the SF ribbon is defined by an ordered list of nodes conforming the dislocation partials and the plane that contains them. The SF forces acting on a partial, in order to be physical, must point towards the opposite partial. Thus, given a slip plane orientation, the node order defining the circuit must be such that the SF force given by equation 3.21 satisfy this condition.

Velocity computation

In FCC metals, the relationship between forces and velocities is linear due to the small intrinsic lattice resistance (Bulatov and Cai, 2006). The total force at a node $\boldsymbol{f}$ is given by $\boldsymbol{f} = \boldsymbol{f}_{PK} + \boldsymbol{f}_{sf}$, where $\boldsymbol{f}_{PK}$ is the Peach-Köhler force. The projections of $\boldsymbol{f}_{PK}$ and $\boldsymbol{f}_{sf}$ on the glide plane act perpendicular to the line segment. Therefore, the mobility law is of the form:

$$\boldsymbol{f} = \boldsymbol{B} \cdot \boldsymbol{v} \tag{3.22}$$

where $\boldsymbol{v}$ is the nodal velocity and $\boldsymbol{B}$ the viscosity matrix:

$$\boldsymbol{B}(\hat{\boldsymbol{\xi}}) = B(\boldsymbol{I} - \hat{\boldsymbol{\xi}} \otimes \hat{\boldsymbol{\xi}}) \tag{3.23}$$

where B is the viscosity coefficient.

Thus, the nodal velocity is obtained by inverting the viscosity matrix from equation 3.22:

$$\boldsymbol{v} = \boldsymbol{B}^{-1} \cdot \boldsymbol{f} \tag{3.24}$$

At each simulation step, the force at every node due to the influence of all other segments and SF is computed; the nodal velocities are thus calculated and their new positions are updated.

Elastic energy

Cai et al. (2006) showed that the non-singular interaction energy E^{ns} between a segment with ends $\boldsymbol{x}_1$ and $\boldsymbol{x}_2$ and Burgers vector $\boldsymbol{b}$ with another segment with ends $\boldsymbol{x}_3$ and $\boldsymbol{x}_4$ and Burgers vector $\boldsymbol{b}'$ is given by:

$$\begin{aligned} E^{ns} = &-\frac{\mu}{8\pi} \int_{\boldsymbol{x}_3}^{\boldsymbol{x}_4} \int_{\boldsymbol{x}_1}^{\boldsymbol{x}_2} \partial_k \partial_k R_a b_i b'_j dx_i dx'_j \\ &-\frac{\mu}{4\pi(1-\nu)} \int_{\boldsymbol{x}_3}^{\boldsymbol{x}_4} \int_{\boldsymbol{x}_1}^{\boldsymbol{x}_2} \partial_i \partial_j R_a b_i b'_j dx_k dx'_k \\ &+\frac{\mu}{4\pi(1-\nu)} \int_{\boldsymbol{x}_3}^{\boldsymbol{x}_4} \int_{\boldsymbol{x}_1}^{\boldsymbol{x}_2} \partial_k \partial_k R_a b_i b'_i dx_j dx'_j \\ &-\frac{\mu\nu}{4\pi(1-\nu)} \int_{\boldsymbol{x}_3}^{\boldsymbol{x}_4} \int_{\boldsymbol{x}_1}^{\boldsymbol{x}_2} \partial_k \partial_k R_a b_i b'_j dx_j dx'_i \end{aligned} \tag{3.25}$$

where μ is the shear modulus, ν the Poisson's ratio, $R_a = \sqrt{\boldsymbol{R} \cdot \boldsymbol{R} + a^2}$, $\boldsymbol{R} = \boldsymbol{x} - \boldsymbol{x}'$, and a the core-width parameter.

The analytical expressions resulting from the solution of equation 3.25 for parallel and non-parallel segments were provided by Cai et al. (2006). These formulas were used to calculate the interaction and self-energies of the segments in NuMoDis (Drouet et al., 2014).

The core-width parameter a affects the elastic energy both qualitatively and quantitatively. Schöck (2010) developed a theory based on the Peierls framework (Schoeck, 2005) to obtain a physical value of a. He showed that the total energy of a single straight dislocation is given by (Schöck, 2010):

$$E^P = E_L(\phi)\left[\ln\left(\frac{r}{2\overline{w}(\phi)}\right)+1\right] \tag{3.26}$$

where ϕ is the angle between the Burgers vector and the line direction, r is the outer cut-off radius, $\overline{w}(\phi)$ is the average width of its edge and screw components, and $E_L(\phi)$ is the pre-logarithmic elastic line energy factor:

$$E_L(\phi) = \frac{\mu b^2}{4\pi}\left(\cos^2(\phi)+\frac{\sin^2(\phi)}{1-\nu}\right) \tag{3.27}$$

Schöck (2010) argued that $\overline{w}(\phi)$ can be approximated as the width of a single dislocation in an isotropic medium passing through two equilibrium positions i.e. with SF energy $\gamma = \gamma_u$ (Schöck, 2010):

$$\frac{\overline{w}(\phi)}{b} = \frac{\cos^2(\phi)+\sin^2(\phi)/(1-\nu)}{b/c+2\pi^2\gamma_u/(\mu b)} \tag{3.28}$$

where c is the interplanar glide plane spacing, γ_u the unstable SF energy and b is the magnitude of the Burgers vector.

Using the model of Cai et al. (2006), the line energy for screw E_S and edge dislocation E_E are found to be (Schöck, 2010):

$$E_S = \frac{\mu b^2}{4\pi}\ln\left(\frac{r\sqrt{e}}{a_S}\right) \tag{3.29}$$

$$E_E = \frac{\mu b^2}{4\pi(1-\nu)}\ln\left(\frac{r}{a_E}\right) \tag{3.30}$$

where a_S and a_E are the core spreading parameters of the screw and edge components, respectively, and e is the base of the natural logarithm.

The continuum description in equations 3.29 and 3.30 must be consistent with the Peierl's atomistic treatment in equation 3.26. Imposing this condition, a_S and a_E are required to be (Schöck, 2010):

$$a_S = \frac{2\overline{w}(0)}{\sqrt{e}} \quad \text{and} \quad a_E = \frac{2\overline{w}(\pi/2)}{e} \tag{3.31}$$

Following the work of Ramírez et al. (2012), the core-width parameter can be considered as an averaged value of a_S and a_E:

$$a \approx \frac{2\overline{w}(0)}{e} = \frac{2}{e}\left(\frac{b}{b/c+2\pi^2\gamma_u/(\mu b)}\right) \tag{3.32}$$

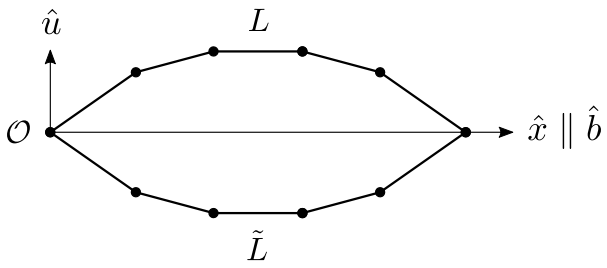

Figure 3.3: The solid dots denote the nodal positions; the shape of the leading and trailing partials are described by L and $\tilde{L}$, respectively.

Effective stacking-fault energy

As discussed in chapter 2, the partial located at the front with respect to the direction of motion is called the leading partial, and the other trailing partial. Let $L = \{\boldsymbol{P}_1, \boldsymbol{P}_2, ..., \boldsymbol{P}_N\}$ and $\tilde{L} = \{\boldsymbol{Q}_1, \boldsymbol{Q}_2, ..., \boldsymbol{Q}_N\}$ represent the set of nodes conforming the leading and trailing partials, respectively (see figure 3.3).

The effective SF energy is given by the SF energy W_{SF} plus the work done by the applied forces W_{app}, which can be calculated as follows:

$$W_{SF} = \gamma_i \sum_{j=1}^{N} \left[\frac{y_{j+1} + y_j}{2} \Delta x_j - \frac{\tilde{y}_{j+1} + \tilde{y}_j}{2} \Delta \tilde{x}_j \right] \tag{3.33}$$

$$W_{app} = \sum_{j=1}^{N} F y_j \Delta x_j + \tilde{F} \tilde{y}_j \Delta \tilde{x}_j \tag{3.34}$$

where:

$$y_j = \boldsymbol{P}_j \cdot \hat{\boldsymbol{u}} \tag{3.35a}$$

$$\tilde{y}_j = \boldsymbol{Q}_j \cdot \hat{\boldsymbol{u}} \tag{3.35b}$$

$$\Delta x_j = (\boldsymbol{P}_{j+1} - \boldsymbol{P}_j) \cdot \hat{\boldsymbol{b}} \tag{3.35c}$$

$$\Delta \tilde{x}_j = (\boldsymbol{Q}_{j+1} - \boldsymbol{Q}_j) \cdot \hat{\boldsymbol{b}} \tag{3.35d}$$

$\hat{\boldsymbol{u}} = \hat{\boldsymbol{n}} \times \hat{\boldsymbol{b}}$ is an unitary vector contained in the slip plane of normal $\hat{\boldsymbol{n}}$ perpendicular to the normalized Burgers vector $\hat{\boldsymbol{b}}$. In absence of Schmid stress, the partials are indistinguishable from each other due to the spatial symmetry with respect to the $\hat{\boldsymbol{x}}$ axis. For that reason, the sign of $\hat{\boldsymbol{u}}$ does not affect the energy. However, the leading and trailing partials are univocally defined in the presence of a Schmid stress. In that case, $\hat{\boldsymbol{u}}$ must point towards the bowing-out direction because the energy barrier does not depend on the sign of the Schmid stress (Kang et al., 2014; Kuykendall et al., 2020; Malka-Markovitz and Mordehai, 2019).

The proportionality factors F and $\tilde{F}$ are given by:

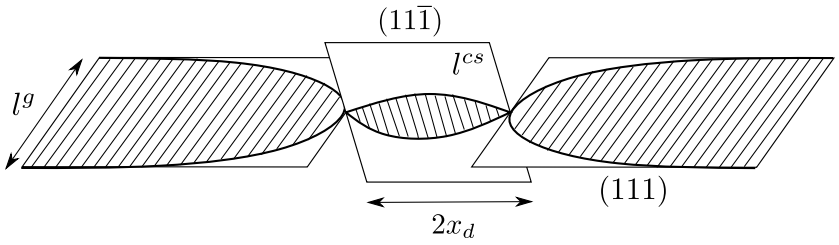

Figure 3.4: An equilibrium configuration during cross-slip via FE mechanism. The process is completed when the constriction separation tends to infinity. In this limit, the dislocation is completely contained in the conjugate plane with separation between the partials l^{cs} for all x (figure adapted from Kang et al. (2014)).

$$F = -\frac{b\sigma_E}{2\sqrt{3}} - \frac{b\sigma_S}{2} \text{ and } \tilde{F} = \frac{b\sigma_E}{2\sqrt{3}} - \frac{b\sigma_S}{2} \tag{3.36}$$

where the subscripts E and S refer to the Escaig and Schmid stress, respectively.

All the nodes were mobile except those two at the extremes, which simulate the constriction points at the equilibrium configurations. Therefore, the partials always satisfied $y_1 = \tilde{y}_1 = y_N = \tilde{y}_N = 0$.

3.2.2 Simulation setup

Cross-slip via FE mechanism was assumed in all simulations. The DDD code NuMoDis was used to find the equilibrium configurations at different cross-slip stages. The total energy of a configuration consisted of its total elastic energy plus the effective stacking-fault energy, which were computed as described in sections 3.2.1 and 3.2.1. The applied stresses were small enough such that the Frank-Read source remained deactivated in all simulations.

According to the FE mechanism, the dislocation must stop moving before cross-slipping. Therefore, the Schmid stress on the glide plane σ_S^g was always assumed to be zero. The dislocation width in the glide plane was affected by the Escaig stress σ_E^g. Soon after stop moving, an already-existing constriction splits into two halves and the dislocation expands in the cross-slip plane until equilibrium is reestablished (see figure 3.4). This occurs in the limit when the distance between the constriction points in the cross-slip plane $2x_d$ tends to infinity. In DDD codes, an infinite dislocation does not really exist. Thus, the initial configuration consisted of a dislocation with length of 1000 Å lying in the $(\overline{1}11)$ plane. This was a long-enough dislocation such that most part of it attained equilibrium i.e the distance l^g between the partials. The dislocation was pinned at its ends. The Burgers vector of the partials pointed away from each other on the glide plane as shown in figure 3.5 (a), whereas

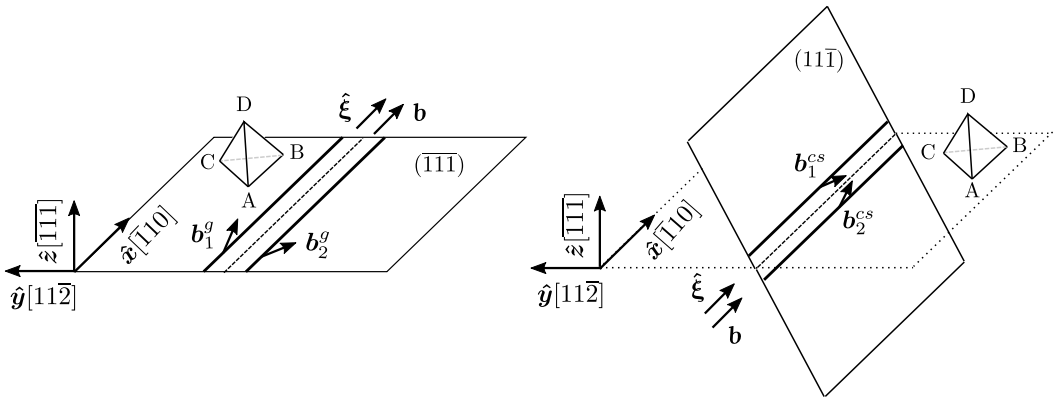

(a) (b)

Figure 3.5: Simulation setup showing: (a) the reference configuration consisting of a dissociated $\boldsymbol{b} = AB$ right-handed screw (RHS) dislocation at equilibrium on the glide plane $(\overline{1}\overline{1}\overline{1})$ with partials' Burgers vector $\boldsymbol{b}_1^g = A\delta = \frac{a_0}{6}[\overline{1}2\overline{1}]$ and $\boldsymbol{b}_2^g = \delta B = \frac{a_0}{6}[\overline{2}11]$ pointing away from each other, and (b) the final configuration consisting of a dissociated RHS dislocation at equilibrium in the cross-slip plane $(11\overline{1})$ with partials' Burgers vector $\boldsymbol{b}_1^{cs} = \gamma B = \frac{a_0}{6}[\overline{1}21]$ and $\boldsymbol{b}_2^{cs} = A\gamma = \frac{a_0}{6}[\overline{2}1\overline{1}]$ pointing towards each other.

the Burgers vector of the partials pointed towards each other on the deviated plane as shown in figure 3.5 (b).

An intermediate cross-slip configuration consisted of a semi-infinite dislocation on the glide plane with a constricted cross-slipped segment on the conjugate plane $(11\overline{1})$ as shown in figure 3.6 (a). The total configuration length was fixed to 1000 Å, in agreement with the initial state (see figure 3.6 (b)). The intermediate cross-slip configuration was thus characterized by the distance between its constriction points. In the limiting case when the constrictions points are infinitely apart, the dislocation must be completely contained in the cross-slip plane. Unlike in the glide plane, the dislocation was allowed to move by bowing-out on the conjugate plane. The sign of the Schmid stress on the cross-slip plane σ_S^{cs} was affected only the bowing-out direction, and not the total energy. As in the glide plane, the width of dislocation in the conjugate plane was affected by the Escaig stress σ_E^{cs}.

3.2.3 Loading setup

In order to study the effect of σ_E^g, σ_S^{cs} and σ_E^{cs}, the coordinate system was rotated such that the $[\overline{1}\overline{1}\overline{1}]$ direction matched with the $\hat{\boldsymbol{z}}$ axis and the Burgers vector $[\overline{1}10]$ with the $\hat{\boldsymbol{x}}$ axis. Thus, the stress on the glide and cross-slip planes as function of the tensor components in the Cartesian coordinate system were given by:

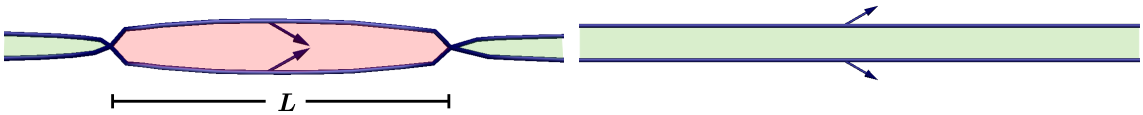

(a) (b)

Figure 3.6: Graphic visualization of: (*a*) an intermediate cross-slip configuration of distance L between its constriction points and (*b*) the reference configuration consisting of a relaxed dislocation completely contained on the glide plane. The area shaded in red represents the deviated plane, whereas the region shaded in green indicates the glide plane.

$$\sigma_S^g = \sigma_{xz} \tag{3.37}$$

$$\sigma_E^g = \sigma_{yz} \tag{3.38}$$

$$\sigma_S^{cs} = \frac{2\sqrt{2}\sigma_{xy} - \sigma_{xz}}{3} \tag{3.39}$$

$$\sigma_E^{cs} = \frac{7\sigma_{zy} + 2\sqrt{2}(\sigma_{yy} - \sigma_{zz})}{9} \tag{3.40}$$

The energy of an intermediate cross-slip configuration was measured with respect to the energy of the initial state i.e. the energy of the dislocation resting at equilibrium in the glide plane under stress σ_E^g. Thus, the energy barrier was defined as the maximum energy among all intermediate cross-slip configurations as function of the distance between the constriction points.

3.3 Results and discussion

3.3.1 Calibration of the cross-slip models

The relative energy of the intermediate cross-slip configurations at zero stress is shown in figure 3.7. The elastic constants of copper used in both the DDD simulations and LT model are shown in table 3.1. The energy uncertainty of the order of ± 0.1 eV in all the simulations results can be attributed to the line discretization used in the DDD simulations, as well as to the finite core-width size of the non-singular theory of dislocations. The parameter α in the LT model of Kang et al. (2014) LT model was calibrated such that the equilibration energy matched with the DDD simulations at zero stress. The value was found to be $\alpha = 0.22$. Together

Property	Value
a_0	3.61 Å (Davey, 1925)
b	$a_0/\sqrt{2}$ (Kittel and McEuen, 2018)
γ_i	42 mJ/m^2 (Bonneville and Escaig, 1979)
γ_u	182 mJ/m^2 (Ramírez et al., 2012)
ν	0.324 (Ledbetter and Naimon, 1974)
μ	54.6 GPa (Schmauder and Mishnaevsky, 2008)
B	1.5 $\times 10^{-5}$ Pa-s (Philibert, 1979)
a	1.95 Å (from equation 3.32)

Table 3.1: Parameters used for FCC copper; a_0 is the lattice parameter, b the magnitude of the Burgers vector, γ_i the intrinsic SF energy, γ_u the unstable SF energy, ν the Poisson's ratio, μ the shear modulus, B the viscosity coefficient at room temperature and a the core-width parameter.

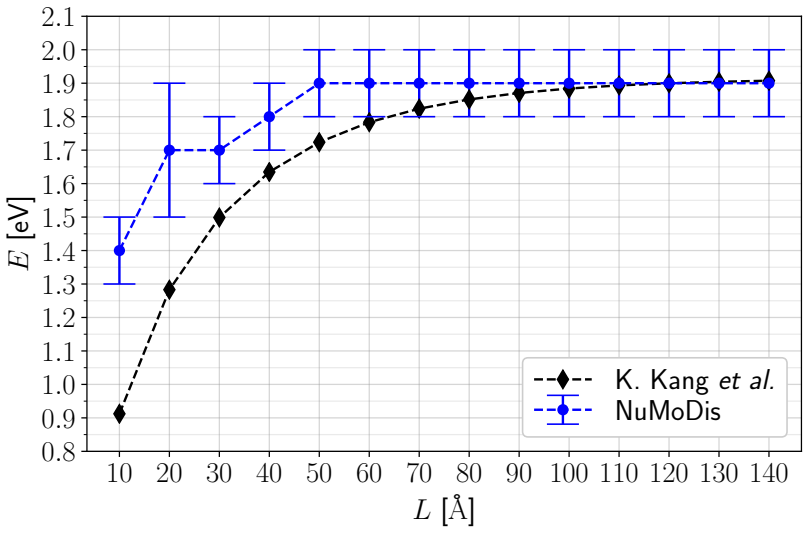

Figure 3.7: The energy barrier as function of the constriction separation at zero stress.

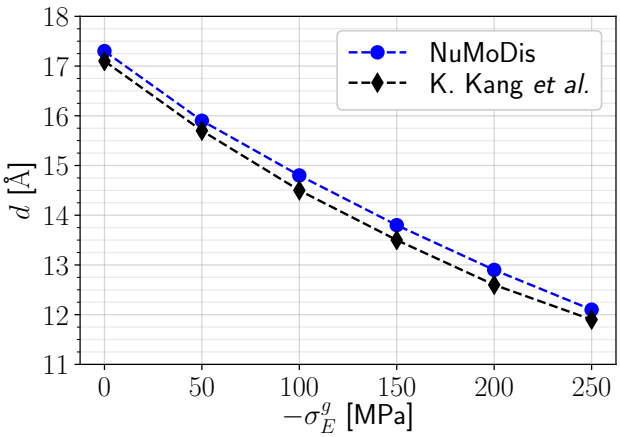

Figure 3.8: The effect of Escaig stress on the equilibrium separation between the partials. The segmented line corresponds to equation 3.1.

with the core-width parameter in the elastic energy, the choice of α was a key parameter for the good agreement between the LT model of Kang et al. (2014) and the DDD simulations. The effect of compressive Escaig stress was to decrease the SF width. The stressed equilibrium separation obtained from the DDD simulations was in great agreement with the LT model, as shown in figure 3.8. The energy predicted by the LT model of Kang et al. (2014) and that obtained with the simulations does not match for short cross-slipped segments as seen in figure 3.7. This is expected because the LT model approximates the energy of a differential segment as that of a straight dislocation (Dupuy and Fivel, 2002). In fact, the LT model breaks down in the limiting case were $2x_d = 0$ because the elastic repulsion diverges (see equation 3.7). However, this is not relevant since the objective of this work is to quantify the stress effect on the energy barrier, which occurs for longer dislocation lines where the LT model is more physical.

In the unstressed case, the energy monotonically augments as the constriction separation increases, but quickly reaches a maximum value of 1.9 eV. This means that once the cross-slip segment reaches a critical length (around 60 Å), no further energy is required to be invested and the cross-slip process continues spontaneously. Therefore, the unstressed energy barrier of copper is equal to 1.9 eV as reported by Ramírez et al. (2012). The equilibration energy encountered in the unstressed cross-slip is roughly equal to twice the energy required to form an isolated constriction. It can be argued that at the beginning of cross-slip, when the two constrictions are close to each other, the elastic repulsion between them adds up to the energy required to form them in isolation. However, as the distance between them increases, their interaction further decreases. Thus, if they are sufficiently far apart, the total energy with respect to the relaxed dislocation is roughly equal to that of the two

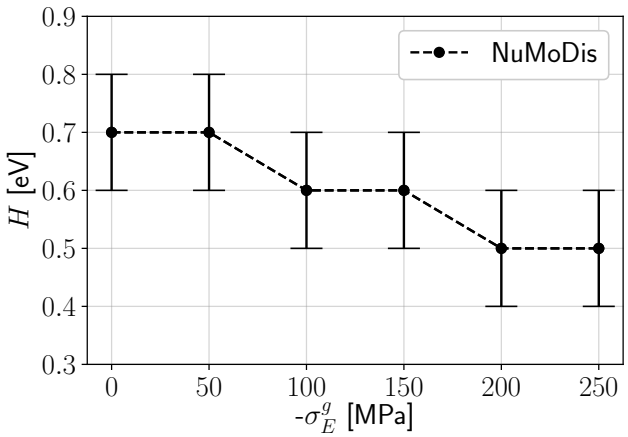

Figure 3.9: The effect of compressive Escaig stress on the constriction energy according to DDD simulations.

independent constrictions.

3.3.2 Effect of stress on the constriction energy

The planar constriction energy at zero stress is 0.7 eV, according to the DDD simulations (see figure 3.9). Stroh (1954) found the energy of a constriction using elasticity theory. Assuming a shear modulus of G = 45 GPa and an equilibration distance between the partials at zero stress of $d_0 = 18$ Å, one finds that in his model the energy of a single constriction is roughly 2 eV, which is almost three times higher than that found in this work (0.7 eV). Püschl (1990) estimated a constriction energy of 1.1 eV for FCC copper using elasticity theory. Later on, Saada (1991) generalized the LT model of Püschl (1990) for arbitrary constricting distance. He obtained different constriction energy values in the range of 0.33 - 0.7 eV, depending on the choice r_0/b, where r_0 is a cut-off radius. Although these values are in better agreement with the experimental energy barrier, the (arbitrary) choice of r_0 was not clearly determined. Rasmussen et al. (1997a) found a constriction energy of 1.6 eV using atomistic simulations, in reasonable agreement with Stroh (1954), but too high according to the experimental energy barrier. More recently, Ramírez et al. (2012) found a constriction energy of 0.7 eV using dislocation dynamics, in excellent agreement with this work.

The effect of pure compressing stress on the constriction energy was found to be negligible. The slight decrease on the constriction energy observed in figure 3.9 is not conclusive. Nevertheless, one can assert that the average constriction energy did not vary much in the given range of stresses. The small effect of stress on the constriction energy can be explained by using the model developed by Püschl (1990).

It predicts a marginal decrease in constriction energy (of less than 0.2 eV) when the splitting width between the partials decreases from $8b \approx 20.4$ Å to $6b \approx 15.3$ Å. These are roughly the equilibration distances simulated by NuMoDis (Drouet et al., 2014) at zero (17.4 Å) and -250 MPa (12.1 Å), respectively. Thus, according to this model, one should not expect the constriction energy to vary much by applying a pure compressing stress for the given range of values.

The asymptotic convergence of the cross-slip energy barrier at zero stress observed in figure 3.7 has been thoroughly reported before. Duesbery et al. (1992) calculated the constriction pair energy as function of the stacking-fault energy using a linear-elastic framework, and found that for constriction separation larger than $\sim 50b$, the total energy becomes that of two independent constrictions. In particular, for FCC copper, they found that the asymptotic value of the cross-slipped configuration was 3.7 eV. They also identified the asymmetric nature of the two constrictions in the cross-slip plane, as they asserted that one had lower energy being screw-like, and the other higher energy being edge-like. These are different from the Stroh-type constriction, which are edge-like on the one side, and screw-like on the other. Later on, Rasmussen et al. (1997a) corroborated several results of Duesbery et al. (1992) using atomistic simulations, as they obtained that indeed the total energy converged to the value of two independent constrictions for separations larger than $\sim 50b$. They measured a screw-like constriction energy of -3.8 eV, and an edge-like constriction energy of 1.1 eV, which added up to the total energy barrier in FCC copper (2.7 eV). Although this value is lower than that obtained by Duesbery et al. (1992), it is roughly the double of the experimental value obtained by Bonneville et al. (1988). Rao et al. (1999) calculated an energy barrier for cross-slip at zero stress in the range of 1.07 - 1.28 eV using molecular statics. This energy is significantly smaller than that predicted by Rasmussen et al. (1997a). They argued that it could be due to the difference in interatomic potentials used, as well as the Green's function technique used to relax the boundary forces in the simulations developed by Rao et al. (1999). Ramírez et al. (2012) found an unstressed energy barrier of 1.9 eV using DDD simulations for dislocations dissociated into two partials. They obtained that the energy plateau was reached for a constriction separation of about 60 Å. Both results are in excellent agreement with the simulations in this work. Furthermore, notice that the critical length is about the half of the value found by previous methods.

3.3.3 Effect of stress on an isolated dislocation

Uncoupled stress case

In order to study the independent influence of the stress components on the energy barrier, three cross-slip possibilities were considered: (A) pure compression on the glide plane, (B) pure expansion on the conjugate plane and (C) pure bowing-out on the conjugate plane. The stress was increased up to 250 MPa, because the equilibrium configuration breaks down around 260 MPa (Davis et al., 2001). The activation enthalpy obtained from DDD simulations, the LT model of Kang et al. (2014) and the general expression for the activation enthalpy proposed by Malka-Markovitz and Mordehai (2019) are in good quantitative agreement with each other, as shown in figure 3.10.

The largest influence on the energy barrier was obtained by pure compression on the glide plane, which reduced it up to 45% (see figure 3.10 (A)). The minimum energy barrier of 1 eV was obtained by applying a compressive Escaig stress of 250 MPa on the glide plane. This is in contrast with the lower energy value of 0.95 eV obtained by Ramírez et al. (2012) under a pure σ_E^{cs} of 220 MPa. On the other hand, Kang et al. (2014) also concluded that the compressive Escaig stress applied on the glide was the most effective way of reducing the energy barrier in FCC nickel. The pure widening Escaig stress on the cross-slip reduced it up to 20% (see figure 3.10 (B)) and the pure Schmid stress on the cross-slip produced a decrease in the energy barrier of about 15% (see figure 3.10 (C)).

The effect of stress was not only to decrease the energy barrier but also the activation length of cross-slip. The maximum of energy at 200 MPa occurred for a constriction separation of about 25 Å. This value is comparable to the activation length of $12b \approx 30.6$ Å at 220 MPa obtained by Ramírez et al. (2012).

Coupled stress case

In order to study the combined effect of the stress components on the energy barrier, three cross-slip possibilities were considered: (A) compression on the glide plane and expansion on the conjugate plane, (B) compression on the glide plane and bowing-out on the conjugate plane and (C) expansion and bowing-out on the conjugate plane. As in the previous case, the activation enthalpy obtained from DD simulations and the two formulations of the LT model of cross-slip analyzed in this work (Kang et al., 2014; Malka-Markovitz and Mordehai, 2019) are in good agreement (see figure 3.11). The effect of applying a coupled compressive stress on the glide plane lead to the largest decrease in the energy barrier (see figures 3.11 (A) and (B)). These results resemble the effect applying an uncoupled compressive stress on the glide

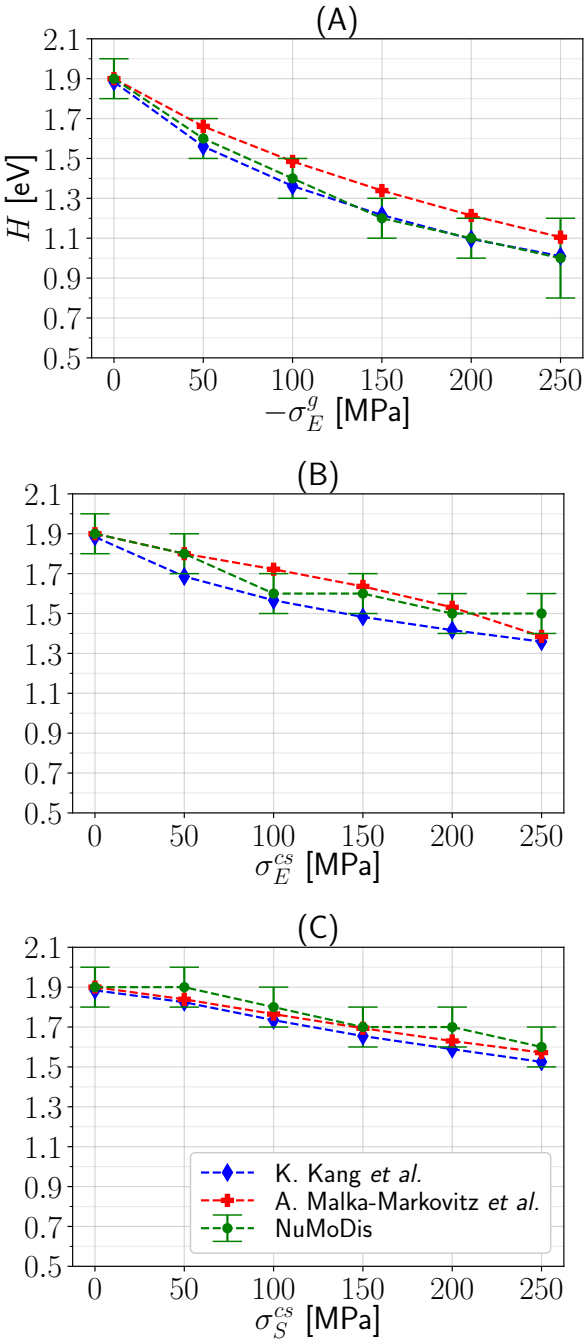

Figure 3.10: The effect of stress on the energy barrier: (A) $\sigma_S^g = \sigma_E^{cs} = \sigma_S^{cs} = 0$, (B) $\sigma_S^g = \sigma_E^g = \sigma_S^{cs} = 0$ and (C) $\sigma_S^g = \sigma_E^g = \sigma_E^{cs} = 0$. The green circles represent the DD simulation results, the blue diamonds correspond to the LT model of Kang et al. (2014) (see equation 3.14) and the red crosses were obtained from the general expression for the activation enthalpy proposed by Malka-Markovitz and Mordehai (2019) (see equation 3.16).

plane (see figure 3.10 (A)), which also lead to an energy barrier reduction of roughly 50%.

The effect of applying coupled stresses on the conjugate plane only (see figure 3.11 (C)) was comparable of applying an uncoupled Schmid stress on the conjugate plane (see figure 3.10 (C)). In both cases, the energy barrier decreased up to 20%. These observations are validated by the atomistic simulations of Esteban-Manzanares et al. (2020), who studied the effect of stress in aluminum using MD and obtained the same qualitative results.

3.4 Conclusions and future work

In this work, the unstressed constriction energy was equal to 0.7 eV, as reported by Ramírez et al. (2012). The effect of pure compressive stress in the range of -50 to -250 MPa on the constriction energy was negligible, in agreement with Püschl (1990).

The unstressed energy barrier was found to be 1.9 eV, as obtained by Ramírez et al. (2012). However, it does not lie within the experimental range of 1.15±0.37 eV measured by Bonneville et al. (1988). On the other hand, the energy barrier could be reduced by applying an external stress, leading to an energy barrier in better agreement with the experimental results. The most effective way of reducing it, was by pure compression on the glide plane. Furthermore, it was found using DDD simulations, that both the Schmid and Escaig stress on the conjugate plane have a comparable effect in reducing the energy barrier, in qualitative agreement with the atomistic simulations performed by Kang et al. (2014) in FCC nickel.

The energy barrier of FCC copper at zero stress has been obtained using the line LT model and atomistic simulations before. Some of them reported an energy barrier in better agreement with experiments (Saada, 1991; Rao et al., 1999). However, the LT model suffers from arbitrariness in the cut-off radius determination (Saada, 1991) and the atomistic simulations are highly sensitive to the interatomic potential used (Rao et al., 1999). In DDD simulations, these problems do not exist and the core-width used to compute the elastic energy can be calculated using the elastic theory of Schöck (2010) as suggested by Ramírez et al. (2012). Moreover, the effect of non-homogeneous stress on the energy barrier, like those generated by pile-ups and forest dislocations, can be more naturally studied using DDD simulations, in comparison with other simulation techniques.

The activation enthalpy obtained from DDD simulations was in excellent agreement with both the LT model of Kang et al. (2014) and the general expression for the activation enthalpy proposed Malka-Markovitz and Mordehai (2019). Since the

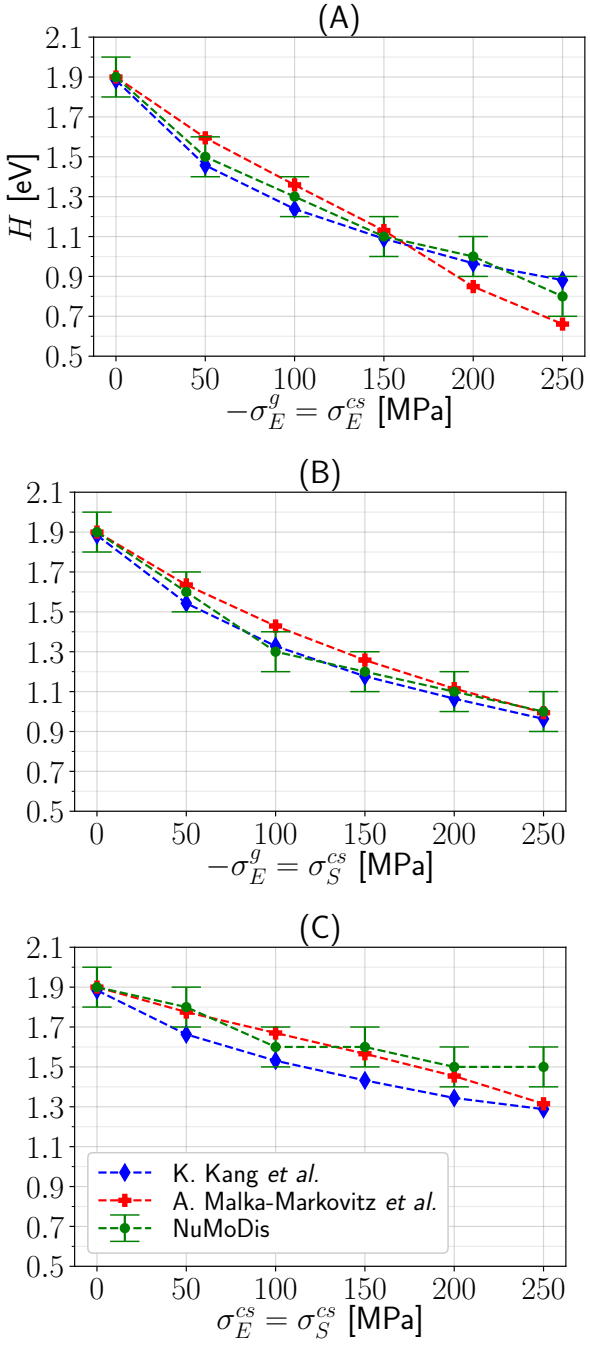

Figure 3.11: The effect of stress on the energy barrier: (A) $\sigma_S^g = \sigma_S^{cs} = 0$, (B) $\sigma_S^g = \sigma_E^{cs} = 0$ and (C) $\sigma_S^g = \sigma_E^g = 0$.

later is an analytical model, it can be easily implemented in a DDD code to calculate the activation enthalpy of screw segments.

Acknowledging a limitation of this work, a perfect screw dislocation in FCC crystals can be dissociated in a set of Fractional Partial Dislocations (FPD) pairs, instead of two Shockley partials with Burgers vectors $\boldsymbol{b}_1$ and $\boldsymbol{b}_2$. Based on the work of Banerjee et al. (2007), Ramírez et al. (2012) generalized the dissociation of perfect screw dislocations into n pairs of FPDs with Burgers vectors $\boldsymbol{b}_1/n$ and $\boldsymbol{b}_2/n$. By using 20 FPDs, they obtained an energy barrier reduction from 1.9 to 1.43 eV at zero stress, which lies within the experimental error of the energy barrier measured by Bonneville et al. (1988).

With regards to the LT model, the constant line energy per unit length T makes it impossible to distinguish between edge-like and screw-like constrictions. Thus, a more physical description of cross-slip can be made by letting the total energy depend on the angle between the Burgers vector and the local tangent vector (Kang et al., 2014; Dupuy and Fivel, 2002; Malka-Markovitz and Mordehai, 2018). In spite of it, the energy barrier calculated using the LT model was found to be in good quantitative agreement with the DDD simulations, at least for the case of dissociation into two partials. Hence, the orientation-dependent LT model might be in better agreement with DDD simulations that describe the dislocation core using more than a pair of FPDs.

As a final remark it is important to mention that the effect of Schmid stress on the glide plane should be considered in a future work. Since the FE mechanism assumes that a dislocation stops moving before cross-slipping due to the existence of invisible obstacles, the LT models based on the FE mechanism assume that the Schmid component of stress does not affect the cross-slip energy. However, a Schmid stress acting on the glide plane pressing both partials against an obstacle could reduce the stacking-fault region, which would be equivalent to the effect of applying a compressive Escaig stress on the glide plane. In order to study the general effect of all stress components on the cross-slip energy via the FE mechanism, a further contribution to the Escaig stress on the glide plane must be included as an implicit function of the Schmid stress on the glide plane. In that way, the presented LT models could be easily generalized.

Chapter 4

The rate of cross-slip

Many DDD simulations have successfully modeled plastic deformation in crystals (Zbib et al., 1998; Weygand et al., 2002; Verdier et al., 1998; Déprés et al., 2004b; Chaussidon et al., 2008). The first cross-slip model used in DDD simulations was proposed by Kubin et al. (1992). They postulated that the cross-slip probability explicitly depends on the resolved shear stress at the onset of stage-III plastic deformation, which is a macroscopic parameter obtained from the stress-strain curve of the material:

$$P = \beta \frac{L}{L_0} \exp\left(\frac{[\tau - \tau_{III}]V}{k_b T}\right) \delta t \tag{4.1}$$

where β is a scaling factor, L the screw-segment length, L_0 a reference length, τ the resolved shear stress in the primary plane, τ_{III} the resolved shear stress at the onset of stage III, V the activation volume, k_b the Boltzmann constant, T the absolute temperature and δt the time step. The values for the activation volume and resolved shear stress at the onset of stage III were obtained from experiments. However, the scaling factor and reference length were defined arbitrarily. In consequence, the absolute cross-slip rates were difficult to validate using other simulation methods.

Hussein et al. (2015) proposed a more physical model depending only on the microstructure parameters:

$$P = \omega \frac{L}{L_0} \exp\left(-\frac{\Delta E_c - V\Delta\sigma_E}{k_b T}\right) \delta t \tag{4.2}$$

where ω is the attempt frequency, ΔE_c the energy barrier required to form a constriction point on the screw dislocation, and $\Delta\sigma_E = \sigma_E^g - \sigma_E^{cs}$ the difference of Escaig stresses on the glide and cross-slip planes. Although the energy barrier and activation volume were obtained from atomistic simulations, the attempt frequency was determined using an heuristic argument, which introduced uncertainty in the absolute cross-slip rates.

The models 4.1 and 4.2 depend either on the Schmid or Escaig stresses, but not on both. Hence, they might be incomplete descriptions of the cross-slip rate. In fact, Kang et al. (2014) showed that both stress components have a comparable effect on the activation enthalpy as demonstrated in the previous chapter. This assertion has been thoroughly verified using different formulations of the LT model (Kang et al., 2014; Liu et al., 2019; Longsworth and Fivel, 2021a), linear-elasticity models (Longsworth and Fivel, 2021a; Kuykendall et al., 2020) and atomistic simulations (Kang et al., 2014; Esteban-Manzanares et al., 2020; Kuykendall et al., 2020; Liu et al., 2019). Therefore, the influence of all the stress components should be considered in the cross-slip rate.

More recently, Malka-Markovitz et al. (2021) calculated the cross-slip probability of screw segments in DD simulations using the following equation:

$$P = \beta \frac{L}{L_0} \exp\left(-\frac{\Delta H}{k_b T}\right) \delta t \tag{4.3}$$

where ΔH is the activation enthalpy. They considered the full effect of a general stress in the activation enthalpy by using the analytical expression of Malka-Markovitz and Mordehai (2019) to calculate it. Nonetheless, their semi-empirical model of the cross-slip rate requires the scaling factor β to be calibrated with atomistic results.

The present work provides a method to calculate the cross-slip rate of screw segments in DDD simulations without relying on scaling factors, yet able to reproduce atomistic results. The rest of this chapter is organized as follows. Section 4.1 introduces the rate equation proposed by Esteban-Manzanares et al. (2020) to compute the cross-slip probability of screw segments and the general expression obtained by Malka-Markovitz and Mordehai (2019) to calculate the activation enthalpy, section 4.2 presents the DDD simulation setup used for the presented results, section 4.3 shows a comparison between the annihilation rates of a screw dipole obtained from DDD simulations respect to atomistic results (Vegge et al., 2000; Oren et al., 2017), and section 4.4 presents the summary and conclusions of this work.

4.1 Theory

4.1.1 Cross-slip rate model of Esteban-Manzanares

Consider the potential energy $\Phi(y_1, .., y_N)$ of a system having only one saddle point P between two minima A and B. There is a unique hyper-surface S of dimension $N-1$ passing though P that is perpendicular to the level curves of Φ. Let S_0 be another hyper-surface with the same shape as S, but passing through A and oriented

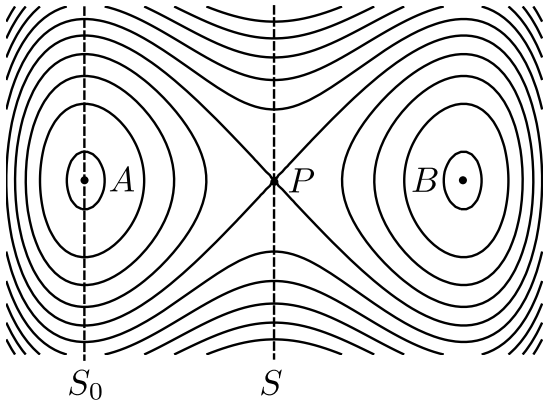

Figure 4.1: Contour plot of a potential with two minima and a saddle point. The solid lines represent level curves and the segmented ones hyper-surfaces.

such that the normal to S_0 at A is along the line of force leading to P (see figure 4.1). In this framework, the following constrained partition functions are defined (Vineyard, 1957):

$$Q_S = \rho_0 \int_S \exp\left(-\frac{\Phi}{k_b T}\right) dS \tag{4.4}$$

$$Q_0 = \rho_0 \int_{S_0} \exp\left(-\frac{\Phi}{k_b T}\right) dS_0 \tag{4.5}$$

and

$$Q_A = \rho_0 \int_A \exp\left(-\frac{\Phi}{k_b T}\right) dV \tag{4.6}$$

where ρ_0 is a normalization factor, k_b the Boltzmann constant, T the absolute temperature, $\int_S$ the surface integral over S, $\int_{S_0}$ the surface integral over S_0 and $\int_A$ the volume integral under S.

In Transition State Theory (TST), the rate of transition from state A to B can be expressed as (Vineyard, 1957):

$$\Gamma_{TST} = \sqrt{\frac{k_b T}{2\pi}} \frac{Q_S}{Q_A} \tag{4.7}$$

Multiplying and diving the latter equation by Q_0:

$$\Gamma_{TST} = \sqrt{\frac{k_b T}{2\pi}} \frac{Q_0}{Q_A} \frac{Q_S}{Q_0} = \sqrt{\frac{k_b T}{2\pi}} \frac{Q_0}{Q_A} \exp\left(-\frac{\Delta F}{k_b T}\right) \tag{4.8}$$

where ΔF is the free-energy change from A to P. The rate prefactor represents the effective frequency $\tilde{\nu}$:

$$\tilde{\nu} = \sqrt{\frac{k_b T}{2\pi}} \frac{Q_0}{Q_A} \tag{4.9}$$

In systems subject to constant stress, ΔF is the Gibbs free-energy $\Delta G \equiv \Delta H - T\Delta S$, where ΔH and ΔS are the activation enthalpy and entropy, respectively. Under this assumption, equation 4.8 can be rewritten as:

$$\Gamma_{TST} = \tilde{\nu} \exp\left(\frac{\Delta S}{k_b}\right) \exp\left(-\frac{\Delta H}{k_b T}\right) \tag{4.10}$$

In Harmonic TST (HTST), the potential energy is expanded in Taylor series around A up to second order, which leads to the following simplified rate equation (Vineyard, 1957; Granato et al., 1964):

$$\Gamma_{HTST} = \nu_1 \prod_{i=2}^{N} \frac{\nu_i}{\nu_i'} \exp\left(-\frac{\Delta H}{k_b T}\right) \tag{4.11}$$

where ν_i are the eigenfrequencies of state A and ν_i' those of the transition state P. In particular, ν_1 is the fundamental frequency.

A comparison between equations 4.10 and 4.11 shows that the entropic factor $e^{\Delta S/k_b}$ is approximately equal to $\prod_{i=2}^{N} \frac{\nu_i}{\nu_i'}$ if $\tilde{\nu}$ is considered to be ν_1.

The activation entropy can also be calculated using an empirical relation known as the Meyer-Neldel (MN) rule (Meyer and Neldel, 1937):

$$\Delta S = \frac{\Delta H}{T_m} \tag{4.12}$$

where T_m is the melting temperature.

Esteban-Manzanares et al. (2020) studied the effect of stress on the cross-slip rate in aluminum using atomistic simulations. They found a rate equation in great quantitative agreement with their results by applying the MN rule within the HTST framework:

$$\Gamma_{HTST} = \nu \frac{L}{L_n} \exp\left(-\frac{\Delta H}{k_b T}\left[1 - \frac{T}{T_m}\right]\right) \tag{4.13}$$

where $\nu = 10^{11}$ Hz is the fundamental frequency (Sobie et al., 2017), L the screw-dislocation length and L_n the nucleation length of cross-slip.

4.1.2 Nucleation length of cross-slip

In this study, the nucleation length was inferred from a LT model of cross-slip. According to said model, the dislocations can be approximated as flexible strings with line tension T_p (Kang et al., 2014):

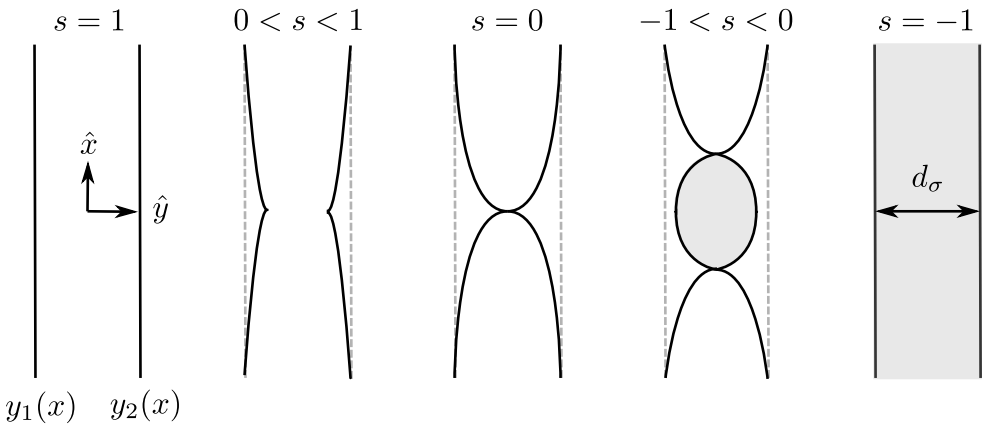

Figure 4.2: Cross-slip stages of a dissociated screw dislocation as function of the reaction coordinate s. The shaded region indicates that the stacking-fault is located the cross-slip plane.
Source: Figure adapted from Malka-Markovitz and Mordehai (2018).

$$T_p = \frac{\alpha \mu b^2}{2} \tag{4.14}$$

where α is the line-energy parameter, μ is the shear modulus and b the magnitude of the Burgers vector.

The total energy of the dislocations E_s is a function of the line tension, the shape of the partials $y_1(x)$ and $y_2(x)$ and the interaction energy between them $V(y_1, y_2)$ (Malka-Markovitz and Mordehai, 2018):

$$E_s = \int_{-\infty}^{+\infty} \left[\frac{1}{2} T_p (y_1')^2 + \frac{1}{2} T_p (y_2')^2 + V \right] dx \tag{4.15}$$

The prime symbol denotes the derivative with respect to the line direction x. Under Escaig stress σ_E, the equilibrium separation between the partials is given by (Malka-Markovitz and Mordehai, 2018):

$$d_\sigma = \beta(\sigma_E) d_0 \tag{4.16}$$

where:

$$\beta(\sigma_E) = \frac{1}{1 + \frac{\sqrt{3}b}{6\gamma}\sigma_E} \quad \text{and} \quad d_0 = \frac{\mu b^2}{24\pi\gamma} \frac{2 - 3\nu}{1 - \nu} \tag{4.17}$$

γ being the intrinsic stacking-fault energy and ν the Poisson's ratio. In absence of stress, $\beta(0) = 1$ and d_σ reduces to d_0 as expected.

The dissociation width $D(x)$ satisfies $D(x) = y_1(x) - y_2(x)$. Therefore, an infinite dislocation at equilibrium satisfies $D(x) = d_\sigma$ for all x.

The reaction coordinate s is a dimensionless variable defined in the interval [-1,1]. The cross-slip process as function of s is illustrated in figure 4.2. For $s \in (0, 1]$, the dislocation is fully contained in the glide plane at equilibrium. The dissociation width at the pinning point $x = 0$ decreases as s goes to 0 i.e. $D_s(0) = sd_\sigma$. At $s = 0$, the dislocation constricts, which means that $D_s(0) = 0$. For $s \in [-1, 0)$, the dislocation expands in the cross-slip plane. When only Escaig stresses are applied, the dissociation width at the pinning point can be expressed as $D_s(0) = |s|d_\sigma$. The cross-slip process finishes when $s = -1$, as the dislocation is completely contained in the conjugate plane at equilibrium.

The energy functional $E_s(y_1, y_2)$ can be minimized using the Euler-Lagrange equation in order to find the cross-slip trajectory. Applying the boundary conditions $D_s(x \to \infty) = d_\sigma$ and $D'_s(x \to \infty) = 0$, it can be shown that the dissociation width in the glide plane satisfies (Malka-Markovitz and Mordehai, 2018):

$$x = d_\sigma \sqrt{\frac{T_p}{4}} \int_s^{D_s^*(x)} \frac{d\eta}{\sqrt{V(\eta)}} \tag{4.18}$$

where $D_s^* = D_s/d_\sigma$ is the normalized dissociation width between the partials and η an adimensional integration variable.

The linear approximation can be used to model the interaction force between the partials for distances near the equilibrium dissociation width d_0. This is called the Harmonic Approximation (HA) because the resulting interaction energy is a quadratic function of their separation. It can be shown that using this approximation, the interaction potential in the glide plane is given by (Malka-Markovitz and Mordehai, 2018):

$$V_{HA}^g(D^*) = \frac{1}{2}(\gamma d_0)(D^* - 1)^2 \tag{4.19}$$

Substituting equation 4.19 into 4.18 gives the relation between x and D^*:

$$x = \beta_g \sqrt{\frac{T_p d_0}{2\gamma}} \int_s^{D_s^*(x)} \frac{d\eta}{|\eta - 1|} \tag{4.20}$$

The notation β_g means $\beta(\sigma_E^g)$, where σ_E^g is the Escaig stress on the glide plane (see equation 4.17).

Thus, the normalization factor in front of the integral could be interpreted as the dislocation length bowing towards the constriction (Malka-Markovitz and Mordehai, 2018). For that reason, it was used in the present work to estimate the nucleation length of cross-slip L_n on the glide plane:

$$L_n = \beta_g \sqrt{\frac{T_p d_0}{2\gamma}} \tag{4.21}$$

Since σ_E^g appears in the denominator of β_g, L_n decreases with positive Escaig stress on the glide plane. In the convention of Malka-Markovitz and Mordehai (2018), a positive Escaig stress shrinks the dissociation width, which increases the cross-slip probability.

4.1.3 Activation enthalpy of cross-slip

The activation enthalpy can be also obtained from the LT model of cross-slip. The first formulation of it was proposed by Stroh (1954) to estimate the effect of Escaig stress in the constriction energy. Kang et al. (2014) generalized it by including the influence of Schmid stress in the cross-slip plane. Later on, Malka-Markovitz and Mordehai (2019) generalized the LT model of Stroh (1954) for an arbitrary interaction force between the partials, and then solved it analytically by using the linear approximation for the interaction force. Malka-Markovitz and Mordehai (2019) assumed the FE mechanism in their LT model, which implies that the dislocation does not move before cross-slipping. As a consequence, the Schmid stress on the glide plane σ_S^g does not appear in their model. They found a general expression for the cross-slip energy as a function of the separation between the constriction points l, the elastic constants and the local stress. In their model, the cross-slip energy reaches its maximum when the separation between the constriction points $l = l_c$ satisfies the following critical equation (Malka-Markovitz et al., 2021):

$$\frac{1.55}{\cosh^2(l_c)} - \frac{3\delta}{\beta_{cs}} l_c^2 = 2E^* \tag{4.22}$$

where δ is a function of the Schmid stress on the cross-slip plane σ_S^{cs} and E^* is a dimensionless off-set in the interaction energy between the glide and cross-slip planes:

$$\delta = \frac{1}{6}\left(\frac{b\sigma_S^{cs}}{\gamma}\right)^2 \quad \text{and} \quad E^* = \ln\left(\frac{\beta_{cs}}{\beta_g}\right) \tag{4.23}$$

The notation β_{cs} means $\beta(\sigma_E^{cs})$, where σ_E^{cs} is the Escaig stress on the cross-slip plane (see equation 4.17). Once the value of l_c was found, the activation enthalpy ΔH is obtained by evaluating the corrected cross-slip energy $H(\sigma, l)$ at $l = l_c$ (Malka-Markovitz et al., 2021):

$$\frac{H(\sigma, l)}{\Delta E_0} = \frac{\beta_g}{2} + \left(\frac{\beta_{cs}}{2}\right)\left[\tanh(l) - \frac{2\alpha_{Ls}}{1.55} l E^* - \frac{\alpha_{Ls}^3}{1.55}\frac{\delta}{\beta_{cs}} l^3\right] \tag{4.24}$$

where ΔE_0 is the unstressed energy barrier and $\alpha_{Ls} \approx 0.6$. In the present work, we consider the energy barrier to be the maximum of equation 4.24. For that reason,

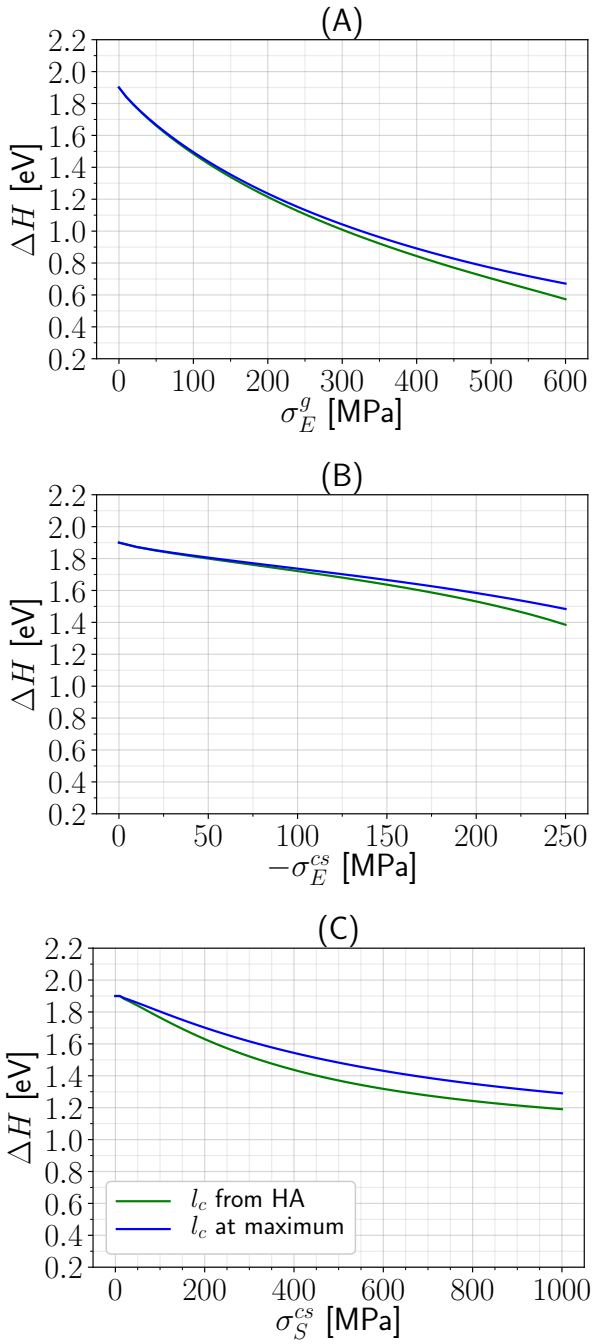

Figure 4.3: Effect of the stress components on the energy barrier for: (A) compressive Escaig stress on the glide plane ($\sigma_S^g = \sigma_E^{cs} = \sigma_S^{cs} = 0$), (B) expansive Escaig stress on the cross-slip plane ($\sigma_S^g = \sigma_E^g = \sigma_S^{cs} = 0$) and (C) Schmid stress on the cross-slip plane ($\sigma_S^g = \sigma_E^g = \sigma_E^{cs} = 0$). The green line shows the energy barrier obtained by evaluating H at the solution of equation 4.22. The blue line show the energy barrier obtained by evaluating H at the solution of equation 4.25.

the critical relation for l_c was obtained by differentiating equation 4.24 with respect to l and equating it to zero, which gives:

$$\frac{1.55}{\cosh^2(l_c)} - \frac{3\alpha_{Ls}^3\delta}{\beta_{cs}} l_c^2 = 2\alpha_{Ls}E^* \tag{4.25}$$

Figure 4.3 shows the minor difference between evaluating $H(\sigma, l)$ at the critical length given by equations 4.22 and 4.25 for FCC copper. The magnitude of the Burgers vector was assumed to be $b = 2.55$ Å, the intrinsic stacking-fault energy $\gamma = 42$ mJ/m^2 and the unstressed energy barrier $\Delta E_0 = 1.9$ eV. Notice that the activation enthalpy obtained by evaluating $H(\sigma, l)$ at the solution of equation 4.22 is slightly lower than the maximum of $H(\sigma, l)$ for a given stress condition.

4.2 Methodology

The Metropolis Monte Carlo (MMC) method generates configurations according to a prescribed probability distribution. Since the time progression leading to an equilibrium state is stochastic, there is no information about dynamics of the system. Moreover, it is not known how fast the equilibrium state is reached. Fortunately, there are other Monte Carlo methods that take into consideration the physical time in simulations. The kinetic Monte Carlo (kMC) method can be used to account for the time increments related to the kinetics of the system. In the MMC method, the transition probability between two states depends on the activation energy, which is time-independent, but in the kMC method, the transition probability is calculated using a rate equation Γ that implicitly depends on the activation energy. For single processes (such as cross-slip, where the screw segment can only lie either on its glide plane or on its conjugate plane), the reciprocal of the rate is equal to the average time required for the process to occur. Therefore, the probability that such transition occurs within an specified time step Δt is simply given by:

$$P = \Gamma \Delta t \tag{4.26}$$

The cross-slip mechanism is the main cause of slip irreversibility during cyclic loading (Mughrabi, 2009; Lukáš and Klesnil, 1973). Therefore, the cross-slip events are very important to determine the microstructure evolution accurately. The cross-slip process in DDD simulations is modeled using a kMC method. The screw chains were identified among the dislocation lines every simulation step. A dislocation chain was considered to have a screw character if the angle between its Burgers vector and line direction was smaller than one degree. For each screw chain, a random number R between 0 and 1 was generated. If the cross-slip probability P was larger than

R, the glide plane of the corresponding screw segment was changed to its deviated plane. Else, the system remained unchanged.

The cross-slip process in DDD simulations is usually modeled using a kinetic Monte Carlo method (Kubin et al., 1992; Hussein et al., 2015; Déprés et al., 2004b; Malka-Markovitz et al., 2021). In the present work, the cross-slip rate proposed by Esteban-Manzanares et al. (2020) (see equation 4.13) is implemented in the DDD code NuMoDis (Drouet et al., 2014) to compute the cross-slip probability of screw segments. Thus, the probability of a screw segment of length L to cross-slip during a time step δt is given by:

$$P = \nu \frac{L}{L_n} \exp\left(-\frac{\Delta H}{k_b T}\left[1 - \frac{T}{T_m}\right]\right) \delta t \tag{4.27}$$

where $\nu = 10^{11}$ Hz is the fundamental frequency (Sobie et al., 2017), L_n the nucleation length of cross-slip, k_b the Boltzmann constant, T the absolute temperature, T_m the melting temperature and ΔH the activation enthalpy.

The activation enthalpy was obtained by evaluating the cross-slip energy $H(\sigma, l)$ at the critical length satisfying equation 4.25. The only free parameter in the theory of Malka-Markovitz and Mordehai (2019) is the unstressed energy barrier ΔE_0, which can be obtained either from line tension models (Kang et al., 2014; Malka-Markovitz and Mordehai, 2019), atomistic simulations (Oren et al., 2017; Liu et al., 2019; Esteban-Manzanares et al., 2020; Kuykendall et al., 2020) or DDD simulations (Ramírez et al., 2012; Longsworth and Fivel, 2021a). In the present chapter, the energy barrier of FCC copper $\Delta E_0 = 1.9$ eV was obtained from DDD simulations (Longsworth and Fivel, 2021a) to make the work independent of other numerical results.

The nucleation length was deduced from the theory of Malka-Markovitz and Mordehai (2018) (see equation 4.21). In said model, the only free variable is the line tension T_p, which is proportional to the line-energy parameter α (see equation 4.14). Typical values of the line-energy parameter are in the range between 0.1 and 0.6. Kang et al. (2014) studied the cross-slip energy of FCC nickel using MD simulations and their line tension model. They reported a reasonable agreement between their atomistic simulations and LT model for α values in the range from 0.1 to 0.6. In chapter 3, the line-energy parameter was calibrated using the LT model of Kang et al. (2014). In order to obtain an unstressed energy barrier of 1.9 eV in FCC copper, the line-energy parameter was adjusted to 0.22. For that reason, an average line-energy value of 0.3 was used in the present work.

In order to calculate the activation enthalpy and the nucleation length, σ_S^g, σ_E^g, σ_S^{cs} and σ_E^{cs} must be obtained as functions of the total stress tensor components. Therefore, the Cartesian coordinate system was rotated such that the $[\overline{111}]$ direction

Property	Value
a_0	3.61 Å (Davey, 1925)
b	$a_0/\sqrt{2}$ (Kittel and McEuen, 2018)
d	$a_0/\sqrt{3}$ (Kittel and McEuen, 2018)
γ	42 mJ/m^2 (Bonneville and Escaig, 1979)
ν	0.324 (Ledbetter and Naimon, 1974)
μ	54.6 GPa (Schmauder and Mishnaevsky, 2008)
T_m	1358 K (Mangum et al., 2001)
B	1.5 $\times 10^{-5}$ Pa-s (Philibert, 1979)

Table 4.1: Parameter values used for FCC copper; a_0 is the lattice parameter, b the magnitude of the Burgers vector, d the interplanar separation, γ the intrinsic stacking-fault energy, ν the Poisson's ratio, μ the shear modulus, T_m is the melting temperature and B the viscous drag coefficient at room temperature.

h [Å]	L_i [Å]	y_i [Å]	y_c [Å]	δt
$6d \approx 12.5$	$2000b \approx 5105.3$	$10b \approx 25.5$	4.4	0.0001
$25d \approx 52.1$	$350b \approx 893.4$	$30b \approx 76.6$	18.5	0.01

Table 4.2: Dipole dimensions in the DDD simulations; h is the dipole height, L_i the initial dislocation length, y_i the initial separation of the dislocations in the direction of $\hat{y}$, y_c their separation at the common cross-slip plane and δt the time step.

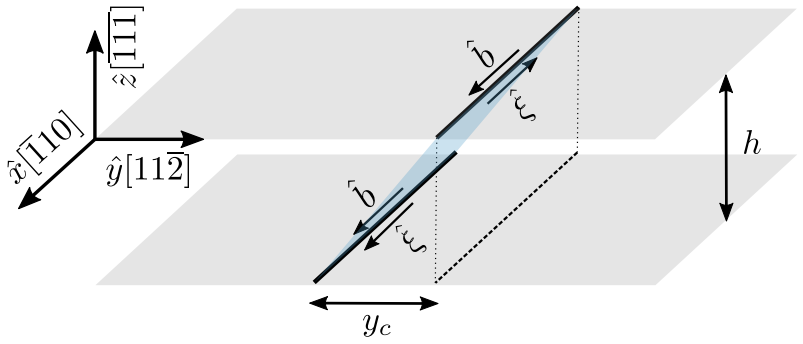

Figure 4.4: Screw dipole of height h contained in the glide plane (shaded in gray). The dislocation separation at the common cross-slip plane (shaded in blue) is denoted as y_c.

matched with the $\hat{z}$ axis and the Burgers vector $[\bar{1}10]$ with the $\hat{x}$ axis. The resulting equations of the stress components were given by:

$$\sigma_S^g = \sigma_{xz} \tag{4.28}$$

$$\sigma_E^g = \sigma_{yz} \tag{4.29}$$

$$\sigma_S^{cs} = \frac{2\sqrt{2}\sigma_{xy} - \sigma_{xz}}{3} \tag{4.30}$$

$$\sigma_E^{cs} = \frac{7\sigma_{zy} + 2\sqrt{2}(\sigma_{yy} - \sigma_{zz})}{9} \tag{4.31}$$

The cross-slip mechanism has been extensively studied using atomistic simulations. In particular, Vegge et al. (2000) and Oren et al. (2017) have investigated the kinetics of cross-slip in FCC copper. Both studies offer a quantitative analysis of the activation enthalpy and annihilation rate of screw dipoles, which can be used as a standard to compare against other results. For the purpose of comparison, similar dipole dimensions to theirs were used in the present DDD simulations of FCC copper.

Consider a screw dipole of height h with both dislocations arrested in the glide plane, at the intersection with the common cross-slip plane. In FCC structures, the angle between two conjugate planes is $\theta_c = \arccos\left(\frac{1}{3}\right) \approx 70.5°$. Consequently, the dislocation separation in the direction of $\hat{y}$ is $y_c = h \cot \theta_c$ (see figure 4.4). If under these conditions one of the dislocations cross-slips, it would start gliding in the conjugate plane and both dislocations would annihilate each other. For that reason, the activation enthalpy and annihilation rate were calculated at the intersection with the common cross-slip plane.

The dipole dimensions, physical properties and elastic constants used in the DDD simulations are shown in tables 4.1 and 4.2.

4.3 Results and discussion

4.3.1 Activation enthalpy of cross-slip

The DDD simulations were performed using non-dissociated dislocations. In consequence, there were no internal Escaig stresses induced by the screw dipole in the present DDD simulations. According to linear elasticity theory, a screw dislocation with Burgers vector $\boldsymbol{b} = b\hat{\boldsymbol{x}}$ generates non-zero stress components σ_{xy} and σ_{xz} (Anderson et al., 2017). As a result, a perfect screw dipole can only produce Schmid

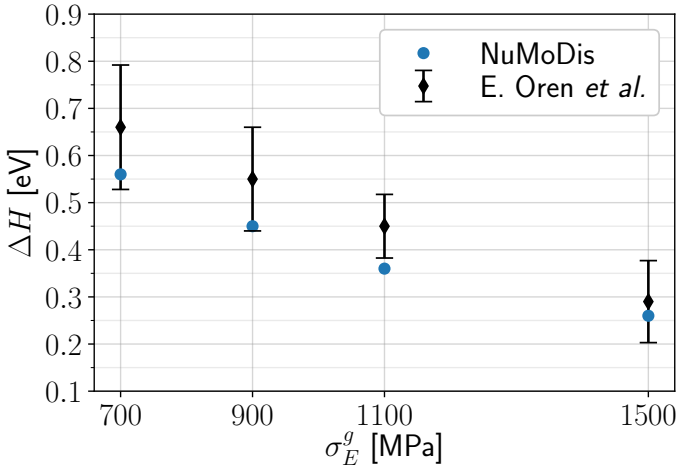

Figure 4.5: Activation enthalpy of the 50-Å-high dipole as function of compressive Escaig stress applied on the glide plane. The blue circles are the activation enthalpies obtained from the DDD simulations using the model of Malka-Markovitz and Mordehai (2019). The black diamonds are the data points obtained by Oren et al. (2017) using MD simulations.

stresses on the glide and cross-slip planes (see equations 4.28 and 4.30). However, a dissociated screw dipole could create both Schmid and Escaig stresses on the glide and cross-slip planes. The screw component of the Shockley partials would induce Schmid stresses on the glide and cross-slip planes as the perfect screw dipole. On the other hand, the edge components of the Shockley partials would introduce Escaig stresses on the glide and cross-slip planes. It can be shown that an edge dislocation with line direction $\hat{\boldsymbol{\xi}} = \hat{\boldsymbol{x}}$ and Burgers vector $\boldsymbol{b} = b\hat{\boldsymbol{y}}$ generates non-zero stress components σ_{xx}, σ_{yy}, σ_{zz} and σ_{yz} (Anderson et al., 2017). For that reason, the edge component of the Shockley partials will introduce Escaig stresses on the glide and cross-slip planes of a dissociated screw dipole (see equations 4.29 and 4.31).

In order to compensate for the absence of internal Escaig stresses in the DDD simulations, a compressive Escaig stress of 1300 MPa was applied on the glide plane of the 13-Å-high dipole. As a result, the activation enthalpy decreased to $\Delta H =$ 0.295 eV. In contrast, the internal Escaig stress in the 50-Å-high dipole are expected to be less strong than in the 13-Å-high dipole. For that reason, no external stress was applied in the glide plane of the 50-Å-high dipole to account for the internal stress. Oren et al. (2017) used MD simulations to obtain the activation enthalpy as function of compressive Escaig stress on the glide plane. Figure 4.5 shows the activation enthalpy of the 50-Å-high dipole obtained using DDD simulations. The atomistic results of Oren et al. (2017) are also plotted for reference. The activation enthalpy at σ_E^g =1500 MPa was approximately 0.3 eV using both simulation techniques. The

σ_E^g [MPa]	ΔH [eV]	L [Å]	L_n [Å]	Γ^0_{HTST} [Hz]
0	1.190	4862	32.9	3.93×10^{17}
1300	0.295	4862	10.0	6.07×10^{14}

Table 4.3: Parameter values obtained from DDD simulations for the 13-Å-high dipole; σ_E^g is the compressive Escaig stress applied on the glide plane of the screw dipole, ΔH the activation enthalpy, L the screw-segment length, L_n the nucleation length and $\Gamma^0_{HTST} = \nu \frac{L}{L_n} \exp\left(\frac{\Delta H}{k_b T_m}\right)$ the constant prefactor of equation 4.13.

results were in good quantitative agreement. Although not all the values obtained in this work lie within their uncertainty, the largest discrepancy was only a small fraction of an electron-volt.

Oren et al. (2017) deduced an energy barrier of 1.05 ± 15% eV, which lies within the experimental value of 1.15 ± 0.37 eV measured by Bonneville et al. (1988). They inferred this value from their data by double interpolation to both zero applied stress and infinite dipole height. On the other hand, the energy barrier of 1.9 eV used in this work was almost the double of their estimate. In spite of it, the simulation results are in good agreement because the activation enthalpy does not decrease linearly with the applied stress. Instead, the activation energy reduces to almost half of its value at 250 MPa (Longsworth and Fivel, 2021a), but decreases only 0.3 eV when increasing the stress magnitude from 700 to 1500 MPa.

4.3.2 Nucleation rate of cross-slip

Figure 4.6 shows the Arrhenius of the cross-slip rate for the 13-Å-high dipole. The logarithm of the annihilation rates obtained by Vegge et al. (2000) using MD simulations are also plotted for reference. Since their data points could be fitted well with a straight line, they proposed the following rate equation:

$$\Gamma = \frac{1}{\tau} = \Gamma_0 \exp\left(-\frac{\Delta H}{k_b T}\right) \tag{4.32}$$

where τ is the average annihilation time and Γ_0 is a the rate prefactor. The least squares fit lead them to the values $\Delta H = 291 \pm 27$ meV and $\Gamma_0 = 7.8 \times 10^{14}$ Hz.

The parameter values obtained from DDD simulations are shown in table 4.3. The rate-prefactor value calculated using the model of Esteban-Manzanares et al. (2020) was similar to the one proposed by Vegge et al. (2000) to fit their atomistic data (6.07×10^{14} and 7.8×10^{14} Hz, respectively). Therefore, the cross-slip rates were in good quantitative agreement as observed in figure 4.6. It is worth mentioning that the external Escaig stress only affects the dissociation width. For that reason,

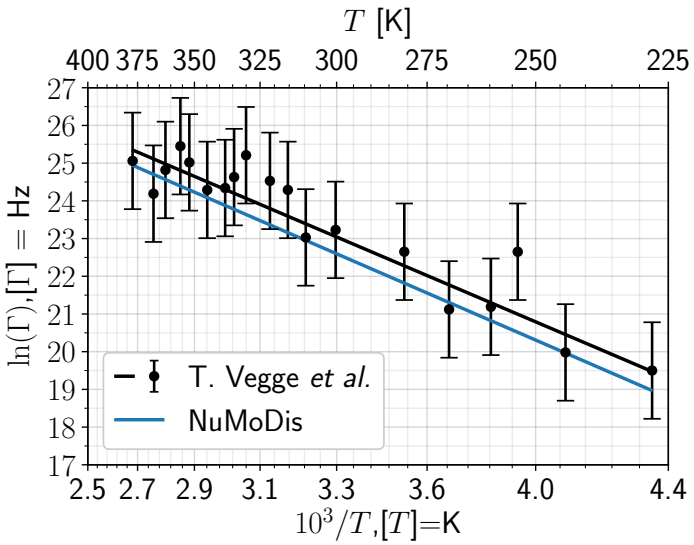

Figure 4.6: Arrhenius plots of the cross-slip rate for the 13-Å-high dipole. The black dots with error bars represent the 19 data points obtained by Vegge et al. (2000) using MD simulations. The black line corresponds to the linear fit proposed by Vegge et al. (2000) to model their atomistic data. The blue line represents the model of Esteban-Manzanares et al. (2020) used in the DDD simulations.

the screw-segment length remains unaffected by the applied Escaig stress for a given dipole height (see the third column of table 4.3).

Figure 4.7 shows the Arrhenius plots of the cross-slip rate for the 50-Å-high dipole as function of compressive Escaig stress applied on the glide plane. Most values were in good quantitative agreement. The harmonic approximation used in the rate equation assumes that the transition state is close to the original one. This is most accurate at sufficiently low temperatures, when the transition cannot be induced by thermal activation. In the investigated temperature range, the activation enthalpy is larger than the thermal energy. For that reason, the cross-slip rates calculated using the HTST should be valid.

σ_E^g [MPa]	ΔH [eV]	L [Å]	L_n [Å]	Γ^0_{HTST} [Hz]
0	1.55	447	32.9	8.14×10^{17}
700	0.56	447	14.8	3.61×10^{14}
900	0.45	447	12.8	1.58×10^{14}
1100	0.36	447	11.2	8.86×10^{13}
1500	0.26	447	9.1	4.64×10^{13}

Table 4.4: Parameter values obtained from DDD simulations for the 50-Å-high dipole.

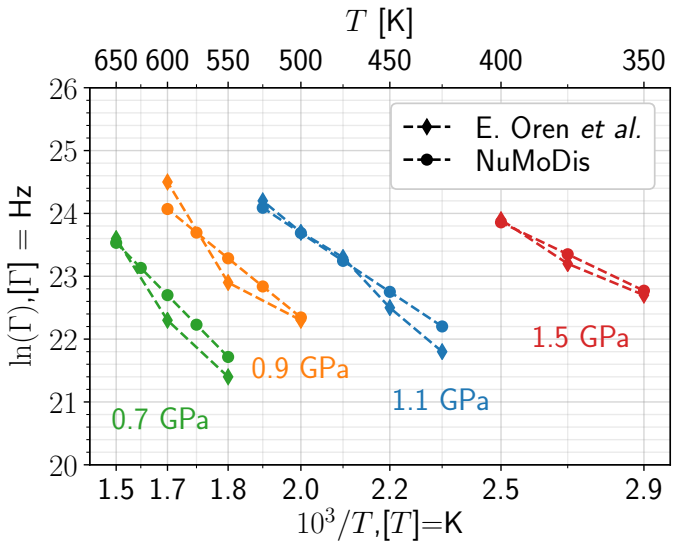

Figure 4.7: Arrhenius plots of the cross-slip rate for the 50-Å-high dipole as function of compressive Escaig stress applied on the glide plane. The dots are the cross-slip rates obtained from the DDD simulations using the model of Esteban-Manzanares et al. (2020). The diamonds correspond to the atomistic results of Oren et al. (2017). The temperature range goes from 350K to 650K in steps of 25K.

In faulted screw dipoles, the compressive Escaig stresses in the glide plane are expected to increase with decreasing dipole height (Rasmussen et al., 2000). As a result, the nucleation length modeled using equation 4.21 would decrease with decreasing dipole height. However, there are no internal Escaig stresses in perfect screw dipoles. In consequence, the nucleation length was 32.9 Å at zero applied stress, independently of the dipole height (compare tables 4.3 and 4.4). As reference, the nucleation length of aluminum was approximately 28 Å according to Esteban-Manzanares et al. (2020).

4.4 Summary and conclusions

The objective of this work is to propose a method to compute the cross-slip rate of screw segments in DDD simulations without relying on scaling factors, yet able to reproduce atomistic results. Thus, all the input information used to compute the cross-slip rate was retrieved from DDD simulations. The stress and forces on the dislocation segments were calculated using the analytical expressions obtained by Cai et al. (2006), who developed the non-singular theory of dislocations. As a consequence, the core-width parameter introduced to obtain those non-singular expressions influenced the DDD simulations strongly. In particular, atomistic and

continuum energies are only comparable if the core-width value is deduced using both an atomistic and a continuum dislocation model. Since the aim was to compare the DDD simulations' outcome with previous atomistic results, the core-width value was calculated using the theory of Schöck (2010) as proposed by Ramírez et al. (2012). They deduced an expression for the core-width parameter based on both atomistic and continuum dislocation models.

The cross-slip rate of screw segments was calculated using the atomistic-based model proposed by Esteban-Manzanares et al. (2020) (see equation 4.13), which combines the HTST framework and the NM rule. In that model, the only two input parameters that depend on the local stress are the activation enthalpy and the nucleation length. Both quantities were obtained from the LT model of cross-slip as follows.

The activation enthalpy was obtained by evaluating the cross-slip energy $H(\sigma, l)$ at the critical length satisfying equation 4.25. In the model of Malka-Markovitz and Mordehai (2019), the activation enthalpy is a function of the microstructure parameters and the stress components acting on the crystallographic planes, which are easily accessible from the DDD simulation. With the aim of calibrating their model, the unstressed energy barrier was set to 1.9 eV as obtained with the DDD simulations of FCC copper (Ramírez et al., 2012; Longsworth and Fivel, 2021a).

The nucleation length was inferred from the LT model of cross-slip developed by Malka-Markovitz and Mordehai (2018) (see equation. 4.21). It is expressed as a function of the line tension, the microstructure parameters and the Escaig stress on the glide plane. In said model, the only free variable is the line tension, which is proportional to the line-energy parameter (see equation 4.14). Typical values of the line-energy parameter are in the range between 0.1 and 0.6 (Kang et al., 2014). For that reason, an average line-energy value of 0.3 was used in the present work.

In summary, the cross-slip modeling proposed in this paper by combining equations 4.13, 4.21 and 4.24 with $\alpha = 0.3$ and $\Delta E_0 = 1.9$ eV can be reliably used in DDD simulations of FCC copper. The activation enthalpies and cross-slip rates obtained were in good quantitative agreement with the atomistic results of Oren et al. (2017) and Vegge et al. (2000). These results ratify that the HTST approximation and the MN rule are valid in the studied temperature range and stress conditions.

Chapter 5

The effect of cross-slip during cyclic fatigue

When a material is subjected to cyclic fatigue, its temperature increases. This well-known effect is usually called self-heating (see chapter 1). Over the past three decades, experimental approaches based on self-heating measurements during cyclic loading have been employed to determine the fatigue limit of materials (Galtier, 1993; Luong, 1998; La Rosa and Risitano, 2000; Yang et al., 2001; Krapez et al., 2000; Krapez and Pacou, 2002). In said experimental approaches, the fatigue limit is identified with the range of applied stresses corresponding to an abrupt increase of the probe's temperature. Although the so-called self-heating method has been able to fairly estimate the fatigue limit in many cases, the temperature as a physical quantity cannot be directly considered as an indicator of fatigue damage (Meneghetti, 2007). In fact, it is widely acknowledged that temperature can also increase due to non-damaging phenomena during reversible cyclic deformation (Halford, 1966; Blotny and Kaleta, 1986). In strong contrast to the direct measurement of temperature at the specimen's surface, energy estimations are expected to be invariant with respect to the loading frequency and the specimen geometry (Meneghetti, 2007). According to the first law of thermodynamics, one part of the mechanical work transferred to the material is dissipated through self-heating and the rest is converted into stored energy in the form of plastic deformation (Halford, 1966; Meneghetti, 2007). In order to improve the fatigue characterization of materials, experimental methods based on the quantification of a particular form of energy have been proposed. Several candidates have been postulated as plausible indicators of fatigue damage, most notably the mechanical work (Feltner and Morrow, 1961), the stored energy (Wan et al., 2014; Warren and Wei, 2010), the dissipated energy (Charkaluk et al., 2002; Meneghetti, 2007; Wang et al., 2017; Meneghetti et al., 2015) or even the plastic strain energy (Halford, 1966; Ellyin and Kujawski, 1984; Duyi and Zhenlin, 2001). It has been reported that most of the mechanical work is converted into heat, specially in the VHCF regime (Halford, 1966). Moreover, the dissipated energy is easier to be measured compared to the stored energy, which requires the previous

determination of the input mechanical work. For these reasons, the present work will be focused on the dissipated energy as a damage indicator.

In the VHCF regime, the fatigue damage can be attributed to the slip irreversibilities during cyclic loading. Many authors have reported that the cross-slip mechanism strongly affects the slip irreversibilities of ductile metals (Mughrabi, 2001; Déprés et al., 2006; El-Awady et al., 2008; Hilgendorff et al., 2013). Thus, the first objective of this chapter is to study the effect of cross-slip on the dislocation density evolution during cyclic loading, with particular focus on the firsts fatigue cycles of the ultrasonic regime. In the present work, the extent of plastic damage to the microstructure due to cross-slip was quantified using the dissipated energy. For that reason, the second objective of this chapter is to present a DDD simulation procedure to calculate the dissipated energy of dislocations. Section 5.1 reviews the models used to calculate cross-slip of screw segments during cyclic loading and presents the model used in the DDD simulations to calculate the dissipated energy. Section 5.2 shows the corresponding simulation setups. For its simplicity, the effect of cross-slip during cyclic fatigue on an isolated screw dislocation was analyzed first. In order to consider a more complex case, the effect of cross-slip on a network of twelve dislocations with an arbitrary angle between their Burgers vector and line direction was also studied. Subsequently, section 5.3 discusses the effect of cross-slip on the dislocation density and dissipated energy. Finally, section 5.4 presents the summary and conclusions of this chapter.

5.1 Theory

5.1.1 Energy balance during cyclic fatigue

The energy balance after a loading cycle involves three quantities, namely the mechanical work supplied to the specimen, the dissipated energy associated to the self-heating and the stored energy into the microstructure (Halford, 1966; Connesson et al., 2011). It is widely acknowledged that materials undergoing mechanical deformation produce heat, even when loaded in the macroscopic elastic regime (Seelan et al., 2020). The Fourier's law modelling the heat conduction of a solid can be expressed in terms of the heat sources, namely the amount of heat energy per unit volume generated per unit time. In the case of a self-heated metal, the temperature variation originates from two sources, specifically the thermoelastic heat source θ_{TE} associated to the thermal expansion of the crystalline structure (Chrysochoos et al., 2008), and the dissipative heat source θ_D caused by plasticity phenomena (Connesson et al., 2011). As a consequence, the thermoelastic heat source provokes a cyclical variation of the temperature, whereas the dissipative heat source causes an increase

on the mean temperature of the material (Seelan et al., 2020). Their associated energy can be obtained by integrating the heat sources over time (Chrysochoos et al., 2008):

$$\Delta E_{TE} = \int_{\text{cycle}} \theta_{TE} dt = 0 \qquad \Delta E_D = \int_{\text{cycle}} \theta_D dt \tag{5.1}$$

It has been conclusively verified using infrared thermography that the thermoelastic energy per cycle ΔE_{TE} vanishes (Chrysochoos et al., 2008). In contrast, the dissipated energy ΔE_D monotonically increases over time because θ_D is always larger than zero for dissipative materials. Intrinsic dissipation has been attributed to grain boundary sliding and dislocation movements (Seelan et al., 2020). Most importantly, it has been shown that most of the dissipated heat can be attributed to dislocation motion in the majority of materials (Mareau et al., 2013).

Mechanical deformation directly affects the stored energy that characterizes the crystalline imperfections, such as dislocations, vacancies, stacking-faults and twins (Rosakis et al., 2000). The stored energy is defined as the contribution of internal stress due to defects. Applying the first law of thermodynamics to one loading cycle, the input work W is equal to the stored energy ΔE_S plus the dissipated energy (Connesson et al., 2011):

$$W = \int_{\text{cycle}} \sigma \dot{\epsilon} dt = \Delta E_S + \Delta E_D \tag{5.2}$$

where σ is the stress and $\dot{\epsilon}$ the total strain rate.

In order to estimate the mechanical work experimentally, the time-resolved evolution of the stress and total strain must be obtained. In the case of ultrasonic fatigue at 20 kHz, the required time resolution is one microsecond or less. For that reason, there are very few experimental attempts to estimate the mechanical work or the stored energy in the VHCF regime. More recently, an experimental method for microsecond time-resolved x-ray diffraction has been proposed to estimate the stress and total strain (Ors et al., 2019) as a first step to compute the stored energy. Despite the significant progress to estimate the mechanical work, the dissipated energy must be simultaneously obtained in order to compute the stored energy (Connesson et al., 2011). For that reason, the present work will only be focused on the dissipated energy as indicator of fatigue damage.

Considering the circumstance in which all plasticity is attributed to dislocations, the dissipated energy per unit cycle is directly available from DDD simulations. In the current work, the dissipated energy per unit cycle is calculated as (Lachowicz, 2001; Cui et al., 2017):

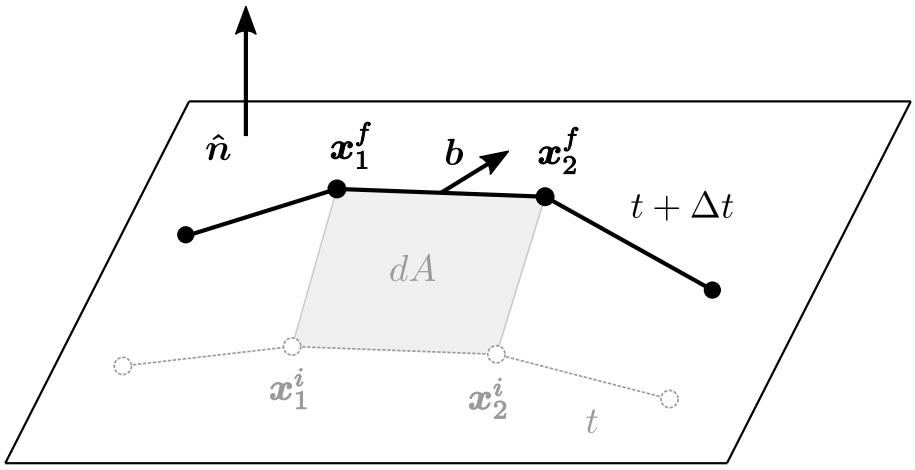

Figure 5.1: Diagram showing the nodes' positions of a segment at time t and at the next instant $t + \Delta t$. The shaded region denotes the incremental area swept by the dislocation segment.

$$E_D = \int_{\text{cycle}} \boldsymbol{\sigma} : \boldsymbol{d\epsilon}^p = \int_{\text{cycle}} \sum_{i=1}^{N} \boldsymbol{f}_i^{PK} \cdot \boldsymbol{v}_i dl_i dt \tag{5.3}$$

where $\boldsymbol{\sigma}$ is the effective stress tensor, N the total number of segments, dt the time step, dl the segment length, $\boldsymbol{f}^{PK}$ the Peach-Köhler force and $\boldsymbol{v}$ the velocity.

In chapter 2 it was learned that a dislocation moving on the glide plane with normal $\hat{\boldsymbol{n}}$ produces a relative displacement over the swept area dA given by the Burgers vector $\boldsymbol{b}$. It can be inferred that the relative displacement caused by the dislocation motion introduces a plastic strain on the microstructure proportional to the swept area (Bulatov and Cai, 2006):

$$d\epsilon_{ij}^p = \frac{b_i n_j + b_j n_i}{2\Omega} dA \quad i, j = 1, 2, 3. \tag{5.4}$$

where Ω is the total volume of the material. Consider a dislocation segment defined by two nodes with initial positions $\boldsymbol{x}_1^i$ and $\boldsymbol{x}_2^i$ ending at final positions $\boldsymbol{x}_1^f$ and $\boldsymbol{x}_2^f$ after a simulation step (see figure 5.1). The incremental area swept out by the segment after a simulation step can be expressed in terms of the nodes' positions as follows:

$$\boldsymbol{dA} = \frac{1}{2}(\boldsymbol{x}_2^f - \boldsymbol{x}_1^i) \times (\boldsymbol{x}_1^f - \boldsymbol{x}_2^i) = dA\hat{\boldsymbol{n}} \tag{5.5}$$

By virtue of the superposition principle, the addition of all segment's contributions gives the total plastic strain increment at a given simulation step t. Thus, the plastic strain after at time $t + \Delta t$ can be obtained by adding the new plastic strain increment generated as a result of the dislocation motion:

$$\boldsymbol{\epsilon}^p(t+\Delta t) = \boldsymbol{\epsilon}^p(t) + \boldsymbol{d\epsilon}^p(t+\Delta t) \tag{5.6}$$

5.1.2 Cross-slip probability

Atomistic simulations have been used to estimate the average waiting time for a single cross-slip process to occur. The reciprocal of said average waiting time is known as the cross-slip rate Γ, which multiplied by an specified time step Δt gives the probability P that a single cross-slip event occurs at the end of said time window:

$$P = \Gamma \Delta t \tag{5.7}$$

Following the cross-slip theory presented in chapter 4, the rate equation implemented in the NuMoDis code (Drouet et al., 2014) was proposed by Esteban-Manzanares et al. (2020):

$$\Gamma = \nu \frac{L}{L_n} \exp\left(-\frac{\Delta H}{k_b T}\left[1 - \frac{T}{T_m}\right]\right) \tag{5.8}$$

where $\nu = 10^{11}$ Hz is the fundamental frequency (Sobie et al., 2017), ΔH the activation enthalpy of cross-slip, k_b the Boltzmann constant, T the absolute temperature, T_m the melting temperature, L the screw-dislocation length and L_n the nucleation length of cross-slip (Malka-Markovitz and Mordehai, 2018):

$$L_n = \beta \sqrt{\frac{T_p d_0}{2\gamma}} \tag{5.9}$$

where

$$\beta = \frac{1}{1 + \frac{\sqrt{3}b}{6\gamma}\sigma_E}, \qquad T_p = \frac{\alpha \mu b^2}{2}, \quad d_0 = \frac{\mu b^2}{24\pi\gamma}\frac{2-3\nu}{1-\nu} \tag{5.10}$$

γ being the intrinsic SF energy, σ_E the Escaig stress, α the line-energy parameter and ν the Poisson's ratio.

The activation enthalpy was calculated using the general expression developed by Malka-Markovitz and Mordehai (2019) based on the LT model presented in chapter 3:

$$\frac{\Delta H(\sigma)}{\Delta E_0} = \frac{\beta^g}{2} + \left(\frac{\beta^{cs}}{2}\right)\tanh(l_c) - \left(\frac{\beta^{cs}}{2}\right)\left[\frac{2\alpha_L}{1.55} l_c E^* + \frac{\alpha_{Ls}^3}{1.55}\frac{\delta}{\beta^{cs}} l_c^3\right] \tag{5.11}$$

where ΔE_0 is the unstressed energy barrier and $\alpha_L \approx 0.6$ is a scale factor. The superscript g and cs refer to the glide and cross-slip plane, respectively. As discussed

in chapter 4, the critical length l_c can be found by solving the following equation numerically:

$$\frac{1.55}{\cosh^2(l_c)} - \frac{3\alpha_{Ls}^3\delta}{\beta_{cs}} l_c^2 = 2\alpha_{Ls}E^* \tag{5.12}$$

where the E^* and δ functions are given by (Malka-Markovitz and Mordehai, 2018):

$$E^* = \ln\left(\frac{\beta^{cs}}{\beta^p}\right) \quad \text{and} \quad \delta = \frac{1}{6}\left(\frac{b\sigma_S^{cs}}{\gamma}\right)^2 \tag{5.13}$$

5.2 Methodology

According to the presented models, the cross-slip rate and activation enthalpy are expressed as function of the Schmid stress in the glide plane σ_S^g, the Escaig stress in the glide plane σ_E^g, the Schmid stress in the cross-slip plane σ_S^{cs} and the Escaig stress in the cross-slip plane σ_E^{cs}. Similarly to the procedure carried out in chapter 3, the Cartesian coordinate system was rotated such that the $[\overline{111}]$ direction matched with the $\hat{\boldsymbol{z}}$ axis and the Burgers vector $[\bar{1}10]$ with the $\hat{\boldsymbol{x}}$ axis. In said basis, the glide plane $\hat{\boldsymbol{n}}_g$, the cross-slip plane $\hat{\boldsymbol{n}}_{cs}$, the direction of expansion under positive Escaig stress in the glide plane $\hat{\boldsymbol{w}}_g$, the direction of expansion under positive Escaig stress in the cross-slip plane $\hat{\boldsymbol{w}}_{cs}$ and the unitary Burgers vector $\hat{\boldsymbol{b}}$ are given by:

$$\hat{\boldsymbol{n}}_g = [0, 0, 1] \tag{5.14}$$

$$\hat{\boldsymbol{w}}_g = [0, 1, 0] \tag{5.15}$$

$$\hat{\boldsymbol{n}}_{cs} = \left[0, \frac{2\sqrt{2}}{3}, -\frac{1}{3}\right] \tag{5.16}$$

$$\hat{\boldsymbol{w}}_{cs} = \left[0, \frac{1}{3}, \frac{2\sqrt{2}}{3}\right] \tag{5.17}$$

$$\hat{\boldsymbol{b}} = [1, 0, 0] \tag{5.18}$$

as illustrated in figure 5.2. Consider a symmetric stress tensor in the Cartesian basis:

$$\boldsymbol{\sigma} = \begin{pmatrix} \sigma_{xx} & \sigma_{xy} & \sigma_{xz} \\ \sigma_{xy} & \sigma_{yy} & \sigma_{yz} \\ \sigma_{xz} & \sigma_{yz} & \sigma_{zz} \end{pmatrix} \tag{5.19}$$

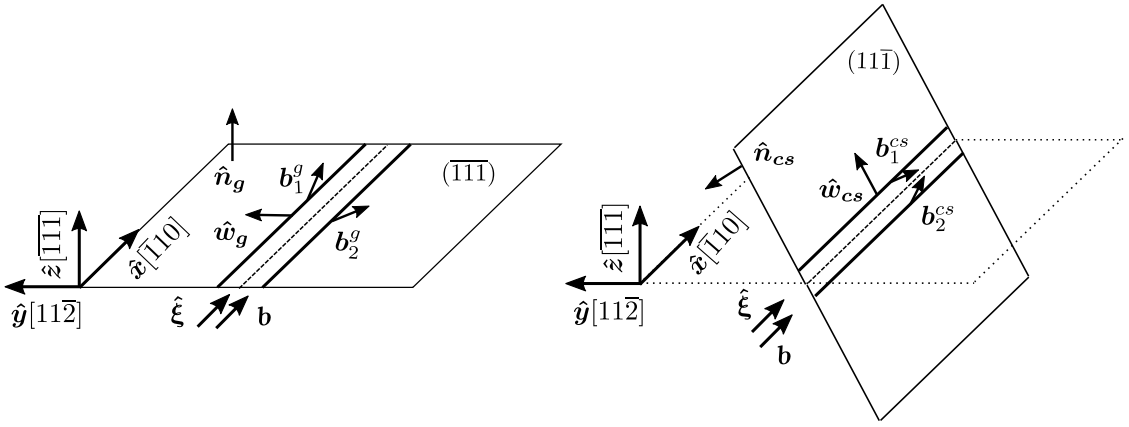

(a) (b)

Figure 5.2: Simulation setup showing loading directions on a $\frac{a}{6}[\overline{1}10]$ dissociated dislocation located in: (a) the glide plane and (b) the cross-slip plane. The dissociated RHS dislocation in the glide plane has partials' Burgers vector $\boldsymbol{b}_1^g = \frac{a_0}{6}[\overline{1}2\overline{1}]$ and $\boldsymbol{b}_2^g = \frac{a_0}{6}[\overline{2}11]$, whereas the dissociated RHS dislocation in the cross-slip plane has partials' Burgers vector $\boldsymbol{b}_1^{cs} = \frac{a_0}{6}[\overline{1}21]$ and $\boldsymbol{b}_2^{cs} = \frac{a_0}{6}[\overline{2}1\overline{1}]$.

Setting $\sigma_{xx} = \sigma_{yy} = 0$, the stress components σ_E^g, σ_S^g, σ_E^{cs} and σ_S^{cs} are given by:

$$\sigma_E^g = \boldsymbol{\sigma} \cdot \hat{\boldsymbol{n}}_g \cdot \hat{\boldsymbol{w}}_g = \sigma_{yz} \tag{5.20}$$

$$\sigma_S^g = \boldsymbol{\sigma} \cdot \hat{\boldsymbol{n}}_g \cdot \hat{\boldsymbol{b}} = \sigma_{xz} \tag{5.21}$$

$$\sigma_E^{cs} = \boldsymbol{\sigma} \cdot \hat{\boldsymbol{n}}_{cs} \cdot \hat{\boldsymbol{w}}_{cs} = \frac{7\sigma_{zy} - 2\sqrt{2}\sigma_{zz}}{9} \tag{5.22}$$

$$\sigma_S^{cs} = \boldsymbol{\sigma} \cdot \hat{\boldsymbol{n}}_{cs} \cdot \hat{\boldsymbol{b}} = \frac{2\sqrt{2}\sigma_{xy} - \sigma_{xz}}{3} \tag{5.23}$$

where $\boldsymbol{\sigma} \cdot \hat{\boldsymbol{n}} \cdot \hat{\boldsymbol{u}}$ is the Schmid's law. Appendix A shows a more detailed calculation of Escaig and Schmid stresses.

Dislocation motion is inertial at both low and high velocities. Said inertia originates from the kinetic energy of the moving core (Tang, 2018). In order to study the cyclic movement of dislocations, the dislocation motion must resonate with the applied stress. Since dislocations are slow respect to the time required for equilibration, the external loading must be increased in a quasi-static manner (Déprés et al., 2004a,b, 2006; Erel et al., 2017b). The effect of frequency on cyclic fatigue simulations using DDD methods has been therefore not considered. Instead, the fatigue regimes are studied according to their range of applied stress amplitudes. In the

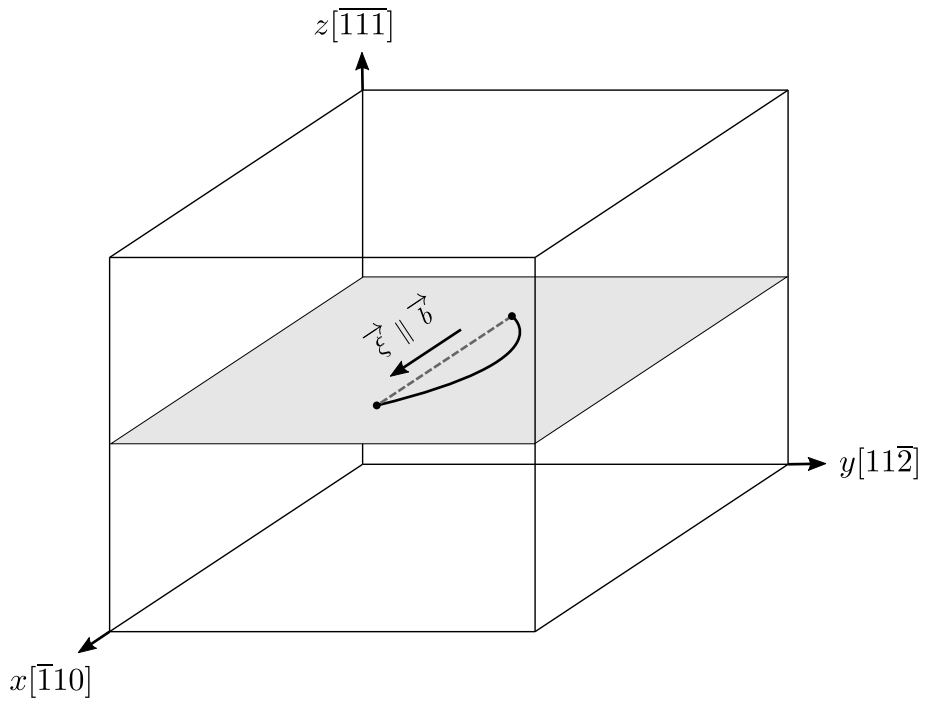

Figure 5.3: Perfect right-handed screw dislocation of length equal to 10,000 Å contained on the $(\overline{111})$ plane. Its Burgers vector and line orientation are parallel to the $[\overline{1}10]$ direction.

present simulations, the time step was set such that the displacement of segments did not exceed 10 nm per step, which resulted in a time step with values between 0.1 and 1 ns for the present simulations. A pure Schmid stress was applied on the glide plane to set the maximum stress amplitude. The applied load was slowly increased at each simulation step once the dislocation reached quasi-static equilibrium with the external load. For this purpose, the applied stress tensor was multiplied by a sine wave of sufficiently large period:

$$\boldsymbol{\sigma}^{cyc} = \sin\left(\frac{2\pi n}{N}\right)\boldsymbol{\sigma} \tag{5.24}$$

where n is the current simulation step and N is the number of steps per cycle. For the particular DDD simulations described in this work, it was found that $N = 40,000$ steps was a sufficiently long period. When a much smaller N was used, the external loading was faster than the inertial motion. In that case, the dislocation was not able to complete the cycle at simulation step $n = N$.

The cross-slip mechanism in the present simulations was modeled using the kinetic Monte Carlo method. Every simulation step, the screw chains were identified. If the angle between its Burgers vector and the line direction was smaller than ten degrees, the dislocation was considered to be screw. A random number between zero

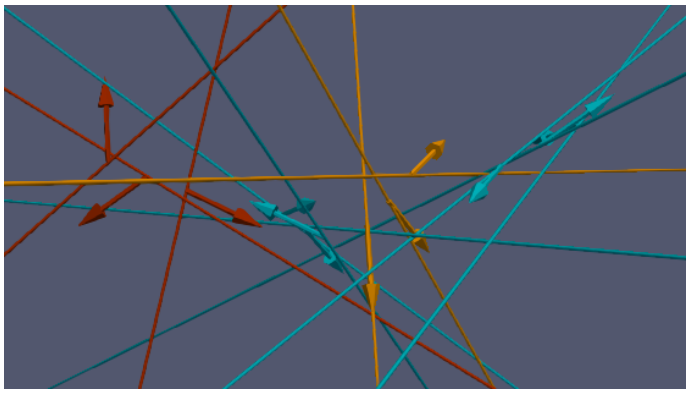

Figure 5.4: Arrangement of twelve dislocations corresponding to each glide system of the FCC structure. Solid arrows denote the Burgers vectors.

and one was generated for each screw chain. The associated cross-slip probability per time step was calculated using equation 5.7. If the cross-slip probability was smaller than the random number, the glide plane of the screw dislocation was changed to its corresponding deviated plane, otherwise, the glide plane of the dislocation remained unchanged.

Single dislocation case

The effect of cross-slip during cyclic fatigue in FCC copper was studied using a perfect screw Frank-Read source. The separation between its pinning points was 10,000 Å (see figure 5.3). The simulation box was 5×10^4 Å wide, 5×10^4 Å deep and 4×10^6 Å high with fixed boundary conditions. The temperature used to calculate the cross-slip rate of screw segments was set to 400 K. As a consequence of the prohibitively high unstressed energy barrier, cross-slip events of isolated dislocations are extremely unlikely to occur. Considering for example a dislocation of length 10,000 Å in copper, the cross-slip probability at room temperature is proportional to 10^{-21}. A pure Schmid stress driving the cyclic motion was not sufficient to trigger any cross-slip events. In order to further decrease the activation enthalpy of cross-slip, a compressive Escaig can be added to the pure Schmid stress that drives the cyclic motion. The present DDD simulations showed that to trigger cross-slip events during one cycle, it was sufficient to add a compressive Escaig stress of 300 MPa to the pure Schmid stress acting on the glide plane. The corresponding dissipated energy per cycle was obtained for a large range of applied Schmid stress amplitudes between 20 and 90 MPa. The dissipated energy per cycle at the pure Schmid stress when no cross-slip occurs was also obtained as a reference. The dissipated energy per cycle was calculated using equation 5.3 in both cases.

Property	Symbol	Value
Unstressed energy barrier	ΔE_0	1.9 eV (Longsworth and Fivel, 2021a)
Line-energy parameter	α	0.3 (Longsworth and Fivel, 2021b)
Lattice parameter	a_0	3.61 Å (Davey, 1925)
Length of Burgers vector	b	$a_0/\sqrt{2}$ (Kittel and McEuen, 2018)
Intrinsic SF energy	γ	42 mJ/m^2 (Bonneville and Escaig, 1979)
Shear modulus	μ	54.6 GPa (Schmauder and Mishnaevsky, 2008)
Poisson's ratio	ν	0.342 (Bradfield and Puesey, 1953)
Melting temperature	T_m	1358 K (Mangum et al., 2001)
Viscous drag coefficient	B	1.5 $\times 10^{-5}$ Pa-s (Philibert, 1979)

Table 5.1: Parameter values for FCC copper used in the DDD simulations.

Multiple dislocations case

The effect of cross-slip during VHCF was simulated using twelve dislocations associated to each gliding system of the FCC structure. Every dislocation was pinned at its ends. All dislocations had an initial length of 10,000 Å. The simulation box was 5×10^4 Å wide, 5×10^4 Å deep and 4×10^6 Å high with fixed boundary conditions. The temperature used to calculate the cross-slip rate of screw segments was equal to 400 K. In FCC copper, the VHCF regime corresponds to the range of stress amplitudes between 3 and 26 MPa (Mughrabi, 1978). In order to study the VHCF regime of FCC copper, a pure Schmid stress of 20 MPa was applied to the glide system $[\bar{1}10](\overline{111})$. The loading tensor was attenuated by the sine function to simulate the cyclic fatigue as shown in equation 5.24. A single perfect right-handed screw was placed in the activated system. The angle between the Burgers vector and line direction of the remaining dislocations was arbitrarily set, with initial values varying between 0 and 126 degrees (see figure 5.4). The center of every dislocation was also randomly assigned. However, the maximum separation between the center of the dislocation in the activated system and the center of the remaining dislocations was 45 Angstroms. Sufficiently strong internal stresses on the screw dislocation were generated by the remaining dislocations. In contrast to the simulations of an isolated screw dislocation, an additional compressive Escaig stress was not necessary to trigger cross-slip events. In the present simulations, the dislocation density during the firsts cycles of the VHCF was computed. The dislocation density obtained with the disabled cross-slip feature was also shown as a reference.

The elastic constants of FCC copper used in the DDD simulations are shown in table 5.1.

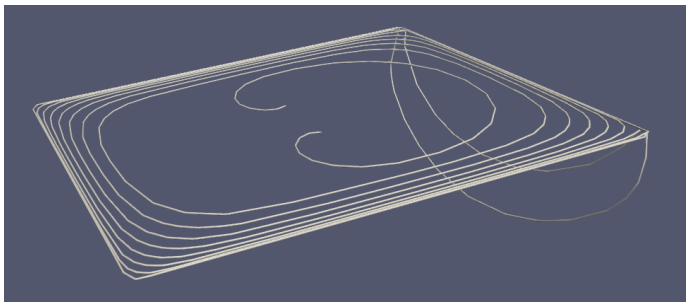

Figure 5.5: Cross-slip at the crystal boundary due to a dislocation pile-up.

5.3 Results and discussion

5.3.1 Effect of cross-slip on the dislocation density

Figure 5.6 (A) shows density evolution of single perfect screw Frank-Read source during the firsts five fatigue cycles. The green curve shows the dislocation density obtained when a compressive Escaig stress of 300 MPa is applied in the glide plane to trigger the cross-slip events, whereas the green curve represents the dislocation density obtained at zero additional Escaig stress. In both cases, a pure Schmid stress of approximately 40 MPa was applied in the glide plane to drive the cyclic motion. At sufficiently low applied stress, the dislocation remained close to its equilibrium position. By increasing the applied stress, the Frank-Read source gets activated. As a consequence, an increasing number of dislocation loops started to reach the crystal boundaries. When the maximum stress was applied, the dislocation loops had zero velocity. A pile-up of screw dislocations was formed at the boundary side which is parallel to the dislocation source as shown in figure 5.5. Said pile-up generated internal Schmid stresses on the deviated plane. In the case where an additional compressive Escaig of 300 MPa was applied, the activation enthalpy decreased sufficiently and some screw dislocations within the pile-up could cross-slip. However, the cross-slipped screws got pulled back to the glide plane immediately after the applied stress started to decrease. For that reason, the dislocation density was only slightly higher for a short period of time when an additional compressive Escaig was applied. It can be concluded that the effect of cross-slip on an isolated dislocation was negligible due to the absence of irreversibility during the cycling.

Figure 5.6 (B) shows the effect of cross-slip on the dislocation density evolution of twelve dislocations during firsts cycles of the VHCF regime corresponding to low stress amplitudes. The green curve represents the dislocation density obtained with the cross-slip feature enabled in the code, whereas the blue curve represents the dislocation density obtained with the cross-slip feature disabled. The vertical lines indicate the instants at which cross-slip events occur in the corresponding simula-

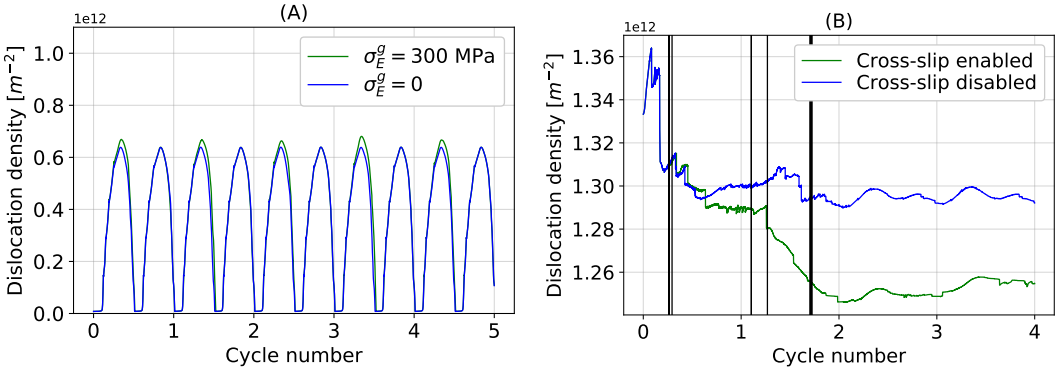

Figure 5.6: Effect of cross-slip on the dislocation density evolution during the firsts fatigue cycles for: (A) a perfect screw Frank-Read source and (B) twelve dislocations with an arbitrary angle between their Burgers vector and line direction.

tion. During the first cycle, the density abruptly decreased due to junction zipping before the first cross-slip event occurs. For the particular dislocation network used in the present simulations, the density obtained with the cross-slip feature enabled decreased further with respect to the dislocation density simulated with the cross-slip feature disabled. At certain parts of the fatigue cycles, the dislocation structure generated strong compressive Escaig stresses near the center of the screw dislocation located on the activated system, in addition to sufficiently large Schmid stresses on the corresponding deviated plane. As a consequence, the screw dislocation moved back and forth between the glide plane and its corresponding cross-slip plane, releasing the strong internal stresses near the center of the dislocations. It can be concluded that the cross-slip mechanism can have a significant effect on the dislocation density evolution even at small applied stress amplitudes.

5.3.2 Effect of cross-slip on the dissipated energy

Figure 5.7 shows the dissipated energy per cycle of an isolated screw dislocation for a large range of applied Schmid stress amplitudes between 20 and 90 MPa. As earlier discussed on section 5.2, cross-slip events could be triggered by adding a compressive Escaig stress of 300 MPa to the pure Schmid stress acting on the glide plane. The green curve shows the dissipated energy per cycle obtained when a compressive Escaig stress of 300 MPa is applied on the glide plane to trigger the cross-slip events, whereas the green curve represents the dissipated energy per cycle at zero additional Escaig stress. For applied stress amplitudes smaller than 40 MPa, the Frank-Read source remains deactivated. As a consequence, the dissipated energy per cycle was the same regardless of the additional compressive Escaig stress. For applied stress amplitudes larger than 40 MPa, the Frank-Read source gets activated

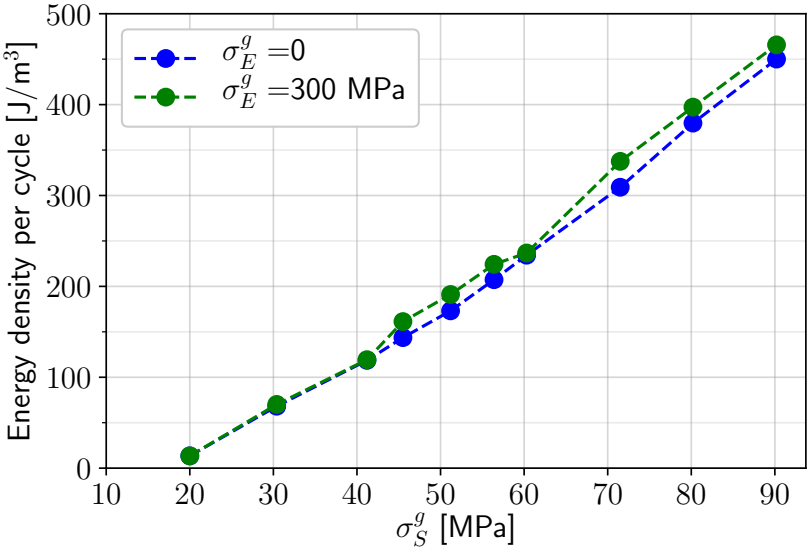

Figure 5.7: Dissipated energy per cycle of a perfect screw Frank-Read source. The abscissa axis represents the pure Schmid stress acting on the glide plane, which corresponds to the applied stress amplitude.

and the dislocation loops generated start to pile up at the crystal boundary. As mentioned on section 5.3.1, the cross-slip events occur at the box sides which are parallel to the dislocation source. However, the cross-slipped screws are pulled back to the glide plane immediately after the applied stress reaches its maximum value. For that reason, the dissipated energy per cycle does not significantly increase due to the cross-slip events. In agreement with the results of section 5.3.1, it can be concluded that the effect of cross-slip on an isolated dislocation is negligible.

5.4 Summary and conclusions

In the present chapter, the effect of cross-slip during cyclic fatigue on two different microstructural defects on FCC copper was studied. For simplicity, the effect of cross-slip during cyclic fatigue on a perfect screw Frank-Read source was analyzed first. In order to consider a more complex case, the effect of cross-slip on a network of twelve dislocations with an arbitrary angle between their Burgers vector and line direction was also studied. For the purpose of characterizing said microstructural defects, the dislocation density evolution during the firsts fatigue cycles was obtained. Moreover, the dissipated energy per cycle was used to quantify the extend of plastic deformation due to cross-slip of a perfect screw Frank-Read source. It was found that although the cross-slip probability of an isolated screw dislocation source is negligible at 400 K, the cross-slip probability could be significantly increased by

adding a compressive Escaig stress of 300 MPa to the pure Schmid stress acting on the glide plane. As a result, some dislocations could cross-slip at the crystal boundaries due to the internal Schmid stress arising from the dislocation pile-up. However, the cross-slipped screws were pulled back to the glide plane immediately after the applied stress reached its maximum value, such that there was no dislocation storage during the cycling. It follows that for the case of an isolated dislocation, the cross-slip mechanism did not cause any irreversible change on the microstructure. It can be concluded that the effect of cross-slip on an isolated dislocation was negligible. In contrast, the cross-slip mechanism produced irreversible changes in the case of a dislocation network. Due to the small distance of less than 45 Å between the centers of the dislocations, a pure Schmid stress of 20 MPa was sufficient to trigger the cross-slip events without the need to add any external Escaig stress. For that reason, cross-slip plays a significant role on the microstructure evolution even in the firsts cycles of the VHCF regime.

Chapter 6

Conclusions and future work

As a way to conclude the present manuscript, a short overview of each chapter is provided. With the expectation of simulating many cycles of the VHCF regime in the future, a time-coarsening algorithm and some possible extensions of the presented work are finally given in the last section.

Conclusions

Theory of dislocations

Chapter 2 reviewed the fundamental concepts necessary to understand the cross-slip mechanism, such as the physical dissociation of perfect dislocations on the FCC structure, the description of Escaig stresses that affect the dissociation separation between the partial dislocations and the definition of Schmid stresses driving the dislocation motion perpendicularly to the Burgers vector. In order to clarify the effect of Escaig and Schmid stresses on a general dissociated dislocation, the direction of motion under the influence of stress was carefully discussed for each dislocation type.

The activation enthalpy of cross-slip

Chapter 3 presented a study of the cross-slip energetics in FCC copper using DDD simulations. In agreement with the work of Ramírez et al. (2012), the constriction energy required for cross-slip initiation was 0.7 eV. A negligible effect on the constriction energy was obtained for applied compressive Escaig stresses in the range between 50 to 250 MPa. In further agreement with the DDD simulations of Ramírez et al. (2012), the unstressed energy barrier of cross-slip was found to be 1.9 eV. As a second step, the effect of stress on the activation enthalpy of cross-slip was estimated for a wide range of Escaig and Schmid stresses. In qualitative agreement with the atomistic simulations performed by Kang et al. (2014), it was confirmed that

both stress components have a comparable effect in reducing the energy barrier. By applying a compressive Escaig stress on the glide plane, the energy barrier was most drastically reduced up to 50% of its value. Two modern LT models of cross-slip were used as references to compare with the DDD simulation results, namely, the numerical LT model of Kang et al. (2014) and the general expression for the activation enthalpy developed by Malka-Markovitz and Mordehai (2019). The model of Kang et al. (2014) was calibrated by tweaking the line-energy parameter α to match the unstressed energy barrier obtained from DDD simulations, whereas the model of Malka-Markovitz and Mordehai (2019) was simply calibrated by using the same unstressed energy barrier of 1.9 eV as obtained from DDD simulations. It was concluded that both theoretical models were in good quantitative agrement with the DDD simulation results. For that reason, the model of Malka-Markovitz and Mordehai (2019) could be reliably employed on DDD codes to calculate the activation enthalpy of screw segments.

As a final remark, the core-width parameter value of the non-singular theory of Cai et al. (2006) used in DDD simulations must be carefully deduced from the models of Schöck (2010) as suggested by Ramírez et al. (2012). Otherwise, neither the constriction energies nor the energy barriers could be correctly estimated using DDD simulations.

The content of this chapter was published in the Journal of Mechanics and Physics of Solids (Longsworth and Fivel, 2021a).

The rate of cross-slip

Based on the quantitative consistency between the DDD simulation results and the LT models demonstrated in chapter 3, a new DDD methodology employing the analytical model of Malka-Markovitz and Mordehai (2019) to simulate cross-slip was proposed in chapter 4. To calibrate their model, the unstressed energy barrier was set to 1.9 eV as obtained with the DDD simulations of FCC copper (Longsworth and Fivel, 2021a). In contrast with many previous cross-slip models used in DDD simulations, no scaling factors nor fitting parameters were required to reproduce quantitative atomistic results. The rate of cross-slip was calculated using the atomistic-based model proposed by Esteban-Manzanares et al. (2020). Besides the activation enthalpy, the nucleation length was the only other stress-dependent parameter required to compute the cross-slip rate. Said nucleation length was inferred from the LT model of cross-slip developed by Malka-Markovitz and Mordehai (2018). The only free variable of the nucleation length was the line-energy parameter, which has typical values in the range between 0.1 and 0.6 (Kang et al., 2014; Longsworth and Fivel, 2021a). For that reason, an average line-energy value

of 0.3 was used in chapter 4 to compute the nucleation length of cross-slip.

There are not many quantitative studies of the cross-slip rate in the literature. A small number of rate estimates have been obtained using atomistic simulations. In particular, Vegge et al. (2000) and Oren et al. (2017) provided some estimates of the cross-slip rate in FCC copper, which have been used as a standard. Their activation enthalpies and cross-slip rates were both in good quantitative agreement with the presented DDD simulation results. It was concluded that the proposed cross-slip methodology can be reliably implemented on any DDD code to simulate the physics of fatigue in metals.

The content of this chapter was published in the Journal of Mechanics and Physics of Solids (Longsworth and Fivel, 2021b).

The effect of cross-slip during cyclic fatigue

Chapter 5 showed some preliminary applications of the recently benchmarked cross-slip modeling described in chapter 4 to cyclic fatigue simulations. Since the external loading was increased in a quasi-static manner, the effect of frequency on the DDD simulations was not considered. Instead, the fatigue regimes were studied according to their range of applied stress amplitudes. The concrete objective of chapter 5 was to study the effect of cross-slip on two different microstructural defects on FCC copper was studied, namely on one isolated dislocation, and on twelve dislocations with an arbitrary angle between their Burgers vector and line direction. It was found that cross-slip on an isolated dislocation could be triggered at the crystal boundary by applying an additional compressive Escaig stress to the cyclic loading. Under this condition, cross-slip events caused the screw segments to bow-out at the crystal boundary due to the Schmid stress arising from the dislocation pile-up. However, the cross-slip mechanism did not cause any irreversible change on the microstructure because cross-slipped screws were immediately pulled back to the glide plane after the applied Schmid stress reached its maximum value. In strong contrast, the pure Schmid stress driving the cyclic motion was sufficient to trigger cross-slip events on the dislocation network. It can be concluded that cross-slip plays a significant role on the microstructure evolution by allowing dislocations on different planes to irreversibly react with each other.

The content of this chapter was presented at the 8th international conference on very high cycle fatigue (VHCF8) on July 2021.

Future work

Time-coarsening algorithm for VHCF simulations

DDD methods have been adequate to study the firsts cycles of the LCF regime. They can only simulate a few tens of fatigue cycles due to the computational limitations imposed by the fine description of the microstructure. At the time of writing, no attempts to simulate the other fatigue regimes have been found in the literature. Since the VHCF regime corresponds to very small applied stress amplitudes, cross-slip of screw dislocations provoking cyclic irreversibilities are far more infrequent than in the LCF regime, which implies that a significant accumulation of microstructural defects would occur at a much larger number of cycles. Jump-in-cycle techniques can be coupled with the kinetic Monte Carlo model of cross-slip to skip the fatigue cycles where no cyclic irreversibilities occur, enabling to predict the number of cycles to failure in the VHCF regime occurring at a much larger time scale. The present section proposes a new time-coarsening algorithm based on the Monte Carlo method to simulate the VHCF regime after many cycles.

The two most prominent Monte Carlo (MC) methods are the Metropolis Monte Carlo (MMC) and the kinetic Monte Carlo (kMC) methods. The MMC method can be used to improve the spatial-sampling efficiency in simulations (Longsworth, 2017; Zhang and Yang, 1993; Chen and Roux, 2015). It generates configurations according to a prescribed probability distribution. Since the time progression leading to an equilibrium state is stochastic, there is no information about dynamics of the system nor on how fast the equilibrium state is reached. For problems in which the time increments related to the kinetics of the system are important, the kMC method is the appropriate alternative to take into consideration the physical time of simulations. The transition probability in the MMC method relies on the time-independent activation energy between two states, whereas the transition probability in the kMC method is calculated using a time-dependent rate equation Γ. For single processes such as the cross-slip of screw dislocations, the reciprocal of the rate is equal to the average time required for the process to occur. The probability P that such transition occurs within an specified time step Δt is given by:

$$P = \Gamma \Delta t \tag{6.1}$$

Recall that NuMoDis (Drouet et al., 2014) employs the atomistic-based cross-slip rate developed by Esteban-Manzanares et al. (2020):

$$\Gamma = \nu \left(\frac{L}{L_n} \right) e^{-\frac{\Delta H}{k_b T}\left(1-\frac{T}{T_m}\right)} \tag{6.2}$$

Variable	Value
$\nu[s^{-1}]$	10^{11} (Sobie et al., 2017)
T_m [K]	1357 (Mangum et al., 2001)
k_b [eV/K]	8.6×10^{-5}
T [K]	300
ΔH [eV]	0.4
L [Å]	10000
L_n [Å]	15

Table 6.1: Example values associated to the fastest cross-slip process; ν is the fundamental frequency, T_m the melting temperature, k_b the Boltzmann constant, T the absolute temperature, ΔH the activation enthalpy, L the screw-dislocation length and L_n the nucleation length of cross-slip, which typically varies between 10 and 30 Å.

where ν is the fundamental frequency, L the screw-dislocation length, L_n the nucleation length of cross-slip, k_b the Boltzmann constant, T_m the melting temperature, T the absolute temperature and ΔH the activation enthalpy, which is calculated using the general expression developed by Malka-Markovitz and Mordehai (2019) based on the LT model. According to the kMC method, a random number between zero and one is generated at the beginning of each simulation step. If said random number is larger than the cross-slip probability of a given screw segment, its glide plane is changed to the corresponding deviated plane, or else the glide plane remains unchanged.

There are several schemes to determine the time step (Cao, 1994; Voter, 1986; Dawnkaski et al., 1995b,a). By simply choosing a constant time step for the whole simulation (Dawnkaski et al., 1995a) , the time step should be smaller than the fastest process. In the context of discrete dislocation dynamics simulations, examples of physical processes are the glide of dislocations over a given distance, the cross-slip of a screw segment having a certain length, the annihilation between two dislocations of opposite signs, the process of junction formation, among others. Assuming that the screw segment most likely to cross-slip at all times has the parameter values indicated in table 6.1, the evaluation of equation 6.2 using said parameter values gives the maximum possible rate:

$$\Gamma_{max} = 3.8 \times 10^{8} \text{ Hz} \tag{6.3}$$

Setting the maximum cross-slip probability to the arbitrary value of 0.5, the time step can be determined using equation 6.1:

ΔH [eV]	P
1.9	1.1×10^{-20}
1.6	9.1×10^{-17}
1.2	1.6×10^{-11}
0.8	2.8×10^{-6}
0.6	1.2×10^{-3}
0.4	0.5

Table 6.2: Cross-slip probability P as function of the activation enthalpy ΔH obtained using the parameter values shown in table 6.1 and the time step value $\Delta t = 1.3$ ns.

$$\Delta t = \frac{0.5}{3.8 \times 10^{8}} = 1.3 \text{ ns} \tag{6.4}$$

The number of cross-slip events at the applied stress levels corresponding to the VHCF regime are negligible. Table 6.2 shows the cross-slip probability obtained using the parameter values shown in table 6.1 at different activation enthalpies. For the low stress amplitudes between 3 and 26 MPa corresponding to the VHCF regime of copper (Mughrabi, 1978), the unstressed energy barrier of 1.9 eV does not significantly decrease. As discussed in chapter 3, the energy barrier of copper decreases on average only 0.1 eV at the maximum stress amplitude of the VHCF regime, which corresponds to a negligible cross-slip probability in the range between 10^{-18} and 10^{-20} for isolated screw dislocations. Assuming that cross-slip is the main mechanism inducing cyclic irreversibilities in the microstructure, the simulations steps where cross-slip trials are rejected can be skipped while increasing the simulation time. Following the work of Déprés et al. (2004a), the number of cycles to failure could be estimated by assuming a critical extrusion size, which represents the initiation of a micro-crack at the crystal surface leading to fatigue failure. The time-coarsening procedure consists of three phases that repeat until the prescribed number of simulation steps is completed, namely the Learning phase where the information during a full cycle is stored, the Stall phase where the loaded information is repeatedly tested until a cross-slip event is detected and the Stabilization phase where the system is evolved until cyclic behavior is obtained after the cross-slip execution. The following sections address each phase independently and present a diagram depicting their interconnection.

Learning phase

When the velocity, position and force acting on each node has been stored for each step of a complete cycle, no more computation using discrete dislocation dynamics

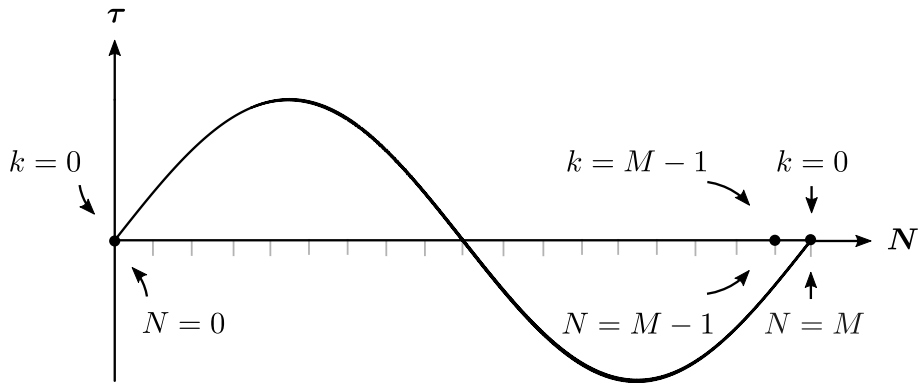

Figure 6.1: Stress cycle applied τ as function of the simulation step N. The loading stage corresponds to a specific part of the cycle characterized by $k = N\%M$.

is further necessary until a cross-slip event occurs: the simulation is predictable for every future step due to the cyclic motion driven by the external loading. In the Learning phase all information about the system is registered during a full loading cycle where all cross-slip events have been rejected. The fast-forwarding algorithm starts in the Learning phase. Each temporal stage of the loading cycle must be indexed such that for a constant number of simulation steps M per cycle, the first stage is characterized by $k = 0$ and the last one by $k = M-1$. The loading stage after N simulation steps can be calculated as $k = N\%M$, where the symbol % refers to the modulus operator (see figure 6.1). Notice that although the Learning phase is limited to the storage of information during M simulation steps, the loading indexation will be essential to account for the real time in the other two phases. Once all physical parameters of the system have been computed and the cross-slip probability of each screw segment P has been calculated, all the obtained information is stored in arrays characterized by the loading index k. Due to the reduced probability of two cross-slip events occurring at the same time, it is assumed that only one cross-slip event occurs per simulation step. In order to select a screw segment with homogeneous probability, an integer random number R_1 between 0 and $S-1$ is generated, where S is the number of screw segments detected at the loading stage k. Assuming that the cross-slip probability of the selected screw segment is $P = P[R_1]$, a rational random number R_2 between 0 and 1 must be generated to implement the MC method. If the cross-slip event is accepted, the Learning phase is immediately terminated to execute the cross-slip event in the Stabilization phase, whereas if the transition is rejected, the total system is simply evolved and the time step is increased. The same process must be repeated until the Learning phase is completed. The configuration obtained after M simulation steps must be compared with the first stored state to confirm that the simulation is cyclic. Once the Learning phase has been completed, no further DDD simulations are generated. The program enters directly into the

Stall phase where only MC trials are processed using the information obtained from the Learning phase. Summarizing:

1. Determine the loading stage using $k = N\%M$.

2. Store the complete simulation state, such as nodal forces, positions and velocities for all the dislocation segments.

3. Compute all available cross-slip probabilities and store them:

$$\Pi[k] = \{P[0], P[1], ..., P[S-1]\}$$

   where S is the total number of screw segments and $P[i]$ is the cross-slip probability of the ith screw segment.

4. Select a cross-slip candidate with homogeneous probability using an integer random number $R_1 \in \{0, 1, 2, ..., S-1\}$:

$$P = P[R_1]$$

5. Generate a rational random number $R_2 \in (0, 1]$. If $P > R_2$: enter into the Stabilization phase, or else continue to step 6.

6. Update the configuration using DDD and increase the simulation step $N = N + 1$, which implicitly augments the loading stage to $k = k + 1$. If the total number of steps has been completed: terminate the program, or else continue to step 7.

7. Compare the updated configuration after the last loading stage with the first registered state, which occurs when the condition $k = M$ is satisfied. If they are identical: enter into the Stall phase, or else return to step 1.

Stall phase

The successful completion of the Learning phase is followed by the Stall phase, where the number of cross-slip trials is indefinitely increased until one trial is accepted. Since the Stall phase loads the cyclic evolution of the system stored during the Learning phase, the number of simulation steps N in the Stall phase is identified with the number of cross-slip trials. Once the loading stage has been determined using $k = N\%M$, the corresponding probability array Π is loaded. An integer random number R_1 between 0 and $S-1$ is typically required to select an element of the array with homogeneous probability, where S is the number of screw segments detected

at the corresponding loading stage. Assuming that the cross-slip probability of the selected screw segment is $P = P[R_1]$, a rational random number R_2 between 0 and 1 must be generated to implement the MC method. If the cross-slip event is accepted, the Stall phase is immediately terminated to execute the cross-slip event in the Stabilization phase, whereas if the transition is rejected, the number of time steps is increased. No further DDD simulation step is necessary because the hypothetical cross-slip trial has been rejected. The same process is indefinitely repeated until a cross-slip trial is accepted. Summarizing:

1. Determine the loading stage using $k = N\%M$.

2. Load all available cross-slip probabilities at the current loading stage:

$$\Pi[k] = \{P[0], P[1], ..., P[S-1]\}$$

   where S is the total number of screw segments and $P[i]$ is the cross-slip probability of the ith screw segment.

3. Select a cross-slip candidate with homogeneous probability using an integer random number $R_1 \in \{0, 1, 2, ..., S-1\}$:

$$P = P[R_1]$$

4. Generate a rational random number $R_2 \in (0, 1]$. If $P > R_2$: enter into the Stabilization phase, or else continue to step 5.

5. Increase the simulation step $N = N+1$, which implicitly augments the loading stage to $k = k+1$. If the total number of steps has been completed: terminate the program, or else return to step 1.

Stabilization phase

The accepted cross-slip trials generated either during the Learning phase or the Stall phase are executed in the Stabilization phase using the DDD method. A cross-slip event can lead to dislocation reactions that disrupt the cyclic motion of the dislocations during a short period of time. The Stabilization phase comprises a series of DDD simulations steps where the dislocation movement is not cyclical. It starts with the configuration evolution after cross-slip and its corresponding storage on the registry. An integer random number R_1 between 0 and $S-1$ is typically required to select an element of the array with homogeneous probability, where S is the number of screw segments detected at the corresponding loading stage.

Assuming that the cross-slip probability of the selected screw segment is $P = P[R_1]$, a rational random number R_2 between 0 and 1 must be generated to implement the MC method. If the cross-slip event is accepted, the glide plane of the screw segment is changed to its corresponding deviate plane, whereas if the transition is rejected, the total system is updated again and the time step is increased. Since the DDD simulation must be evolved until the configuration is stabilized by the cyclic stress, the updated state must be compared with each past registered state to detect initiation of cyclic behavior. The same process must be repeated until the Stabilization phase is completed. Once an updated state has already been registered, the program enters back into the Learning phase. Summarizing:

1. Execute cross-slip process.
2. Update the configuration using DDD and increase the simulation step. If the total number of steps has been completed: terminate the program, or else continue to step 2.
3. Store the complete simulation state, such as nodal forces, positions and velocities.
4. Compute all available cross-slip probabilities:

$$\Pi = \{P[0], P[1], ..., P[S-1]\}$$

   where S is the total number of screw segments and $P[i]$ is the cross-slip probability of the ith screw segment.
5. Select a cross-slip candidate with homogeneous probability using an integer random number $R_1 \in \{0, 1, 2, ..., S-1\}$:

$$P = P[R_1]$$

6. Generate a rational random number $R_2 \in (0, 1]$. If $P > R_2$: return to step 1, or else continue to step 7.
7. Update the configuration using DDD and increase the simulation step. If the total number of steps has been completed: terminate the program, or else continue to step 8.
8. Compare the updated configuration with each past registered state. If the system started to repeat itself: enter into the Learning phase, or else return to step 3.

The complete algorithm is graphically synthesized in figure 6.2.

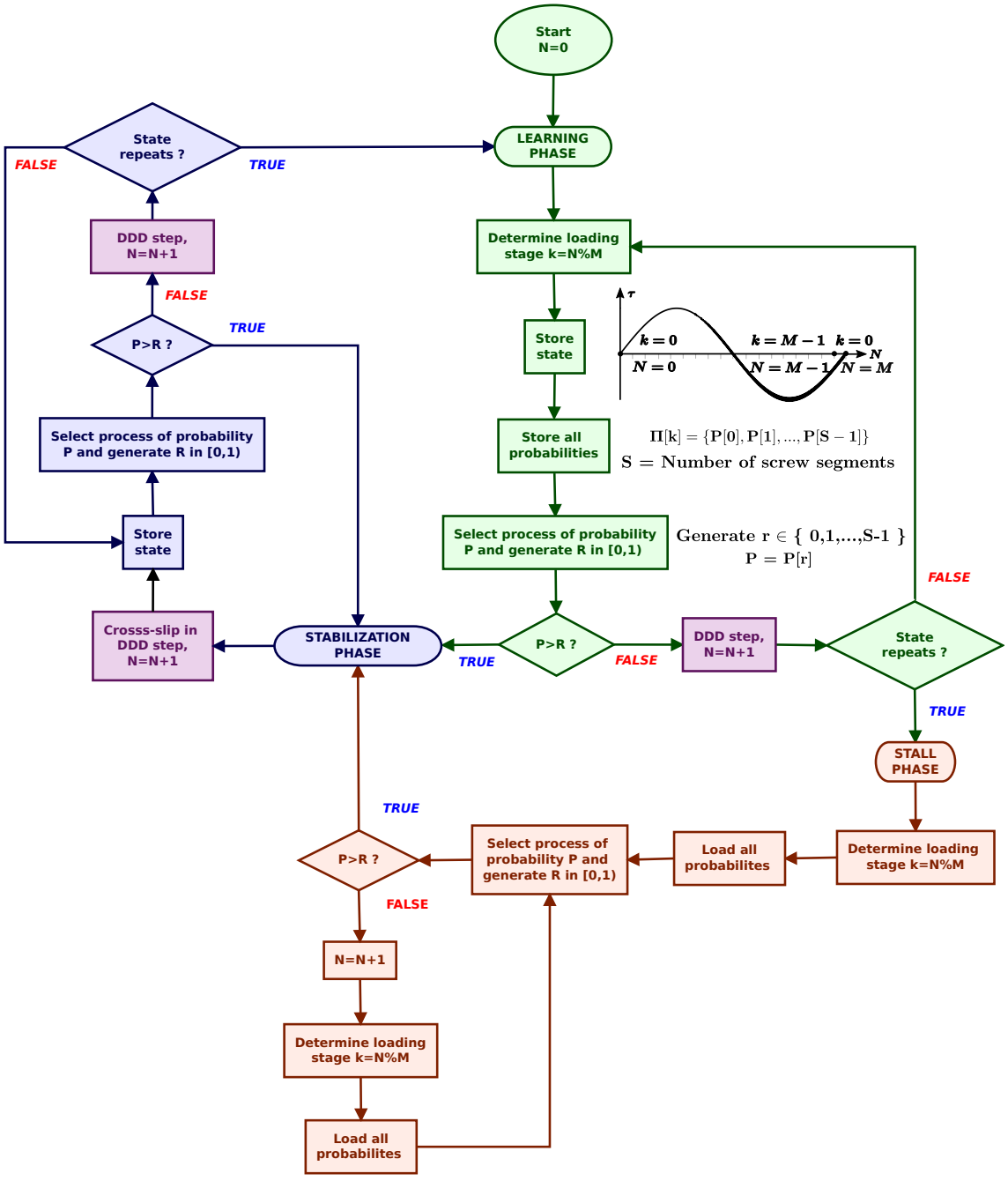

Figure 6.2: Simulation scheme to be implemented in the DDD code to model the microstructure evolution in the VHCF regime.

Virtual X-ray diffraction patterns

In chapter 1 it was learned that microsecond time-resolved X-ray diffraction during ultrasonic loading has been recently used to determinate the fatigue behavior of materials (Ors et al., 2019). Important micromechanical information can be deduced from the diffraction data, such as the lattice elastic strain and the longitudinal normal stress. By implementing the previously described time-coarsening algorithm and the computational method proposed by Bertin and Cai (2018), the virtual X-ray diffraction patterns from discrete dislocation structures can be obtained as function of time using DDD simulations, which would serve to compute the temporal evolution of the dissipated and stored energy in the VHCF regime. By employing the temperature value obtained using infrared thermography (Wagner et al., 2010) in a DDD code, a good agreement with the experimental studies is expected to be achieved. It can be concluded that the successful implementation of both methodologies in a DDD code would enable the direct comparison between numerical simulations and experimental techniques to further study the VHCF regime.

Appendix A

Escaig and Schmid stresses

As discussed in chapter 3, the normalized Burgers vector $\hat{\boldsymbol{b}}$, the unitary normal to the glide plane $\hat{\boldsymbol{n}}_g$, the Escaig vector on the glide plane $\hat{\boldsymbol{w}}_g$, the unitary normal to the cross-slip plane $\hat{\boldsymbol{n}}_{cs}$ and the Escaig vector on the cross-slip plane $\hat{\boldsymbol{w}}_{cs}$ are given by:

$$\hat{\boldsymbol{b}} = \begin{pmatrix} \overline{1} \\ 1 \\ 0 \end{pmatrix} \quad \hat{\boldsymbol{n}}_g = \begin{pmatrix} \overline{1} \\ \overline{1} \\ \overline{1} \end{pmatrix} \quad \hat{\boldsymbol{n}}_{cs} = \begin{pmatrix} 1 \\ 1 \\ \overline{1} \end{pmatrix} \quad \hat{\boldsymbol{w}}_g = \begin{pmatrix} 1 \\ 1 \\ \overline{2} \end{pmatrix} \quad \hat{\boldsymbol{w}}_{cs} = \begin{pmatrix} \overline{1} \\ \overline{1} \\ \overline{2} \end{pmatrix} \tag{A.1}$$

Recall that the rotation of ϕ about the initial $\hat{\boldsymbol{z}}$ axis, followed by a second rotation of θ about the rotated $\hat{\boldsymbol{x}}$ axis and finishing with a third rotation of ψ about the rotated $\hat{\boldsymbol{z}}$ can be represented by the following matrix:

$$R = R_{z''}(\psi) R_{x'}(\theta) R_z(\phi) \tag{A.2}$$

$$= \begin{pmatrix} C_\phi C_\psi - S_\phi S_\theta S_\psi & -C_\phi S_\psi - S_\phi C_\theta C_\psi & S_\phi S_\theta \\ S_\phi C_\psi + C_\phi C_\theta S_\psi & -S_\phi S_\psi + C_\phi C_\theta C_\psi & -C_\phi S_\theta \\ S_\theta S_\psi & S_\theta C_\psi & C_\theta \end{pmatrix} \tag{A.3}$$

where C and S are the shorthanded terms for cosine and sine.

The transformation matrix that rotates the $[\overline{111}]$ direction to the $\hat{\boldsymbol{z}}$ axis and the Burgers vector $[\overline{1}10]$ with the $\hat{\boldsymbol{x}}$ axis is obtained using the Bunges angles $\psi = 0$, $\theta = -\frac{3\pi}{4}$ and $\phi = \arccos\left(-\frac{1}{\sqrt{3}}\right)$, which gives:

$$R = \begin{pmatrix} -\frac{\sqrt{2}}{2} & \frac{\sqrt{2}}{2} & 0 \\ \frac{\sqrt{6}}{6} & \frac{\sqrt{6}}{6} & -\frac{\sqrt{6}}{3} \\ -\frac{\sqrt{3}}{3} & -\frac{\sqrt{3}}{3} & -\frac{\sqrt{3}}{3} \end{pmatrix} \tag{A.4}$$

One can easily verify that the application of the rotation matrix R to the vectors shown on equation A.1 give:

$$\hat{\boldsymbol{b}}' = \begin{pmatrix} 1 \\ 0 \\ 0 \end{pmatrix} \quad \hat{\boldsymbol{n}}'_g = \begin{pmatrix} 0 \\ 0 \\ 1 \end{pmatrix} \quad \hat{\boldsymbol{n}}'_{cs} = \begin{pmatrix} 0 \\ \frac{2\sqrt{2}}{3} \\ -\frac{1}{3} \end{pmatrix} \quad \hat{\boldsymbol{w}}'_g = \begin{pmatrix} 0 \\ 1 \\ 0 \end{pmatrix} \quad \hat{\boldsymbol{w}}'_{cs} = \begin{pmatrix} 0 \\ \frac{1}{3} \\ \frac{2\sqrt{2}}{3} \end{pmatrix} \tag{A.5}$$

Consider the stress tensor in the previously defined base:

$$\boldsymbol{\sigma} = \begin{pmatrix} \sigma_{xx} & \sigma_{xy} & \sigma_{xz} \\ \sigma_{xy} & \sigma_{yy} & \sigma_{yz} \\ \sigma_{xz} & \sigma_{yz} & \sigma_{zz} \end{pmatrix} \tag{A.6}$$

Then, the stress components are given by:

$$\sigma_S^g = \boldsymbol{\sigma} \cdot \hat{\boldsymbol{n}}'_g \cdot \hat{\boldsymbol{b}}' = \sigma_{xz} \tag{A.7}$$

$$\sigma_E^g = \boldsymbol{\sigma} \cdot \hat{\boldsymbol{n}}'_g \cdot \hat{\boldsymbol{w}}'_g = \sigma_{yz} \tag{A.8}$$

$$\sigma_S^{cs} = \boldsymbol{\sigma} \cdot \hat{\boldsymbol{n}}'_{cs} \cdot \hat{\boldsymbol{b}}' = \frac{2\sqrt{2}\sigma_{xy} - \sigma_{xz}}{3} \tag{A.9}$$

$$\sigma_E^{cs} = \boldsymbol{\sigma} \cdot \hat{\boldsymbol{n}}'_{cs} \cdot \hat{\boldsymbol{w}}'_{cs} = \frac{7\sigma_{zy} + 2\sqrt{2}(\sigma_{yy} - \sigma_{zz})}{9} \tag{A.10}$$

Inverting the system of equations A.7 to A.10 gives the tensor components as function of σ_S^g, σ_E^g, σ_S^{cs} and σ_E^{cs}:

$$\sigma_{xx} = \sigma_{yy} = 0 \tag{A.11}$$

$$\sigma_{zz} = \frac{7\sqrt{2}\sigma_E^g - 9\sqrt{2}\sigma_E^{cs}}{4} \tag{A.12}$$

$$\sigma_{xy} = \frac{\sqrt{2}\sigma_S^g + 3\sqrt{2}\sigma_S^{cs}}{4} \tag{A.13}$$

$$\sigma_{xz} = \sigma_S^g \tag{A.14}$$

$$\sigma_{yz} = \sigma_E^g \tag{A.15}$$

Bibliography

M. Abdel Wahab. Prediction of fatigue thresholds in adhesively bonded joints using damage mechanics and fracture mechanics. *Journal of Adhesion Science and Technology*, 15(7):763–781, 2001. ISSN 01694243. doi: 10.1163/15685610152540830. 14

M. Aliabadi. *The boundary element method, volume 2: applications in solids and structures*, volume 2. John Wiley & Sons, 2002. 16

P. Anderson, J. Hirth, and J. Lothe. *Theory of Dislocations*. Cambridge University Press, 2017. ISBN 9780521864367. URL https://books.google.fr/books?id=LK7DDQAAQBAJ. viii, 22, 23, 24, 25, 26, 42, 47, 81, 82

A. Arsenlis, W. Cai, M. Tang, M. Rhee, T. Oppelstrup, G. Hommes, T. Pierce, and V. Bulatov. Enabling strain hardening simulations with dislocation dynamics. *Modelling and Simulation in Materials Science and Engineering*, 15 (6):553–595, 2007. ISSN 0965-0393. doi: 10.1088/0965-0393/15/6/001. URL https://iopscience.iop.org/article/10.1088/0965-0393/15/6/001. 54

S. Banerjee, N. Ghoniem, G. Lu, and N. Kioussis. Non-singular descriptions of dislocation cores: a hybrid ab initio continuum approach. *Philosophical Magazine*, 87(27):4131–4150, 2007. ISSN 1478-6435. doi: 10.1080/14786430701528739. URL http://www.tandfonline.com/doi/abs/10.1080/14786430701528739. 69

Z. Basinski and S. Basinski. Copper single crystal PSB morphology between 4.2 and 350 K. 37(12):3263–3273, 1989. 10

C. Bathias. There is no infinite fatigue life in metallic materials. *Fatigue & fracture of engineering materials & structures (Print)*, 22(7):559–565, 1999. 3

T. Belytschko and T. Black. Elastic crack growth in finite elements with minimal remeshing. *International Journal for Numerical Methods in Engineering*, 45 (5):601–620, 1999. ISSN 00295981. doi: 10.1002/(SICI)1097-0207(19990620)45:5⟨601::AID-NME598⟩3.0.CO;2-S. 14

N. Bertin and W. Cai. Computation of virtual X-ray diffraction patterns from discrete dislocation structures. *Computational Materials Science*, 146:268–277,

2018. ISSN 09270256. doi: 10.1016/j.commatsci.2018.01.037. URL https://doi.org/10.1016/j.commatsci.2018.01.037. 112

S. Bhamare, T. Eason, S. Spottswood, S. Mannava, V. Vasudevan, and D. Qian. A multi-temporal scale approach to high cycle fatigue simulation. *Computational Mechanics*, 53(2):387–400, 2014. ISSN 01787675. doi: 10.1007/s00466-013-0915-y. vii, 14, 15

T. Billaudeau and Y. Nadot. Support for an environmental effect on fatigue mechanisms in the long life regime. *International Journal of Fatigue*, 26(8):839–847, 2004. ISSN 01421123. doi: 10.1016/j.ijfatigue.2004.01.005. 12, 13

A. Blanche, A. Chrysochoos, N. Ranc, and V. Favier. Dissipation Assessments During Dynamic Very High Cycle Fatigue Tests. *Experimental Mechanics*, 55 (4):699–709, apr 2015. ISSN 0014-4851. doi: 10.1007/s11340-014-9857-3. URL http://link.springer.com/10.1007/s11340-014-9857-3. 6

R. Blotny and J. Kaleta. A method for determining the heat energy of the fatigue process in metals under uniaxial stress. Part 1. Determination of the amount of heat liberated from a fatigue-tested specimen. *International Journal of Fatigue*, 8(1):29–34, 1986. 87

J. Bonneville and B. Escaig. Cross-slipping process and the stress-orientation dependence in pure copper. *Acta Metallurgica*, 27(9):1477–1486, 1979. ISSN 00016160. doi: 10.1016/0001-6160(79)90170-6. URL https://linkinghub.elsevier.com/retrieve/pii/0001616079901706. 61, 80, 96

J. Bonneville, B. Escaig, and J. Martin. A study of cross-slip activation parameters in pure copper. *Acta Metallurgica*, 36(8):1989–2002, 1988. ISSN 00016160. doi: 10.1016/0001-6160(88)90301-X. URL https://linkinghub.elsevier.com/retrieve/pii/000161608890301X. 64, 67, 69, 83

T. Boulanger, A. Chrysochoos, C. Mabru, and A. Galtier. Calorimetric analysis of dissipative and thermoelastic effects associated with the fatigue behavior of steels. *International journal of fatigue*, 26(3):221–229, 2004. 5

G. Bradfield and H. Puesey. XLV. The hole of preferred orientation in elasticity investigations. *The London, Edinburgh, and Dublin Philosophical Magazine and Journal of Science*, 44(351):437–443, 1953. ISSN 1941-5982. doi: 10.1080/14786440408520326. URL https://doi.org/10.1080/14786440408520326http://www.tandfonline.com/doi/abs/10.1080/14786440408520326. 96

T. Bretheau and O. Castelnau. Rayons X et Matiere(RX2006), ch. 5. *edited by R. Guinebretiere & Ph. Goudeau. London: Hermes Science Publishing*, pages 123–154, 2006. 7

S. Brinckmann and E. Van der Giessen. Stress concentration at the surface of fatigued materials: a discrete dislocation dynamics study. *Advances in Computational and Experimental Engineering and Sciences*, 2003. URL http://homepage.ruhr-uni-bochum.de/steffen.brinckmann/WORK/DDD/papers/2003/paper{_}2.pdf. 17

S. Brinckmann and E. Van der Giessen. A discrete dislocation dynamics study aiming at understanding fatigue crack initiation. *Materials Science and Engineering A*, 387-389(1-2 SPEC. ISS.):461–464, 2004. ISSN 09215093. doi: 10.1016/j.msea.2004.01.142. 17

V. Bulatov and W. Cai. *Computer Simulations of Dislocations*. OUP Oxford, 2006. ISBN 9780198526148. URL https://books.google.fr/books?id=AdfbPfihVJsC. 54, 90

J. Burgers. Internal strains in solids. *Proc. Acad. Science*, 42:293, 1939. 23

W. Cai and W. Nix. *Imperfections in crystalline solids*. Cambridge University Press, 2016. 27

W. Cai, V. Bulatov, J. Justo, A. Argon, and S. Yip. Intrinsic Mobility of a Dissociated Dislocation in Silicon. *Physical Review Letters*, 84(15):3346–3349, 2000. ISSN 0031-9007. doi: 10.1103/PhysRevLett.84.3346. URL https://link.aps.org/doi/10.1103/PhysRevLett.84.3346. 51

W. Cai, A. Arsenlis, C. Weinberger, and V. Bulatov. A non-singular continuum theory of dislocations. *Journal of the Mechanics and Physics of Solids*, 54(3):561–587, 2006. ISSN 00225096. doi: 10.1016/j.jmps.2005.09.005. URL https://linkinghub.elsevier.com/retrieve/pii/S002250960500195X. 55, 56, 85, 102

P. Cao. Computer Experiments for Surface Diffusion: The Real Time in Monte Carlo Simulations. 73(16):2595–2598, 1994. 105

J. Chaboche and P. Lesne. A Non-Linear Continuous Fatigue Damage Model. *Fatigue & Fracture of Engineering Materials & Structures*, 11(1):1–17, 1988. ISSN 14602695. doi: 10.1111/j.1460-2695.1988.tb01216.x. 14

E. Charkaluk, A. Bignonnet, A. Constantinescu, and K. Dang Van. Fatigue design of structures under thermomechanical loadings. *Fatigue and Fracture of Engineering Materials and Structures*, 25(12):1199–1206, 2002. ISSN 8756758X. doi: 10.1046/j.1460-2695.2002.00612.x. 87

J. Chaussidon, C. Robertson, D. Rodney, and M. Fivel. Dislocation dynamics simulations of plasticity in Fe laths at low temperature. *Acta Materialia*, 56(19): 5466–5476, 2008. ISSN 13596454. doi: 10.1016/j.actamat.2008.07.047. URL http://dx.doi.org/10.1016/j.actamat.2008.07.047. 47, 70

Y. Chen and B. Roux. Generalized Metropolis acceptance criterion for hybrid non-equilibrium molecular dynamics - Monte Carlo simulations. *Journal of Chemical Physics*, 142(2), 2015. ISSN 00219606. doi: 10.1063/1.4904889. URL http://dx.doi.org/10.1063/1.4904889. 104

J. Chessa and T. Belytschko. Arbitrary discontinuities in space-time finite elements by level sets and X-FEM. *International Journal for Numerical Methods in Engineering*, 61(15):2595–2614, 2004. ISSN 00295981. doi: 10.1002/nme.1155. 15

S. Chirputkar, D. Qian, and C. Source. Coupled atomistic/continuum simulation based on extended space-time finite element method. *Computer Modeling in Engineering and Sciences*, 24(2/3):185, 2008. 15

C. Chow and J. Wang. An anisotropic theory of continuum damage mechanics for ductile fracture. *Engineering Fracture Mechanics*, 27(5):547–558, 1987a. ISSN 00137944. doi: 10.1016/0013-7944(87)90108-1. 14

C. Chow and J. Wang. An anisotropic theory of elasticity for continuum damage mechanics. *International Journal of Fracture*, 33(1):3–16, 1987b. ISSN 03769429. doi: 10.1007/BF00034895. 14

C. Chow and J. Wang. A finite element analysis of continuum damage mechanics for ductile fracture. *International Journal of Fracture*, 38(2):83–102, 1988. ISSN 03769429. doi: 10.1007/BF00033000. 14

A. Chrysochoos, B. Berthel, F. Latourte, S. Pagano, B. Wattrisse, and B. Weber. Local energy approach to steel fatigue. *Strain*, 44(4):327–334, 2008. ISSN 00392103. doi: 10.1111/j.1475-1305.2007.00381.x. 5, 88, 89

H. Cleveringa, E. Van der Giessen, and A. Needleman. A discrete dislocation analysis of rate effects on mode I crack growth. *Materials Science and Engineering A*, 317 (1-2):37–43, 2001. ISSN 09215093. doi: 10.1016/S0921-5093(01)01177-7. 17

D. Cojocaru and A. Karlsson. A simple numerical method of cycle jumps for cyclically loaded structures. *International Journal of Fatigue*, 28(12):1677–1689, 2006. ISSN 01421123. doi: 10.1016/j.ijfatigue.2006.01.010. 15

N. Connesson, F. Maquin, and F. Pierron. Experimental energy balance during the first cycles of cyclically loaded specimens under the conventional yield stress. *Experimental Mechanics*, 51(1):23–44, 2011. 5, 88, 89

P. Costa, R. Nwawe, H. Soares, L. Reis, M. Freitas, Y. Chen, and D. Montalvão. Review of multiaxial testing for very high cycle fatigue: From 'Conventional' to ultrasonic machines. *Machines*, 8(2), 2020. ISSN 20751702. doi: 10.3390/MACHINES8020025. 1

M. Croft, N. Jisrawi, Z. Zhong, K. Horvath, R. L. Holtz, M. Shepard, M. Lakshmipathy, K. Sadananda, J. Skaritka, V. Shukla, R. K. Sadangi, and T. Tsakalakos. Stress gradient induced strain localization in metals: High resolution strain cross sectioning via synchrotron X-Ray diffraction. *Journal of Engineering Materials and Technology, Transactions of the ASME*, 130(2):0210051–02100510, 2008. ISSN 00944289. doi: 10.1115/1.2840962. 9

Y. Cui, G. Po, and N. Ghoniem. Influence of loading control on strain bursts and dislocation avalanches at the nanometer and micrometer scale. *Physical Review B*, 95(6):1–12, 2017. ISSN 24699969. doi: 10.1103/PhysRevB.95.064103. 89

C. Darwin. XXXIV. The theory of X-ray reflexion. *The London, Edinburgh, and Dublin Philosophical Magazine and Journal of Science*, 27(158):315–333, 1914. 22

W. Davey. Precision Measurements of the Lattice Constants of Twelve Common Metals. *Physical Review*, 25(6):753–761, 1925. ISSN 0031-899X. doi: 10.1103/PhysRev.25.753. URL https://link.aps.org/doi/10.1103/PhysRev.25.753. 61, 80, 96

A. Davis, M. Shokouhian, and S. Ni. Loading estimates of lead, copper, cadmium, and zinc in urban runoff from specific sources. *Chemosphere*, 44(5):997–1009, 2001. ISSN 00456535. doi: 10.1016/S0045-6535(00)00561-0. URL https://linkinghub.elsevier.com/retrieve/pii/S0045653500005610. 65

E. J. Dawnkaski, D. Srivastava, and B. J. Garrison. Time-dependent Monte Carlo simulations of radical densities and distributions on the diamond {001} (2 × 1): H surface. *Chemical Physics Letters*, 232(5-6):524–530, 1995a. ISSN 00092614. doi: 10.1016/0009-2614(94)01393-A. 105

E. J. Dawnkaski, D. Srivastava, and B. J. Garrison. Time dependent Monte Carlo simulations of H reactions on the diamond {001}(2×1) surface under chemical vapor deposition conditions. *The Journal of Chemical Physics*, 102(23):9401–9411, 1995b. ISSN 00219606. doi: 10.1063/1.468808. 105

M. de Freitas. Multiaxial fatigue: From materials testing to life prediction. *Theoretical and Applied Fracture Mechanics*, 92:360–372, 2017. ISSN 01678442. doi: 10.1016/j.tafmec.2017.05.008. URL https://doi.org/10.1016/j.tafmec.2017.05.008. 1

C. Déprés, C. Robertson, and M. Fivel. Crack initiation in fatigue: experiments and three-dimensional dislocation simulations. *Materials Science and Engineering: A*, 387-389:288–291, 2004a. ISSN 09215093. doi: 10.1016/j.msea.2003.12.084. URL https://linkinghub.elsevier.com/retrieve/pii/S0921509304007075. 17, 20, 47, 93, 106

C. Déprés, C. Robertson, and M. Fivel. Low-strain fatigue in AISI 316L steel surface grains: a three-dimensional discrete dislocation dynamics modelling of the early cycles I. Dislocation microstructures and mechanical behaviour. *Philosophical Magazine*, 84(22):2257–2275, 2004b. ISSN 1478-6435. doi: 10.1080/14786430410001690051. URL http://www.tandfonline.com/doi/abs/10.1080/14786430410001690051. 70, 79, 93

C. Déprés, C. Robertson, and M. Fivel. Low-strain fatigue in 316L steel surface grains: A three dimension discrete dislocation dynamics modelling of the early cycles. Part 2: Persistent slip markings and micro-crack nucleation, 2006. ISSN 14786435. vii, 17, 18, 47, 88, 93

C. Déprés, G. Reddy, L. Tabourot, R. Sandhya, and S. Sankaran. First steps of crack initiation and propagation in fatigue of fcc crystals studied by dislocation dynamics. In *Engineering Systems Design and Analysis*, volume 44847, pages 297–306. American Society of Mechanical Engineers, 2012. 17

C. Déprés, G. Reddy, C. Robertson, and M. Fivel. An extensive 3D dislocation dynamics investigation of stage-I fatigue crack propagation. *Philosophical Magazine*, 94(36):4115–4137, 2014. ISSN 14786443. doi: 10.1080/14786435.2014.978830. URL http://dx.doi.org/10.1080/14786435.2014.978830. 17

C. Déprés, C. Robertson, and M. Fivel. 3D Discrete Dislocation Dynamics Investigations of Fatigue Crack Initiation and Propagation. *Aerospace Lab Journal*, AL09-01(9):1–8, 2015. doi: 10.12762/2015.AL09-01. 17

V. Deshpande, H. Cleveringa, E. Van der Giessen, and A. Needleman. A discrete dislocation analysis of fatigue crack growth. *Journal De Physique. IV : JP*, 11(5): 3189–3203, 2001. ISSN 11554339. doi: 10.1051/jp4:2001509. 17

V. Deshpande, A. Needleman, and E. Van der Giessen. Discrete dislocation plasticity modeling of short cracks in single crystals. *Acta Materialia*, 51:1–15, 2003a. 17

V. Deshpande, A. Needleman, and E. Van der Giessen. Scaling of discrete dislocation predictions for near-threshold fatigue crack growth. *Acta Materialia*, 51(15):4637–4651, 2003b. ISSN 13596454. doi: 10.1016/S1359-6454(03)00302-1. 17

R. Desmorat, A. Kane, M. Seyedi, and J. Sermage. Two scale damage model and related numerical issues for thermo-mechanical High Cycle Fatigue. *European Journal of Mechanics, A/Solids*, 26(6):909–935, 2007. ISSN 09977538. doi: 10.1016/j.euromechsol.2007.01.002. 15

B. Devincre, T. Hoc, and L. Kubin. Collinear interactions of dislocations and slip systems. *Materials Science and Engineering: A*, 400-401:182–185, 2005. ISSN 09215093. doi: 10.1016/j.msea.2005.02.071. URL https://linkinghub.elsevier.com/retrieve/pii/S0921509305003333. 47

J. Drouet, L. Dupuy, F. Onimus, F. Mompiou, S. Perusin, and A. Ambard. Dislocation dynamics simulations of interactions between gliding dislocations and radiation induced prismatic loops in zirconium. *Journal of Nuclear Materials*, 449(1-3):252–262, jun 2014. ISSN 00223115. doi: 10.1016/j.jnucmat.2013.11.049. URL http://dx.doi.org/10.1016/j.jnucmat.2013.11.049https://linkinghub.elsevier.com/retrieve/pii/S0022311513012877. i, 54, 55, 64, 79, 91, 104

C. Duarte and J. Oden. H-p clouds—anh-p meshless method. *Numerical Methods for Partial Differential Equations*, 12(6):673–705, 1996. ISSN 1098-2426. doi: 10.1002/(SICI)1098-2426(199611)12:63.0.CO;2-P. 14

M. Duesbery, N. Louat, and K. Sadananda. The mechanics and energetics of cross-slip. *Acta Metallurgica et Materialia*, 40(1):149–158, 1992. ISSN 09567151. doi: 10.1016/0956-7151(92)90208-V. URL https://linkinghub.elsevier.com/retrieve/pii/095671519290208V. 64

L. Dupuy and M. Fivel. A study of dislocation junctions in FCC metals by an orientation dependent line tension model. *Acta Materialia*, 50(19):4873–4885, 2002. ISSN 13596454. doi: 10.1016/S1359-6454(02)00356-7. URL https://linkinghub.elsevier.com/retrieve/pii/S1359645402003567. 62, 69

Y. Duyi and W. Zhenlin. A new approach to low-cycle fatigue damage based on exhaustion of static toughness and dissipation of cyclic plastic strain energy during fatigue. *International Journal of Fatigue*, 23(8):679–687, 2001. ISSN 01421123. doi: 10.1016/S0142-1123(01)00027-5. 87

T. El-Achkar and D. Weygand. Discrete dislocation dynamics study of dislocation microstructure during cyclic loading. *Fatigue of Materials at Very High Numbers of Loading Cycles*, pages 395–416, 2018. doi: 10.1007/978-3-658-24531-3_18. vii, 18, 19

T. El-Achkar and D. Weygand. Analysis of dislocation microstructure characteristics of surface grains under cyclic loading by discrete dislocation dynamics. *Modelling and Simulation in Materials Science and Engineering*, 27(5), 2019. ISSN 1361651X. doi: 10.1088/1361-651X/ab1b7c. 18

J. El-Awady, S. Bulent Biner, and N. Ghoniem. A self-consistent boundary element, parametric dislocation dynamics formulation of plastic flow in finite volumes. *Journal of the Mechanics and Physics of Solids*, 56(5):2019–2035, 2008. ISSN 00225096. doi: 10.1016/j.jmps.2007.11.002. 17, 88

F. Ellyin and D. Kujawski. Plastic strain energy in fatigue failure. 1984. 87

C. Erel, G. Po, T. Crosby, and N. Ghoniem. Generation and interaction mechanisms of prismatic dislocation loops in FCC metals. *Computational Materials Science*, 140:32–46, 2017a. ISSN 09270256. doi: 10.1016/j.commatsci.2017.07.043. URL https://doi.org/10.1016/j.commatsci.2017.07.043. 19

C. Erel, G. Po, and N. Ghoniem. Dependence of hardening and saturation stress in persistent slip bands on strain amplitude during cyclic fatigue loading. *Philosophical Magazine*, 97(32):2947–2970, 2017b. ISSN 14786443. doi: 10.1080/14786435.2017.1361555. 93

B. Escaig. Sur le glissement dévié des dislocations dans la structure cubique à faces centrées. *Journal de Physique*, 29(2-3):225–239, 1968. ISSN 0302-0738. doi: 10.1051/jphys:01968002902-3022500. URL http://www.edpsciences.org/10.1051/jphys:01968002902-3022500. 48

J. Eshelby. Elastic inclusions and inhomogeneities, Vol. 2, 1961. 12

U. Essmann, U. Gösele, and H. Mughrabi. A model of extrusions and intrusions in fatigued metals I. Point-defect production and the growth of extrusions. *Philosophical Magazine A: Physics of Condensed Matter, Structure, De-*

fects and Mechanical Properties, 44(2):405–426, 1981. ISSN 01418610. doi: 10.1080/01418618108239541. 10

G. Esteban-Manzanares, R. Santos-Güemes, I. Papadimitriou, E. Martínez, and J. LLorca. Influence of the stress state on the cross-slip free energy barrier in Al: An atomistic investigation. *Acta Materialia*, 184:109–119, 2020. ISSN 13596454. doi: 10.1016/j.actamat.2019.10.055. URL https://doi.org/10.1016/j.actamat.2019.10.055. i, ii, xii, 19, 20, 21, 67, 71, 73, 79, 83, 84, 85, 86, 91, 102, 104

P. Ewald. Zur begründung der kristalloptik. *Annalen der Physik*, 359:557–597, 1917. 22

J. Ewing and W. Rosenhain. The crystalline structure of metals. *Philosophical Transactions of the Royal Society*, 193:353–391, 1899. 22

C. Feltner and J. Morrow. Microplastic strain hysteresis energy as a criterion for fatigue fracture. 1961. 87

R. Fleischer. Cross slip of extended dislocations. *Acta Metallurgica*, 7(2):134–135, 1959. ISSN 00016160. doi: 10.1016/0001-6160(59)90122-1. URL https://linkinghub.elsevier.com/retrieve/pii/0001616059901221. x, 48

J. Frenkel. Zur theorie der elastizitätsgrenze und der festigkeit kristallinischer körper. *Zeitschrift für Physik*, 37(7-8):572–609, 1926. viii, 22, 23

A. M. Freudenthal. The statistical aspect of fatigue of materials. *Proceedings of the Royal Society of London. Series A. Mathematical and Physical Sciences*, 187 (1011):416–429, 1946. ISSN 0080-4630. doi: 10.1098/rspa.1946.0086. 1

J. Friedel. *Les Dislocations*. Pergamon, 1964. URL https://books.google.fr/books?id=R8QYzQEACAAJ. x, 48

Y. Furuya, S. Matsuoka, T. Abe, and K. Yamaguchi. Gigacycle fatigue properties for high-strength low-alloy steel at 100 Hz, 600 Hz, and 20 kHz. *Scripta Materialia*, 46(2):157–162, 2002. 3

A. Galtier. *Contribution à l'étude de l'endommagement des aciers sous sollicitations uni ou multi-axiales*. PhD thesis, Paris, ENSAM, 1993. 87

A. V. Granato, K. Lücke, J. Schlipf, and L. J. Teutonico. Entropy Factors for Thermally Activated Unpinning of Dislocations. *Journal of Applied Physics*, 35 (9):2732–2745, 1964. ISSN 0021-8979. doi: 10.1063/1.1713833. URL http://aip.scitation.org/doi/10.1063/1.1713833. 73

G. Halford. *Stored energy of cold work changes induced by cyclic deformation*. University of Illinois at Urbana-Champaign, 1966. 87, 88

P. Hilgendorff, A. Grigorescu, M. Zimmermann, C. Fritzen, and H. Christ. Simulation of irreversible damage accumulation in the very high cycle fatigue (VHCF) regime using the boundary element method. *Materials Science and Engineering A*, 575:169–176, 2013. ISSN 09215093. doi: 10.1016/j.msea.2013.03.072. URL http://dx.doi.org/10.1016/j.msea.2013.03.072. vii, 14, 16, 17, 88

P. Hilgendorff, A. Grigorescu, M. Zimmermann, C. Fritzen, and H. Christ. Simulation of Deformation-induced Martensite Formation and its Influence on the Resonant Behavior in the Very High Cycle Fatigue (VHCF) Regime. *Procedia Materials Science*, 3:1135–1142, 2014. ISSN 22118128. doi: 10.1016/j.mspro.2014.06.185. URL http://dx.doi.org/10.1016/j.mspro.2014.06.185. 17

P. Hilgendorff, A. Grigorescu, M. Zimmermann, C. Fritzen, and H. Christ. Cyclic deformation behavior of austenitic Cr–Ni-steels in the VHCF regime: Part II – Microstructure-sensitive simulation. *International Journal of Fatigue*, 93:261–271, 2016a. ISSN 01421123. doi: 10.1016/j.ijfatigue.2016.05.006. URL http://dx.doi.org/10.1016/j.ijfatigue.2016.05.006. 17

P. Hilgendorff, A. Grigorescu, M. Zimmermann, C. Fritzen, and H. Christ. Modeling and simulation of temperature-dependent cyclic plastic deformation of austenitic stainless steels at the VHCF limit. *Procedia Structural Integrity*, 2:1156–1163, 2016b. ISSN 24523216. doi: 10.1016/j.prostr.2016.06.148. URL http://dx.doi.org/10.1016/j.prostr.2016.06.148. 17

P. Hirsch. *The Physics of Metals*. Cambridge University Press, 2009. ISBN 9780521113106. URL https://books.google.fr/books?id=5JOKPwAACAAJ. 47

J. Hirth and J. Lothe. *Theory of Dislocations*. Krieger Publishing Company, 1982. ISBN 9780894646171. URL https://books.google.fr/books?id=LFZGAAAAYAAJ. 37, 38

M. Huang, J. Tong, and Z. Li. A study of fatigue crack tip characteristics using discrete dislocation dynamics. *International Journal of Plasticity*, 54:229–246, 2014. ISSN 07496419. doi: 10.1016/j.ijplas.2013.08.016. URL http://dx.doi.org/10.1016/j.ijplas.2013.08.016. 17

T. Hughes and G. Hulbert. Space-time finite element methods for elastodynamics: Formulations and error estimates. *Computer Methods in Applied Mechanics and Engineering*, 66(3):339–363, 1988. ISSN 00457825. doi: 10.1016/0045-7825(88)90006-0. 15

G. Hulbert and T. Hughes. Space-time finite element methods for second-order hyperbolic equations. *Computer Methods in Applied Mechanics and Engineering*, 84(3):327–348, 1990. ISSN 00457825. doi: 10.1016/0045-7825(90)90082-W. 15

A. Hussein, S. Rao, M. Uchic, D. Dimiduk, and J. El-Awady. Microstructurally based cross-slip mechanisms and their effects on dislocation microstructure evolution in fcc crystals. *Acta Materialia*, 85:180–190, 2015. ISSN 13596454. doi: 10.1016/j.actamat.2014.10.067. URL http://dx.doi.org/10.1016/j.actamat.2014.10.067. 20, 47, 70, 79

H. Itoga, K. Tokaji, M. Nakajima, and H. N. Ko. Effect of surface roughness on stepwise S-N characteristics in high strength steel. *International Journal of Fatigue*, 25(5):379–385, 2003. ISSN 01421123. doi: 10.1016/S0142-1123(02)00166-4. 12

P. Jackson. The role of cross-slip in the plastic deformation of crystals. *Materials Science and Engineering*, 57(1):39–47, 1983. ISSN 00255416. doi: 10.1016/0025-5416(83)90025-3. URL https://linkinghub.elsevier.com/retrieve/pii/0025541683900253. 47

P. Jackson. Dislocation modelling of shear in f.c.c. crystals. *Progress in Materials Science*, 29(1-2):139–175, 1985. ISSN 00796425. doi: 10.1016/0079-6425(85)90009-X. URL https://linkinghub.elsevier.com/retrieve/pii/007964258590009X. 47

C. Jin, Y. Xiang, and G. Lu. Dislocation cross-slip mechanisms in aluminum. *Philosophical Magazine*, 91(32):4109–4125, 2011. ISSN 1478-6435. doi: 10.1080/14786435.2011.602030. URL http://www.tandfonline.com/doi/abs/10.1080/14786435.2011.602030. 49

L. Kachanov. Rupture time under creep conditions. 1958. 14

K. Kang, J. Yin, and W. Cai. Stress dependence of cross slip energy barrier for face-centered cubic nickel. *Journal of the Mechanics and Physics of Solids*, 62:181–193, 2014. ISSN 00225096. doi: 10.1016/j.jmps.2013.09.023. URL https://linkinghub.elsevier.com/retrieve/pii/S002250961300207X. i, ii, x, xi, 20, 21, 50, 51, 52, 53, 57, 58, 60, 62, 65, 66, 67, 69, 71, 73, 76, 79, 86, 101, 102

M. Karuskevich, O. Karuskevich, T. Maslak, and S. Schepak. Extrusion/intrusion structures as quantitative indicators of accumulated fatigue damage. *International Journal of Fatigue*, 39:116–121, 2012. ISSN 01421123. doi: 10.1016/j.ijfatigue.2011.02.007. URL http://dx.doi.org/10.1016/j.ijfatigue.2011.02.007. vii, 9

V. Kazymyrovych. Very high cycle fatigue of engineering materials - A literature review. pages 1–37, 2009. URL www.kau.se. 1

C. Kittel and P. McEuen. *Introduction to Solid State Physics*. John Wiley & Sons, 2018. ISBN 9781119454168. URL https://books.google.fr/books?id=S3gAugEACAAJ. 61, 80, 96

J. Krapez and D. Pacou. Thermography detection of damage initiation during fatigue tests. *Thermosense XXIV*, 4710(March 2002):435–449, 2002. doi: 10.1117/12.459593. 87

J. Krapez, D. Pacou, and G. Gardette. Lock-in thermography and fatigue limit of metals. *Office National D'etudes et de recherches aerospatiales*, (187), 2000. 4, 87

L. Kubin. *Dislocations, Mesoscale Simulations and Plastic Flow*. Oxford Series on Materials Modelling. OUP Oxford, 2013. ISBN 9780198525011. URL https://books.google.fr/books?id=Uit4KrwBmrwC. 31

L. Kubin, G. Canova, M. Condat, B. Devincre, V. Pontikis, and Y. Bréchet. Dislocation Microstructures and Plastic Flow: A 3D Simulation. *Solid State Phenomena*, 23-24:455–472, 1992. ISSN 1662-9779. doi: 10.4028/www.scientific.net/SSP.23-24.455. URL https://www.scientific.net/SSP.23-24.455. 20, 47, 70, 79

C. Kung and M. Fine. Fatigue Crack Initiation and Microcrack Growth in 2024-T4 and 2124-T4 Aluminum Alloys. *Fatigue and Fracture of Engineering Materials and Structures*, 30(5):443–457, 2007. ISSN 8756758X. doi: 10.1111/j.1460-2695.2006.01088.x. 12

W. Kuykendall, Y. Wang, and W. Cai. Stress effects on the energy barrier and mechanisms of cross-slip in FCC nickel. *Journal of the Mechanics and Physics of Solids*, 144:1–13, 2020. ISSN 00225096. doi: 10.1016/j.jmps.2020.104105. URL https://doi.org/10.1016/j.jmps.2020.104105. 49, 57, 71, 79

G. La Rosa and A. Risitano. Thermographic methodology for rapid determination of the fatigue limit of materials and mechanical components. *International Journal of Fatigue*, 22(1):65–73, 2000. ISSN 01421123. doi: 10.1016/S0142-1123(99)00088-2. 4, 87

C. Lachowicz. Calculation of the elastic–plastic strain energy density under cyclic and random loading. *International Journal of Fatigue*, 23(7):643–652, aug 2001. ISSN 01421123. doi: 10.1016/S0142-1123(00)00102-X. URL https://linkinghub.elsevier.com/retrieve/pii/S014211230000102X. 89

H. Ledbetter and E. Naimon. Elastic Properties of Metals and Alloys. II. Copper. *Journal of Physical and Chemical Reference Data*, 3(4):897–935, 1974. ISSN 0047-2689. doi: 10.1063/1.3253150. URL http://aip.scitation.org/doi/10.1063/1.3253150. 61, 80

J. Lemaitre and J. Chaboche. *Mechanics of solid materials*. Cambridge university press, 1994. 14

J. Lemaitre, J. Sermage, and R. Desmorat. A two scale damage concept applied to fatigue. *International Journal of Fracture*, 97(1-4):67–81, 1999. ISSN 03769429. doi: 10.1023/a:1018641414428. 14, 15

H. Liu, X. Zhou, D. Hu, J. Song, R. Wang, and J. Mao. A new variational line tension model for accurate evaluation of the stress effect on cross-slip energy barrier in face-centered cubic metals. *Scripta Materialia*, 166:24–28, 2019. ISSN 13596462. doi: 10.1016/j.scriptamat.2019.03.002. URL https://doi.org/10.1016/j.scriptamat.2019.03.002. 71, 79

M. Longsworth. Biasing Technique in Parallel Monte Carlo Simulations for Segregation in Solids. Master's thesis, Rheinisch-Westfälische Technische Hochschule Aachen, 2017. URL https://juser.fz-juelich.de/record/840660/files/longsworth-thesis-23-11-2017.pdf. 104

M. Longsworth and M. Fivel. The effect of stress on the cross-slip energy in face-centered cubic metals: A study using dislocation dynamics simulations and line tension models. *Journal of the Mechanics and Physics of Solids*, 148:104281, 2021a. ISSN 00225096. doi: 10.1016/j.jmps.2020.104281. URL https://doi.org/10.1016/j.jmps.2020.104281. 71, 79, 83, 86, 96, 102

M. Longsworth and M. Fivel. Investigating the cross-slip rate in face-centered cubic metals using an atomistic-based cross-slip model in dislocation dynamics simulations. *Journal of the Mechanics and Physics of Solids*, 153:104449, 2021b. ISSN 00225096. doi: 10.1016/j.jmps.2021.104449. URL https://doi.org/10.1016/j.jmps.2021.104449. 96, 103

P. Lukáš and M. Klesnil. Cyclic stress-strain response and fatigue life of metals in low amplitude region. *Materials Science and Engineering*, 11(6):345–356, jun 1973. ISSN 00255416. doi: 10.1016/0025-5416(73)90125-0. URL https://linkinghub.elsevier.com/retrieve/pii/0025541673901250. 7, 78

P. Lukáš and L. Kunz. Role of persistent slip bands in fatigue. *Philosophical Magazine*, 84(3-5):317–330, 2004. ISSN 14786435. doi: 10.1080/14786430310001610339. 10

P. Lukáš, M. Klesnil, J. Krejčí, and P. Ryš. Substructure of Persistent Slip Bands in Cyclically Deformed Copper. *Physica Status Solidi (B)*, 15(1):71–82, 1966. ISSN 15213951. doi: 10.1002/pssb.19660150105. 10

M. Luong. Infrared thermographic scanning of fatigue in metals. *Nuclear Engineering and Design*, 158(2-3):363–376, 1995. vii, 4

M. Luong. Fatigue limit evaluation of metals using an infrared thermographic technique. *Mechanics of materials*, 28(1-4):155–163, 1998. 4, 87

A. Malka-Markovitz and D. Mordehai. Cross-slip in face-centered cubic metals: a general Escaig stress-dependent activation energy line tension model. *Philosophical Magazine*, 98(5):347–370, 2018. doi: 10.1080/14786435.2017.1406194. URL https://doi.org/10.1080/14786435.2017.1406194. xi, 53, 69, 74, 75, 76, 79, 86, 91, 92, 102

A. Malka-Markovitz and D. Mordehai. Cross-slip in face centred cubic metals: a general full stress-field dependent activation energy line-tension model. *Philosophical Magazine*, 99(12):1460–1480, 2019. ISSN 1478-6435. doi: 10.1080/14786435.2019.1584410. URL https://www.tandfonline.com/doi/full/10.1080/14786435.2019.1584410. i, ii, xi, xii, 20, 21, 50, 53, 57, 65, 66, 67, 71, 76, 79, 82, 86, 91, 102, 105

A. Malka-Markovitz, B. Devincre, and D. Mordehai. A molecular dynamics-informed probabilistic cross-slip model in discrete dislocation dynamics. *Scripta Materialia*, 190:7–11, 2021. ISSN 13596462. doi: 10.1016/j.scriptamat.2020.08.008. URL https://doi.org/10.1016/j.scriptamat.2020.08.008. 71, 76, 79

J. Man, K. Obrtlík, and J. Polák. Study of surface relief evolution in fatigued 316L austenitic stainless steel by AFM. *Materials Science and Engineering A*, 351(1-2):123–132, 2003. ISSN 09215093. doi: 10.1016/S0921-5093(02)00846-8. 16

B. W. Mangum, G. T. Furukawa, K. G. Kreider, C. W. Meyer, D. C. Ripple, G. F. Strouse, W. L. Tew, M. R. Moldover, B. C. Johnson, H. W. Yoon, C. E. Gibson, and R. D. Saunders. The Kelvin and temperature measurements. *Journal of Research of the National Institute of Standards and Technology*, 106(1):105, 2001. doi: 10.6028/jres.106.006. URL https://nvlpubs.nist.gov/nistpubs/jres/106/1/j61man.pdf. 80, 96, 105

C. Mareau, D. Cuillerier, and F. Morel. Experimental and numerical study of the evolution of stored and dissipated energies in a medium carbon steel under cyclic loading. *Mechanics of Materials*, 60:93–106, 2013. ISSN 01676636. doi: 10.1016/j.

mechmat.2013.01.011. URL http://dx.doi.org/10.1016/j.mechmat.2013.01.011. 89

E. Martínez, J. Marian, A. Arsenlis, M. Victoria, and J. Perlado. Atomistically informed dislocation dynamics in fcc crystals. *Journal of the Mechanics and Physics of Solids*, 56(3):869–895, 2008. ISSN 00225096. doi: 10.1016/j.jmps.2007.06.014. URL https://linkinghub.elsevier.com/retrieve/pii/S0022509607001408. 54

J. Melenk and I. Babuška. The partition of unity finite element method: Basic theory and applications. *Computer Methods in Applied Mechanics and Engineering*, 139 (1-4):289–314, 1996. ISSN 00457825. doi: 10.1016/S0045-7825(96)01087-0. 14

G. Meneghetti. Analysis of the fatigue strength of a stainless steel based on the energy dissipation. *International Journal of Fatigue*, 29(1):81–94, 2007. ISSN 01421123. doi: 10.1016/j.ijfatigue.2006.02.043. 87

G. Meneghetti, M. Ricotta, and B. Atzori. Experimental evaluation of fatigue damage in two-stage loading tests based on the energy dissipation. *Proceedings of the Institution of Mechanical Engineers, Part C: Journal of Mechanical Engineering Science*, 229(7):1280–1291, 2015. ISSN 20412983. doi: 10.1177/0954406214559112. 87

F. Meng, E. Ferrié, C. Déprés, and M. Fivel. 3D discrete dislocation dynamic investigations of persistent slip band formation in FCC metals under cyclical deformation. *International Journal of Fatigue*, 149(December 2020):106234, 2021. ISSN 01421123. doi: 10.1016/j.ijfatigue.2021.106234. 18

W. Meyer and H. Neldel. Relation between the energy constant and the quantity constant in the conductivity–temperature formula of oxide semiconductors. *Z. tech. Phys*, 18(12):588–593, 1937. 73

D. Mordehai, I. Kelson, and G. Makov. Cross-slip and annihilation of screw dislocations in Cu: a molecular dynamics study. *Materials Science and Engineering: A*, 400-401:37–39, 2005. ISSN 09215093. doi: 10.1016/j.msea.2005.03.077. URL https://linkinghub.elsevier.com/retrieve/pii/S0921509305003692. 19

H. Mughrabi. The cyclic hardening and saturation behaviour of copper single crystals. *Materials Science and Engineering*, 33(2):207–223, 1978. ISSN 00255416. doi: 10.1016/0025-5416(78)90174-X. 96, 106

H. Mughrabi. Dislocations in fatigue. *Dislocations and properties of real materials*, pages 244–262, 1984. 10, 11

H. Mughrabi. *Cyclic Strain Localization in Fatigued Metals*, pages 271–281. Springer Netherlands, Dordrecht, 2001. ISBN 978-94-010-0656-9. doi: 10.1007/978-94-010-0656-9_20. URL https://doi.org/10.1007/978-94-010-0656-9{_}20. 9, 10, 88

H. Mughrabi. On 'multi-stage'fatigue life diagrams and the relevant life-controlling mechanisms in ultrahigh-cycle fatigue. *Fatigue & Fracture of Engineering Materials & Structures*, 25(8-9):755–764, 2002. vii, 9, 10, 11, 12, 13, 16

H. Mughrabi. Specific features and mechanisms of fatigue in the ultrahigh-cycle regime. *International Journal of Fatigue*, 28(11):1501–1508, 2006. ISSN 01421123. doi: 10.1016/j.ijfatigue.2005.05.018. vii, 10, 13

H. Mughrabi. Cyclic Slip Irreversibilities and the Evolution of Fatigue Damage. *Metallurgical and Materials Transactions B*, 40(4):431–453, aug 2009. ISSN 1073-5615. doi: 10.1007/s11663-009-9240-4. URL http://link.springer.com/10.1007/s11663-009-9240-4. 78

H. Mughrabi, R. Wang, K. Differt, and U. Essmann. Fatigue crack initiation by cyclic slip irreversibilities in high-cycle fatigue. In *Fatigue mechanisms: advances in quantitative measurement of physical damage*. ASTM International, 1983. 10, 11

R. Munier, C. Doudard, S. Calloch, and B. Weber. Determination of high cycle fatigue properties of a wide range of steel sheet grades from self-heating measurements. *International Journal of Fatigue*, 63:46–61, 2014. 4

S. Murakami and Y. Liu. Mesh-dependence in local approach to creep fracture. *International Journal of Damage Mechanics*, 4(3):230–250, 1995. 14

Y. Murakami, T. Nomoto, and T. Ueda. Factors influencing the mechanism of superlong fatigue failure in steels. *Fatigue & fracture of engineering materials & structures (Print)*, 22(7):581–590, 1999. 12

S. Nishijima and K. Kanazawa. Stepwise SN curve and fish-eye failure in gigacycle fatigue. *Fatigue & fracture of engineering materials & structures*, 22(7):601–607, 1999. 13

W. Nix. Partial Dislocation Tutorial for FCC metals. pages 1–14, 2010. viii, ix, 27, 29, 30, 35, 37, 38, 39

T. Nogaret, D. Rodney, M. Fivel, and C. Robertson. Clear band formation simulated by dislocation dynamics: Role of helical turns and pile-ups. *Journal*

of Nuclear Materials, 380(1-3):22–29, 2008. ISSN 00223115. doi: 10.1016/j.jnucmat.2008.07.001. URL https://linkinghub.elsevier.com/retrieve/pii/S002231150800367X. 47

S. Olarnrithinun. A Short Review of 2D-Discrete Dislocation Modeling for Fracture / Fatigue. 6:45–57, 2013. 17

E. Oren, E. Yahel, and G. Makov. Kinetics of dislocation cross-slip: A molecular dynamics study. *Computational Materials Science*, 138:246–254, 2017. ISSN 09270256. doi: 10.1016/j.commatsci.2017.06.039. URL http://dx.doi.org/10.1016/j.commatsci.2017.06.039. i, ii, xii, 19, 21, 71, 79, 81, 82, 83, 85, 86, 103

E. Orowan. Zur Kristallplastizität. i. *Zeitschrift für Physik*, 89(9-10):605–613, 1934a. 23

E. Orowan. Zur Kristallplastizität. ii. *Zeitschrift für Physik*, 89(9-10):614–633, 1934b. 23

T. Ors, N. Ranc, M. Pelerin, V. Michel, V. Favier, O. Castelnau, C. Mocuta, and D. Thiaudière. Microsecond time-resolved x-ray diffraction for the investigation of fatigue behavior during ultrasonic fatigue loading. *Journal of Synchrotron Radiation*, 26:1660–1670, 2019. ISSN 16005775. doi: 10.1107/S1600577519008518. vii, 5, 6, 7, 8, 89, 112

M. Paas, P. Schreurs, and W. Brekelmans. A continuum approach to brittle and fatigue damage: Theory and numerical procedures. *International Journal of Solids and Structures*, 30(4):579–599, 1993. ISSN 00207683. doi: 10.1016/0020-7683(93)90189-E. URL http://dx.doi.org/10.1016/0020-7683(93)90189-E. 14

V. Pandey, I. Singh, and B. Mishra. A Strain-based continuum damage model for low cycle fatigue under different strain ratios. *Engineering Fracture Mechanics*, 242 (December 2020):107479, 2021. ISSN 00137944. doi: 10.1016/j.engfracmech.2020.107479. URL https://doi.org/10.1016/j.engfracmech.2020.107479. 14, 15

J. Pascoe, R. Alderliesten, and R. Benedictus. Methods for the prediction of fatigue delamination growth in composites and adhesive bonds - A critical review. *Engineering Fracture Mechanics*, 112-113:72–96, 2013. ISSN 00137944. doi: 10.1016/j.engfracmech.2013.10.003. URL http://dx.doi.org/10.1016/j.engfracmech.2013.10.003. 14, 17

R. Peerlings, W. Brekelmans, R. Borst, and M. Geers. Gradient-enhanced damage modelling of high-cycle fatigue. (December 1999):1547–1569, 2000. 14

J. Philibert. Dislocations et déformation plastique. *Les éditions de la physique in École d'été d'Yravals*, 101, 1979. 61, 80, 96

J. Polak. *Cyclic plasticity and low cycle fatigue life of metals*. Elsevier Amsterdam, 1991. 7

M. Polanyi. Über eine Art Gitterstörung, die einen Kristall plastisch machen könnte. *Zeitschrift für Physik*, 89(9):660–664, 1934. 23

G. Prasad Reddy, C. Robertson, C. Déprés, and M. Fivel. Effect of grain disorientation on early fatigue crack propagation in face-centred-cubic polycrystals: A three-dimensional dislocation dynamics investigation. *Acta Materialia*, 61(14): 5300–5310, 2013. ISSN 13596454. doi: 10.1016/j.actamat.2013.05.021. 17

W. Püschl. The Energy of Constrictions in Extended Dislocations. *physica status solidi (b)*, 162(2):363–370, 1990. ISSN 03701972. doi: 10.1002/pssb.2221620205. URL http://doi.wiley.com/10.1002/pssb.2221620205. 63, 67

W. Püschl. Models for dislocation cross-slip in close-packed crystal structures: a critical review. *Progress in Materials Science*, 47(4):415–461, jan 2002. ISSN 00796425. doi: 10.1016/S0079-6425(01)00003-2. URL https://linkinghub.elsevier.com/retrieve/pii/S0079642501000032. 49

B. Pyttel, D. Schwerdt, and C. Berger. Very high cycle fatigue–Is there a fatigue limit? *International Journal of fatigue*, 33(1):49–58, 2011. 3

B. Ramírez, N. Ghoniem, and G. Po. Ab initio continuum model for the influence of local stress on cross-slip of screw dislocations in fcc metals. *Physical Review B*, 86(9):1–11, 2012. ISSN 1098-0121. doi: 10.1103/PhysRevB.86.094115. URL https://link.aps.org/doi/10.1103/PhysRevB.86.094115. 49, 56, 61, 62, 63, 64, 65, 67, 69, 79, 86, 101, 102

N. Ranc. Fast determination of fatigue behavior of materials beyond one billon cycles, 2017. vii, 2

N. Ranc, A. Blanche, D. Ryckelynck, and A. Chrysochoos. POD Preprocessing of IR Thermal Data to Assess Heat Source Distributions. *Experimental Mechanics*, 55(4):725–739, 2015. ISSN 17412765. doi: 10.1007/s11340-014-9858-2. 6

S. Rao, T. Parthasarathy, and C. Woodward. Atomistic simulation of cross-slip processes in model fcc structures. *Philosophical Magazine A*, 79(5):1167–1192, 1999. ISSN 0141-8610. doi: 10.1080/01418619908210354. URL http://www.tandfonline.com/doi/abs/10.1080/01418619908210354. 49, 64, 67

S. Rao, D. Dimiduk, J. El-Awady, T. Parthasarathy, M. Uchic, and C. Woodward. Atomistic simulations of cross-slip nucleation at screw dislocation intersections in face-centered cubic nickel. *Philosophical Magazine*, 89(34-36): 3351–3369, 2009. ISSN 1478-6435. doi: 10.1080/14786430903286201. URL http://www.tandfonline.com/doi/abs/10.1080/14786430903286201. 49

S. Rao, D. Dimiduk, C. Woodward, and T. Parthasarathy. On the Escaig obstacle hypothesis for cross-slip in face-centered-cubic materials. *Philosophical Magazine Letters*, 91(7):452–457, 2011. ISSN 0950-0839. doi: 10.1080/09500839.2011.581703. URL https://www.tandfonline.com/doi/full/10.1080/09500839.2011.581703. 49

S. Rao, D. Dimiduk, J. El-Awady, T. Parthasarathy, M. Uchic, and C. Woodward. Screw dislocation cross slip at cross-slip plane jogs and screw dipole annihilation in FCC Cu and Ni investigated via atomistic simulations. *Acta Materialia*, 101: 10–15, 2015. ISSN 13596454. doi: 10.1016/j.actamat.2015.08.070. URL http://dx.doi.org/10.1016/j.actamat.2015.08.070. 49

T. Rasmussen, K. Jacobsen, T. Leffers, and O. Pedersen. Simulations of the atomic structure, energetics, and cross slip of screw dislocations in copper. *Physical Review B*, 56(6):2977–2990, 1997a. ISSN 0163-1829. doi: 10.1103/PhysRevB.56.2977. URL https://link.aps.org/doi/10.1103/PhysRevB.56.2977. 49, 63, 64

T. Rasmussen, K. Jacobsen, T. Leffers, O. Pedersen, S. Srinivasan, and H. Jónsson. Atomistic Determination of Cross-Slip Pathway and Energetics. *Physical Review Letters*, 79(19):3676–3679, 1997b. ISSN 0031-9007. doi: 10.1103/PhysRevLett.79.3676. URL https://link.aps.org/doi/10.1103/PhysRevLett.79.3676. 49

T. Rasmussen, T. Vegge, T. Leffers, O. Pedersen, and K. Jacobsen. Simulation of structure and annihilation of screw dislocation dipoles. *Philosophical Magazine A: Physics of Condensed Matter, Structure, Defects and Mechanical Properties*, 80(5):1273–1290, 2000. ISSN 01418610. doi: 10.1080/01418610008212115. 85

W. Röntgen. On a new kind of rays. *Science*, 3(59):227–231, 1896. 22

P. Rosakis, A. J. Rosakis, G. Ravichandran, and J. Hodowany. Thermodynamic internal variable model for the partition of plastic work into heat and stored energy in metals. *Journal of the Mechanics and Physics of Solids*, 48(3):581–607, 2000. ISSN 00225096. doi: 10.1016/S0022-5096(99)00048-4. 89

G. Saada. Cross-slip and work hardening of f.c.c. crystals. *Materials Science and Engineering: A*, 137:177–183, 1991. ISSN 09215093. doi: 10.1016/

0921-5093(91)90333-I. URL https://linkinghub.elsevier.com/retrieve/pii/092150939190333I. 63, 67

T. Sakai. Experimental evidence of duplex SN characteristics in wide life region for high strength steels. In *Proceedings the 7th International Fatigue Congress*, volume 1, pages 573–578. Higher Education Press, 1999. 13

S. Schmauder and L. Mishnaevsky. *Micromechanics and Nanosimulation of Metals and Composites: Advanced Methods and Theoretical Concepts*. Springer Berlin Heidelberg, 2008. ISBN 9783540786788. URL https://books.google.fr/books?id=QcyxI-3EG4cC. 61, 80, 96

G. Schöck. Atomic dislocation core parameters. *physica status solidi (b)*, 247(2): 265–268, 2010. ISSN 03701972. doi: 10.1002/pssb.200945379. URL http://doi.wiley.com/10.1002/pssb.200945379. 49, 55, 56, 67, 86, 102

G. Schoeck. The Peierls model: Progress and limitations. *Materials Science and Engineering A*, 400-401(1-2 SUPPL.):7–17, 2005. ISSN 09215093. doi: 10.1016/j.msea.2005.03.050. 55

P. Seelan, J. Dulieu-Barton, and F. Pierron. Microstructural Assessment of 316L Stainless Steel Using Infrared Thermography Based Measurement of Energy Dissipation Arising from Cyclic Loading. *Mechanics of Materials*, 148(October 2019):103455, 2020. ISSN 01676636. doi: 10.1016/j.mechmat.2020.103455. URL https://doi.org/10.1016/j.mechmat.2020.103455. 88, 89

K. Shiozawa, L. Lu, and S. Ishihara. S–N curve characteristics and subsurface crack initiation behaviour in ultra-long life fatigue of a high carbon-chromium bearing steel. *Fatigue & Fracture of Engineering Materials & Structures*, 24(12):781–790, 2001. 3

R. Sills, W. Kuykendall, A. Aghaei, and W. Cai. *Fundamentals of Dislocation Dynamics Simulations*, pages 53–87. Springer International Publishing, 2016. ISBN 978-3-319-33480-6. doi: 10.1007/978-3-319-33480-6_2. URL https://doi.org/10.1007/978-3-319-33480-6{_}2. 54

C. Sobie, L. Capolungo, D. McDowell, and E. Martínez. Modal analysis of dislocation vibration and reaction attempt frequency. *Acta Materialia*, 134:203–210, 2017. ISSN 13596454. doi: 10.1016/j.actamat.2017.02.005. URL http://dx.doi.org/10.1016/j.actamat.2017.02.005. 73, 79, 91, 105

S. Stanzl-Tschegg. Very high cycle fatigue measuring techniques. *International Journal of Fatigue*, 60:2–17, 2014. ISSN 01421123. doi: 10.1016/j.ijfatigue.2012.11.016. URL http://dx.doi.org/10.1016/j.ijfatigue.2012.11.016. 3

S. Stanzl-Tschegg and H. Mayer. Fatigue and fatigue crack growth of aluminium alloys at very high numbers of cycles. *International Journal of Fatigue*, 23(SUPPL. 1):231–237, 2001. ISSN 01421123. doi: 10.1016/s0142-1123(01)00167-0. 3

A. Stroh. Constrictions and Jogs in Extended Dislocations. *Proceedings of the Physical Society. Section B*, 67(5):427–436, 1954. ISSN 0370-1301. doi: 10.1088/0370-1301/67/5/307. URL https://iopscience.iop.org/article/10.1088/0370-1301/67/5/307. 48, 50, 53, 63, 76

M. Sudmanns, M. Stricker, D. Weygand, T. Hochrainer, and K. Schulz. Dislocation multiplication by cross-slip and glissile reaction in a dislocation based continuum formulation of crystal plasticity. *Journal of the Mechanics and Physics of Solids*, 132:1–19, 2019. ISSN 00225096. doi: 10.1016/j.jmps.2019.103695. URL https://linkinghub.elsevier.com/retrieve/pii/S0022509619306428. 47

S. Suresh. *Fatigue of Materials*. Cambridge Solid State Science. Cambridge University Press, 1998. ISBN 9780521578479. URL https://books.google.fr/books?id=j4w6frFAiQcC. 7

M. Takagaki and T. Nakamura. Fatigue crack modeling and simulation based on continuum damage mechanics. *Journal of Pressure Vessel Technology, Transactions of the ASME*, 129(1):96–102, 2007. ISSN 00949930. doi: 10.1115/1.2388993. 14

Y. Tang. Uncovering the inertia of dislocation motion and negative mechanical response in crystals. *Scientific Reports*, 8(1):1–15, 2018. ISSN 20452322. doi: 10.1038/s41598-017-18254-5. URL http://dx.doi.org/10.1038/s41598-017-18254-5. 93

G. Taylor. The mechanism of plastic deformation of crystals. Part I.—Theoretical. *Proceedings of the Royal Society of London. Series A, Containing Papers of a Mathematical and Physical Character*, 145(855):362–387, 1934. 23

H. Tran and H. Homma. Experimental and Discrete Dislocation Dynamics Approach to Initiation of Cleavage Fracture under Short Pulse Loads. *Journal of Solid Mechanics and Materials Engineering*, 3(5):770–781, 2009. ISSN 1880-9871. doi: 10.1299/jmmp.3.770. 17

N. Tsutsumi, Y. Murakami, and V. Doquet. Effect of test frequency on fatigue strength of low carbon steel. *Fatigue & Fracture of Engineering Materials & Structures*, 32(6):473–483, 2009. 3

T. Vegge, T. Rasmussen, T. Leffers, O. B. Pedersen, and K. W. Jacobsen. Determination of the of Rate Cross Slip of Screw Dislocations. *Physical Review Letters*, 85 (18):3866–3869, 2000. ISSN 0031-9007. doi: 10.1103/PhysRevLett.85.3866. URL https://link.aps.org/doi/10.1103/PhysRevLett.85.3866. i, ii, xii, 19, 21, 71, 81, 83, 84, 86, 103

T. Vegge, T. Rasmussen, T. Leffers, O. Pedersen, and K. Jacobsen. Atomistic simulations of cross-slip of jogged screw dislocations in copper. *Philosophical Magazine Letters*, 81(3):137–144, 2001. ISSN 0950-0839. doi: 10.1080/09500830010019040. URL http://www.tandfonline.com/doi/abs/10.1080/09500830010019040. 49

M. Verdier, M. Fivel, and I. Groma. Mesoscopic scale simulation of dislocation dynamics in fcc metals: Principles and applications. *Modelling and Simulation in Materials Science and Engineering*, 6:755–770, 1998. ISSN 0965-0393. doi: 10.1088/0965-0393/6/6/007. URL https://iopscience.iop.org/article/10.1088/0965-0393/6/6/007. 17, 18, 47, 70

G. H. Vineyard. Frequency factors and isotope effects in solid state rate processes. *Journal of Physics and Chemistry of Solids*, 3(1-2):121–127, 1957. ISSN 00223697. doi: 10.1016/0022-3697(57)90059-8. URL https://linkinghub.elsevier.com/retrieve/pii/0022369757900598. 72, 73

J. Vogt, J. Bouquerel, and I. Proriol Serre. Cyclic Strain Localization Assessment by Advanced Microscopies. *Lecture Notes in Mechanical Engineering*, pages 25–35, 2020. ISSN 21954364. doi: 10.1007/978-981-13-8767-8_3. 9

V. Volterra. Annales scientifique de l'é.n.s. 24:401–517, 1907. 22

A. F. Voter. Classically exact overlayer dynamics: Diffusion of rhodium clusters on Rh(100). *Physical Review B*, 34(10):6819–6829, 1986. ISSN 01631829. doi: 10.1103/PhysRevB.34.6819. 105

D. Wagner, N. Ranc, C. Bathias, and P. Paris. Fatigue crack initiation detection by an infrared thermography method. *Fatigue and Fracture of Engineering Materials and Structures*, 33(1):12–21, 2010. ISSN 8756758X. doi: 10.1111/j.1460-2695.2009.01410.x. 5, 112

V. Wan, D. Maclachlan, and F. Dunne. A stored energy criterion for fatigue crack nucleation in polycrystals. *International Journal of Fatigue*, 68:90–102, 2014. ISSN 01421123. doi: 10.1016/j.ijfatigue.2014.06.001. URL http://dx.doi.org/10.1016/j.ijfatigue.2014.06.001. 87

X. Wang, V. Crupi, C. Jiang, E. Feng, E. Guglielmino, and C. Wang. Energy-based approach for fatigue life prediction of pure copper. *International Journal of Fatigue*, 104:243–250, 2017. ISSN 01421123. doi: 10.1016/j.ijfatigue.2017.07.025. URL http://dx.doi.org/10.1016/j.ijfatigue.2017.07.025. 87

J. Warren and D. Y. Wei. A microscopic stored energy approach to generalize fatigue life stress ratios. *International Journal of Fatigue*, 32(11):1853–1861, 2010. ISSN 01421123. doi: 10.1016/j.ijfatigue.2010.05.003. URL http://dx.doi.org/10.1016/j.ijfatigue.2010.05.003. 87

D. Weygand, L. Friedman, E. Giessen, and A. Needleman. Aspects of boundary-value problem solutions with three-dimensional dislocation dynamics. *Modelling and Simulation in Materials Science and Engineering*, 10(4):437–468, 2002. ISSN 09650393. doi: 10.1088/0965-0393/10/4/306. URL https://iopscience.iop.org/article/10.1088/0965-0393/10/4/306. 47, 70

L. Willertz. Ultrasonic fatigue. *International metals reviews*, 25(1):65–78, 1980. 3

A. Wöhler. Versuche zur Ermittlung der auf die Eisenbahnwagenachsen einwirkenden Kräfte und die Widerstandsfähigkeit der Wagen-Achsen. *Zeitschrift für Bauwesen*, 10(1860):583–614, 1860. 2

Y. Xiao, S. Li, and Z. Gao. A continuum damage mechanics model for high cycle fatigue. *International Journal of Fatigue*, 20(7):503–508, 1998. ISSN 01421123. doi: 10.1016/S0142-1123(98)00005-X. 14

S. Xu, L. Xiong, Y. Chen, and D. McDowell. Shear stress- and line length-dependent screw dislocation cross-slip in FCC Ni. *Acta Materialia*, 122:412–419, 2017. ISSN 13596454. doi: 10.1016/j.actamat.2016.10.005. URL https://linkinghub.elsevier.com/retrieve/pii/S1359645416307601. 49

B. Yang, P. Liaw, H. Wang, L. Jiang, J. Huang, R. C. Kuo, and J. Huang. Thermographic investigation of the fatigue behavior of reactor pressure vessel steels. *Materials Science and Engineering A*, 314(1-2):131–139, 2001. ISSN 09215093. doi: 10.1016/S0921-5093(00)01910-9. 87

Z. G. Yang, S. X. Li, J. M. Zhang, J. F. Zhang, G. Y. Li, Z. B. Li, W. J. Hui, and Y. Q. Weng. The fatigue behaviors of zero-inclusion and commercial 42CrMo

steels in the super-long fatigue life regime. *Acta Materialia*, 52(18):5235–5241, 2004. ISSN 13596454. doi: 10.1016/j.actamat.2004.06.031. 12

H. Zbib, M. Rhee, and J. Hirth. On plastic deformation and the dynamics of 3D dislocations. *International Journal of Mechanical Sciences*, 40(2-3):113–127, 1998. ISSN 00207403. doi: 10.1016/S0020-7403(97)00043-X. URL https://linkinghub.elsevier.com/retrieve/pii/S002074039700043X. 47, 70

G. Zhang and C. Yang. Monte Carlo study of the two-dimensional quadratic Ising ferromagnet with spins S=1/2 and S=1 and with crystal-field interactions. *Physical Review B*, 48(13):9452–9455, 1993. ISSN 01631829. doi: 10.1103/PhysRevB.48.9452. 104

R. Zhang, S. Naboulsi, T. Eason, and D. Qian. A high-performance multiscale space-time approach to high cycle fatigue simulation based on hybrid CPU/GPU computing. *Finite Elements in Analysis and Design*, 166(August):103320, 2019. ISSN 0168874X. doi: 10.1016/j.finel.2019.103320. URL https://doi.org/10.1016/j.finel.2019.103320. 15

T. Zhang, P. McHugh, and S. Leen. Finite element implementation of multiaxial continuum damage mechanics for plain and fretting fatigue. *International Journal of Fatigue*, 44:260–272, 2012. ISSN 01421123. doi: 10.1016/j.ijfatigue.2012.04.011. URL http://dx.doi.org/10.1016/j.ijfatigue.2012.04.011. 15

L. Zhigilei. Lecture slides: Partial dislocations in FCC crystals. In *MSE 6020: Defects and Microstructure in Materials*. 2018. ix, 33